UV-excited SnO$_2$ nanowire based electronic nose

Zur Erlangung des akademischen Grades eines

Doktor-Ingenieurs

von der KIT-Fakultät für
Elektrotechnik und Informationstechnik
des Karlsruher Instituts für Technologie (KIT)

genehmigte

Dissertation

von

MSc. Mustahsin Adib

aus Dhaka, Bangladesh

To my parents (Mr. and Mrs. Rahman)

Wife (Fariha Sultana)

&

Daughter (Raeefah Farnaz Adib)

Acknowledgment

Being an immigrant from a 3rd world country, the journey for Doctoral study at one of the finest universities in the world was not easy. It was only possible due to constant support from some wonderful people around me.

Gas sensing using surface chemistry requires profound material understanding and sound knowledge of measurement methodology. Therefore, the Doctoral study in the state-of-the-art gas sensing field coming with an electrical engineering background required a special kind of guidance. My mentor, Dr. Martin Sommer was the person who guided me on such a challenging journey. I have learned something new every time I talked with him. My special thanks to him for patiently guiding me, challenging me when needed, encouraging me when required, providing me valuable advice, suggestions, and feedback. I would also like to thank him for making my Doctoral journey the most special academic journey through different kinds of interactions. I am fully indebted to his supervision concerning all strategic, experimental, and theoretical aspects during my Ph.D.

Since the day I decided to look for an opportunity to study Optics and Photonics for my Masters in 2011, I know Prof. Lemmer. One of his articles on the KSOP webpage gave me the motivation to apply for KSOP. Later on, getting an opportunity to work with him closely during my doctoral study was a memorable experience. Two collaboration projects during that period with Innovation lab and LTI were possible because of his constant support and guidance. Especially, the Innovation lab project opened up new potential for printed gas sensors. Apart from the academic guidance, I was also supported immensely administrative-wise. I had a contract extension for 6 months in 2017, after my original 3-year contract. That was the most critical turning point of my life in Germany, as it helped me to finish my Ph.D. work and eventually let me stay in Germany legally with my family and find a job afterward at one of the finest companies in the world.

The parent group from where I got the opportunity to work on the project is 'Smart Materials and Devices'. The group is headed by Prof. Kohl. I would also like to thank him for his support at different times. I have worked with him very closely through weekly meetings, discussions, cleanroom work, lab work, preparation of presentation, poster, etc. All these interactions have created a dynamic scenario to learn a lot from him. I am grateful for those close interactions and valuable feedback.

Additionally, I had the opportunity to work and learn from different visiting scholars and among them, Prof. V. Sysoev is especially noteworthy. His perspective also helped me shape the research targets. Lastly, I am thankful to Martin Augustin who gave me a first-hand introduction to the different experimental set up after I joined.

I am thankful to Prof. Wilhelm Stork, as he taught me how to tackle a problem during research work. I remember in May 2013 I had a talk with him regarding the ideal approach to solving an engineering problem during my Master's thesis. He said roughly as follows:

'*Mustahsin, you should always understand the state-of-the-art technology at first. Then, you should look for the pain points of the existing solution. Then you should justify your methodology to break down the problem and define how your approach could offer better value than the existing solution. Always, take good preparation with the experimental setup, so that you can trust the result.*'

Since then, I am trying to follow his guidance as much as possible to date.

On a personal level, I am thankful to all the Bangladeshi communities living in Karlsruhe. Special thanks to Dr. Hossain for his guidance and extraordinary logistic support to ensure timely handover of the thesis to the department. Last but not least, special thanks to my current colleague at Infineon Technologies AG, Mr. Mauriz Trautmann for his help translating the abstract into German.

Preface

I have started my journey as an electrical engineer trained in one of the best engineering schools in Bangladesh called IUT before I came to Germany. After spending 2 years in the Bangladeshi academic environment during the post-graduation period, I have got the opportunity to pursue my MSc in Optics and Photonics at KIT in 2011. After joining KIT as a student, different sensing mechanism started to fascinate me as the sensors are an essential part of our life which translates our analog world into the digital world and enable us to make this planet a better place in many different ways.

Before starting my Ph.D. work, I had the opportunity to work with an optical sensor, pressure sensor, and temperature sensor at a different stage of my MSc, which motivated me to try something new with a considerable challenge. The possibility of developing an eNose, which can be scaled up to multiple applications while fulfilling several system requirements amazed me to the core. Thus, I tried to spend the best of my time in that brief Ph.D. period to tackle some of the key challenges in this area.

The work was carried out to fulfill the key application requirement as fire alarm using the eNose which has been envisioned within the scope of the Horizon 2020 SMOKESENESE project. As the call was led by one of the leading Fire equipment suppliers from Europe, FIRE EATER company, this gave us immense opportunity to test our solution in the real application environment. Simultaneously, several key limitations in the existing gas sensor solutions were addressed within the scope of this work.

Rosenheim, May 2021

Mustahsin Adib

Kurzfassung

Unsere Atemluft ist täglichen Schwankungen ausgesetzt und die Marktnachfrage nach Sensoren, die die Luftqualität messen können, steigt rapide an. Ein großer Teil dieser Nachfrage kann mit Metall-Oxid Gas Sensoren bedient werden. Diese Art von Gassensoren hat jedoch einige Nachteile im Bezug auf Genauigkeit, Langzeitstabilität, Leistungsaufnahme und Selektivität. Auch fehlen großvolumige Anwendungsbeispiele auf dem Markt, die Metall-Oxid (MOX) Gassensoren einsetzen und dabei alle Systemanforderungen erfüllen.

Diese Arbeit stellt die neueste Entwicklung der "KArlsruhe MIkro NAse", einer im Rahmen der EU Horizon 2020 Initiative namens SMOKESENSE entwickelten elektrischen Nase, vor und vergleicht diese mit dem aktuellen Stand der Technik für Metalloxid-Gassensoren.

Es wird gezeigt, dass durch UV-Anregung der SnO_2-Nanodrähte ein geringerer Stromverbrauch sowie eine minimierte Siloxan-Kontaminierung im Vergleich zu klassischen MOX-Sensoren erzielt wird. Zudem lässt sich mittels Aerosol-Jet-Druck eine vereinfachte und kostengünstigere Herstellung der Sensoren realisieren.

Um die Massenproduktionstauglichkeit für eine Anwendung als intelligenter Feuersensor sicherzustellen, wird der Wachstumsprozess der Nanodrähte optimiert. Außerdem wird ein neuartiges chemisches FET-ähnliches Sensorkonzept namens Chem-FET vorgestellt, das im Vergleich zu UV-KAMINA ein verbessertes Signal-Rausch-Verhältnis und eine schnellere Reaktionszeit bietet. Eine überwachte Lernmethode des Maschinellen Lernens basierend auf einer linearen Diskriminanzfunktion wird verwendet, um verschiedene Zielgerüche zu klassifizieren. In einer Anwendung als Feuersensor erwiesen sich die entwickelten Sensorprototypen als konkurrenzfähig. Zusätzlich werden Möglichkeiten aufgezeigt, das Sensorprinzip als Plattform für andere Anwendungsarten verwenden zu können.

Während mit den vorgestellten Methoden die Leistung des Gesamtsystems optimiert werden konne, bleibt als Ausblick Verbesserungsbedarf in Bereichen, wie z. B. der Charakterisierung von Gerüchen und der Testmethodik für die Anwendung in hohen Stückzahlen.

Abstract

The air we breathe is changing every day and the market demand for the sensors that quantify our surrounding air is growing rapidly. A big portion of that market appetite can be fulfilled by a Metal oxide gas sensor. However, these types of gas sensors are lacking accuracy, long-term stability, low power consumption, and decent selectivity. The market is also lacking high-volume application examples using such sensors while fulfilling the system requirements.

In this work, we tried to challenge the state-of-the-art metal oxide gas sensor solution with an electronic nose. The work represents the latest development of '**Ka**rlsruhe **MI**kro **NA**se' within the scope of the European Union Horizon 2020 initiative project called, SMOKESENSE. The use of UV illumination as a means to excite the SnO_2 nanowire improves the power consumption and minimizes Siloxane contamination. Additionally, due to the implementation of aerosol jet printing technology, the sensor concept became simpler and more cost-efficient. The nanowire growth process has been optimized to ensure mass production capabilities for the final application as a smart fire alarm. Last but not least, a novel chemical FET-like sensor concept has been presented called Chem-FET, which offers a better signal-to-noise ratio and faster response time compared to UV KAMINA. Linear Discriminant Analysis (LDA) has been used as a supervised machine learning method to classify the fingerprint of targeted smells. The prototype version of the developed sensor demonstrated competitive performance as the fire alarm. Additionally, the sensing principle can easily be used as a platform for other types of applications.

Even though the presented sensing methodology optimized the complete system performance; however, several areas need to be improved as an outlook including smell characterization, and testing methodology for high volume applications.

Table of contents

List of figures

List of tables

List of abbreviations

CAGR	Compound Annual Growth Rate
eNose	Electronic Nose
HTC	High-Temperature Condensation
IMT	Institut für Mikrostrukturtechnik
LDA	Linear Discriminant Analysis
NAAQS	National Ambient Air Quality Standards
SME	Small Medium Enterprise
VLS	Vapor-Liquid Solid
XRD	X-Ray Diffraction
US EPA	United States Environmental Protection Agency
WHO	World Health Organization
NAAQS	National Ambient Air Quality Standards
PM	Particle Matter
HVAC	Heating Ventilation and Air Conditioning
MFC	Mass Flow Controller

1   Introduction

The amount of air flowing in and out of our lungs with each breath is termed tidal volume and a fully-grown person inhales and exhales roughly 500 ml during quiet breathing[1]. On average an adult breathes 15,000 liters of air every day. Since the 17th century, the air we know and breathe is changing every second because of the industrial revolution. The industrial revolution has been the driving force of air pollution for centuries, as it started to change the way that we created everything before; from nutrition and energy to health and industrialized technologies. Part of the reason was the overachieving industrial growth target along with our inability of foreseeing the environmental impact of burning coal and fossil fuels. As shown in figure 1, according to the United States Environmental Protection Agency's (US EPA) air pollutant emissions trends data, between 1995 and 2019, emissions due to gross domestic product increased from 60% to 182%. At the same time, emissions due to vehicle miles traveled increased from 60% to 114%.
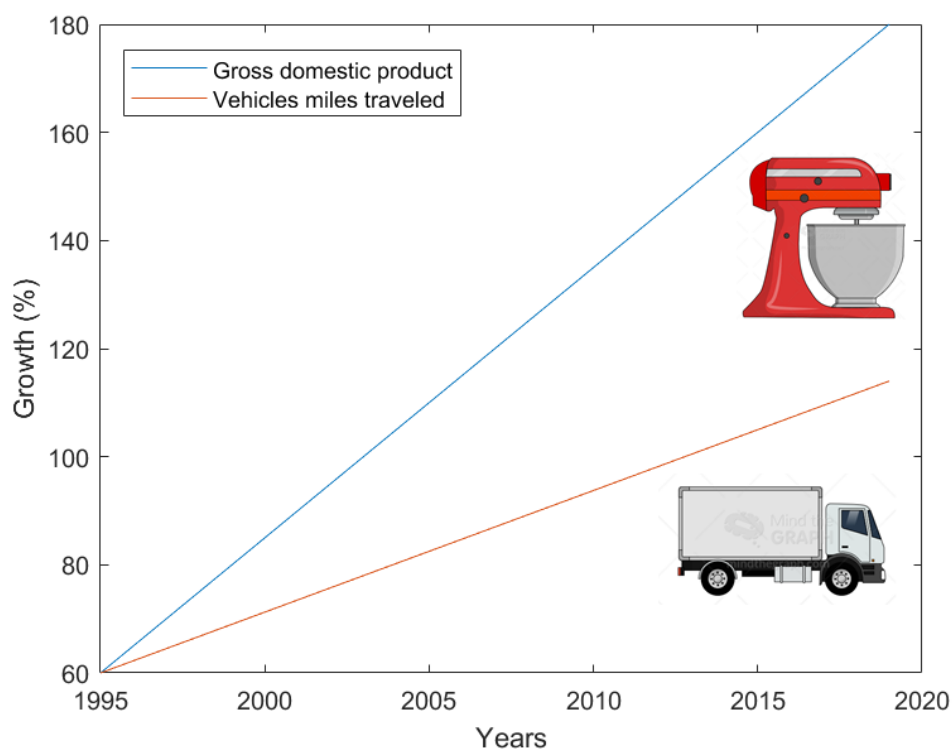
Figure 1: Comparison of growth areas and emissions from 1995 to 2019. Within that period emissions due to gross domestic product increased by 122%. At the same time, emissions due to vehicle miles traveled increased by 54%. The graph has been recreated and modified from the reference[2].

Figure 1 has been drawn in Mind the graph workspace under a common license agreement.

According to EPA, as of 2019 approximately 82 million people nationwide lived in countries with high pollution levels as shown in figure 2[2].
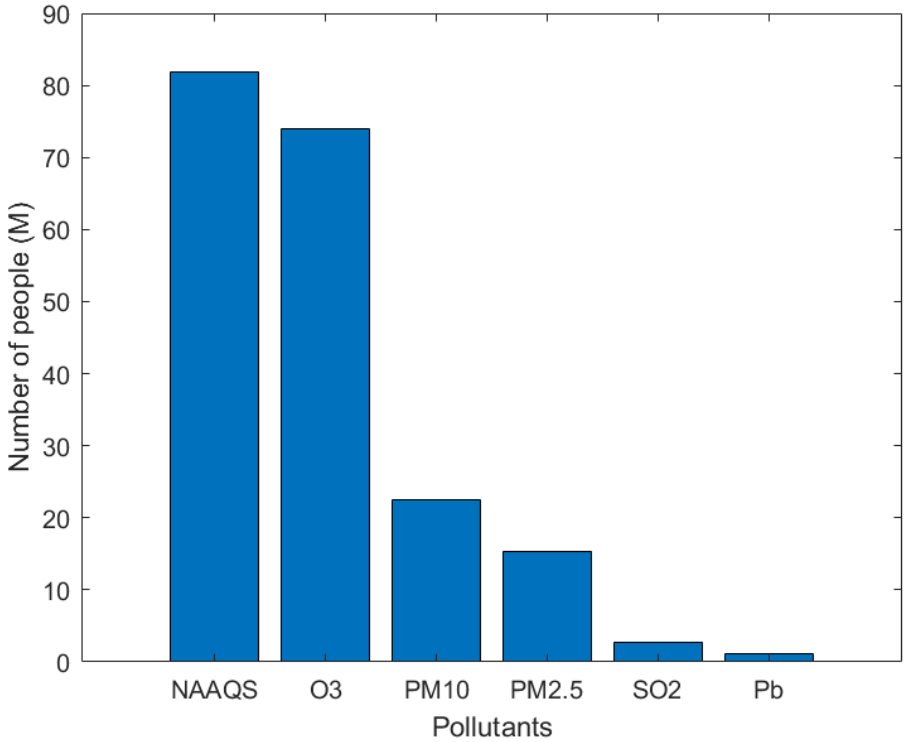
Figure 2: Number of people living in countries with air quality concentration above the tolerable level of NAAQS (At least one of the substances from the listed pollutants), O_3, PM10, PM2.5, SO_2, and Pb in 2019. Recreated from the reference[2].

All of these air pollutants are harmful to our health in many different ways. This also has adverse impacts on the environmental ecosystem. World Health Organization (WHO) reported 7 million deaths per year linked to air pollution[3], which is reflected as 5 trillion USD yearly economic damage[4]. Employee productivity can be decreased by up to 50% due to poor air quality in the offices[5]. All these development justifies air pollution featuring in UN Sustainable Development Goals (SDGs)[6].

Therefore, logically gas sensor's importance is growing in the market, as it has the potential to revolutionize the way we interact with air quality at the moment. According to the Yole development report, the gas sensor market will soar up to ~ $1B in 2023 with a 6% Compound Annual Growth Rate (CAGR)[7]. The market growth will be driven by demand control ventilation with energy-saving and maintaining of good air quality as two primary objectives. Additionally, in the consumer section, they also predict that the gas sensor

might be the next sensor to be integrated into smartphones in near future. However, the biggest market share belongs to safety applications.
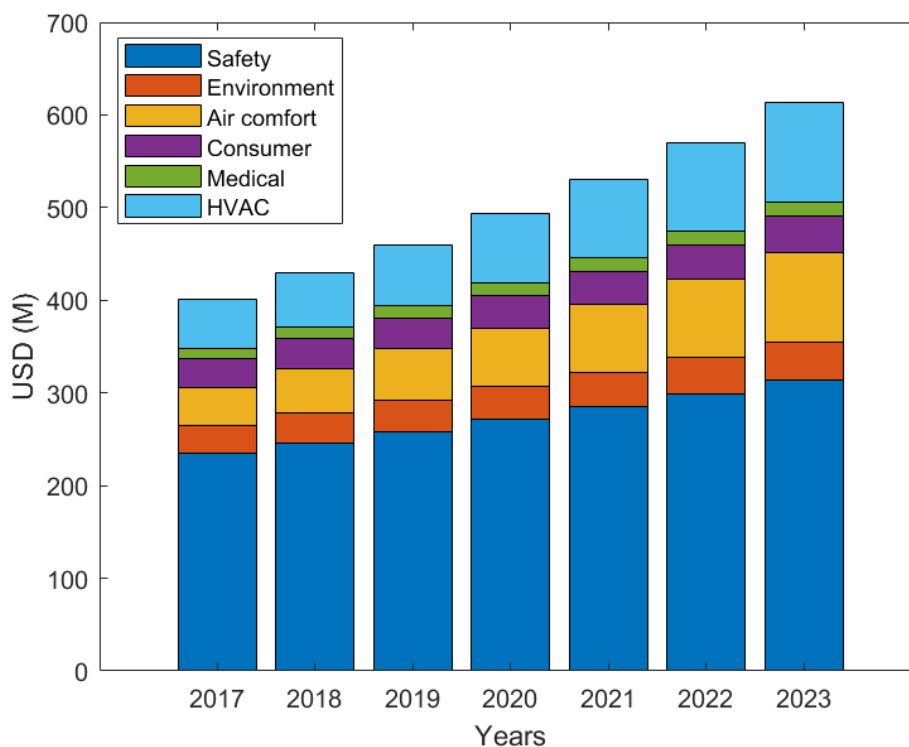
Figure 3: Gas sensor market projection from 2017 to 2023. The market is dominated by safety applications. However, the main growth driver is HVAC (Heating Ventilation and Air Conditioning) and Air comfort/ well-being products. At the same period, medical and consumer applications will experience steady growth. Recreated from the reference[7].

The rapid growth of the market indicated strong potential which is visible in the patent battles among the leading companies. Leading companies are trying to cover as many technologies as possible with a goal to enter the smartphone market. Sensor size, stability, selectivity, and energy consumption are the limiting factors to enter into the consumer domain. Therefore, a large number of publications and patents in the gas sensing segment are targeting specific gas selectivity with the help of material optimization or introducing physical detection techniques.

However, apart from specific gases, there are applications where fingerprints of a combination of gases need to be detected i.e: breath analysis to indicate health risk[8,9], food

freshness monitoring[10], early fire detection[11], explosive detection[12], etc are notable applications. For such applications, an electronic nose system is better suited than a typical gas sensor targeting a specific gas. Within the scope of this work, an electronic nose platform has been developed and relevant applications have been investigated thoroughly.

To develop an electronic nose, both the material development process and algorithm need to be optimized for a targeted application. The work has been carried out under the umbrella of the SMOKESENSE project of the European Union Horizon 2020 initiative. SMOKESENSE project envisioned to radicalize the fire detection technology by developing a novel system consists of a miniaturized smart smell sensor having superior performance compared to the state-of-the-art fire alarms. The sensor solution is targeted to disrupt safety and consumer applications. Several key areas have been identified as pain points for the existing fire hazard safety solutions in the market, which are listed below:

- The limited scope of measurements and amount of gasses
- Complex system requirement with multiple sensor components
- Poor early detection capabilities, as the sensor is placed far from the fire source

These limitations result in extensive economic and ultimately even personal losses either due to late response or false alarms. The consortium members were committed to overcoming scientific and technical barriers by developing a system with the ideal combination of gas sensing technologies and machine learning algorithms.

Naturally, the project objective defined the first *research target*.

Research Target 1: *Develop a SnO_2 nanowire-based eNose that can be used as a smart fire detector. The eNose should be able to detect potential fire hazards in the early stage and simultaneously predict the source of the potential fire.*

A very important aspect of any technology development is scalability. Scalability defines the system's ability to be used across multiple applications according to market potential. The project stakeholders would become more confident to invest in a technology development cycle that is easily scalable. Hardware and software both need to have the ability to fulfill the need for multiple applications. This scalability requirement defines the second *research target* of this work.

Research Target 2: *The developed platform within the scope of the SMOKESENSE project should be able to reuse for other applications.*

State of the art metal oxide gas sensor comes with several limitations[13], explicitly:

- High energy consumption due to constant heater control operation at 300 °C
- Complex system requirement to maintain a fixed target temperature on the heater element

- Poor long-term stability due to multiple drifting components
- Strong cross sensitivities to non-targeted gases
- Gradual sensitivity loss of the sensor due to Siloxane contamination

The task to optimize these limitations has defined the third research target.

Research Target 3: *Investigate the root cause of the limitations of the state-of-the-art SnO$_2$ material for gas sensing application and demonstrate a potential solution to minimize as many limitations as possible within the scope of the thesis work.*

All three research targets are addressed in section 6.4 of Chapter 6.

Thesis outline:

The introductory chapter is followed by chapter 2, *Theoretical Framework* which provides the necessary theoretical foundation to follow the rest of the content of this thesis.

Chapter 3, covers all the experimental setups and test methodology which have been used at different stages of the work. Additionally, the SnO$_2$ growth process has also been discussed in detail.

Chapter 4 titled *KAMINA (KArlsruhe MIkro NAse)* covers the journey of the KAMINA system from heater-based KAMINA to UV-KAMINA which has been used successfully to facilitate the SMOKESENSE project.

Chapter 5 titled *UV Chem-FET KAMINA* introduces a novel electronic nose concept, which has minimized some of the shortcomings of the UV KAMINA. From concept to final demonstration as an eNose-prototype has been covered in detail in this chapter.

Chapter 6 is titled *Performance of the sensor as eNose*, where all the major results have been summarized and presented. The final status of the research targets is also addressed here.

Last but not the least, chapter 7 titled *Executive Summary* captures the key achievements of the thesis and offers an outlook to the future.

2 Theoretical Framework

This chapter is designed to facilitate the reader to become familiar with the electronic nose concept. eNose is developed based on two main components, namely a gas sensor array and a machine learning algorithm. The fundamentals of the classification algorithm, called Linear Discriminant Analysis (LDA) will be discussed, which has been used extensively throughout this work to quantify the eNose performance. Additionally, a brief introduction to SnO_2 nanowire material is provided, which has been used in an array as a sensing element for this work.

2.1   Electronic nose

Electronic nose or eNose is an electronic sensing system designed to detect odors or smells. An eNose needs to mimic a mammalian olfaction system to perceive the smell as a global fingerprint. The steps of the recognition process are very similar to the human olfaction system. For humans, when a smell is experienced, the nose and the mind cooperate to sort out many exceptionally minuscule atoms or compounds, that are skimming around. If a greater amount of these atoms arrives at the top of the nasal cavity while sniffing, it is easier to smell. Inside the nose, some neurons covey the electrical messages to the brain, where it processes the information and trains itself with the particular smell for future detection.

For example, as shown in figure 4, when something is burning in the living room, a lot of complex organic and inorganic material starts burning simultaneously. Residues in the air go through our nasal cavity and in the 2nd step, olfactory mucosa sends a specific burning fingerprint signal to the brain. The brain classifies the smell signal based on previous learning and takes emergency preventive action. Then the brain updates the classification of the burning smell data for future reference.

Recent studies done by A. Keller and the team reported that humans can discriminate more than 1 trillion smells[14] using 400 types of receptors, which are a total of several million in number. Specific receptors in the nose trigger signature neural responses. However, many details of the complete sequence are still unknown.
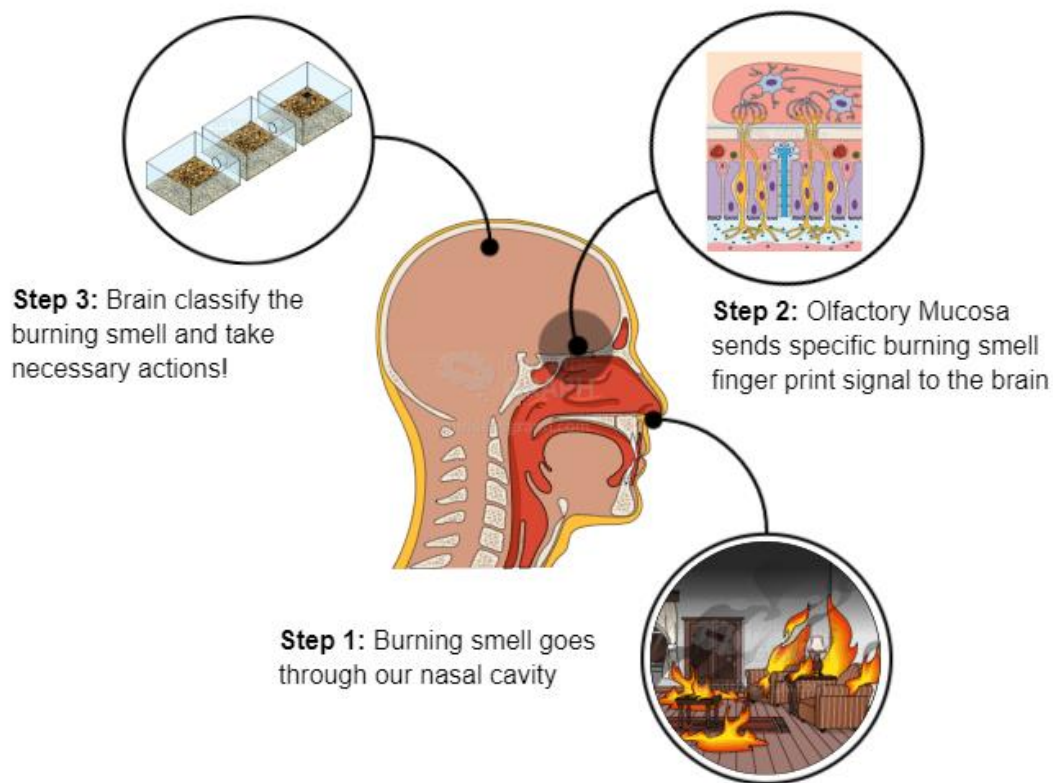
Figure 4: The way the human nose identifies, classify and remembers the fingerprint of a burning smell. Step 1: Burning smell goes through the nasal cavity of a human being. Step2: Olfactory mucosa sends an already trained signal to the brain. Step3: The brain classifies the signal and recognizes that something is burning and take necessary actions.

Similarly, eNose has two main building blocks explicitly gas sensors as smell receptors and a computational unit where the receptor signal is processed and classified based on previously characterized training data. The smell classification is done in the learning phase. The idea has been presented numerous times with different technologies[15–23]. However, the essence of each approach is identical, which is a combination of an array of sensing elements and a machine learning algorithm.

As shown in figure 5 to use an eNose as a fire alarm the burning smell initially needs to be detected by the sensor array followed by smell classification based on a machine learning algorithm.

Figure 4 has been drawn in Mind the graph workspace under a common license agreement.

8

Step 1   **Step 2**   **Step 3**

Burning smell   Smell sensing element   Smell classification using machine learning algorithm
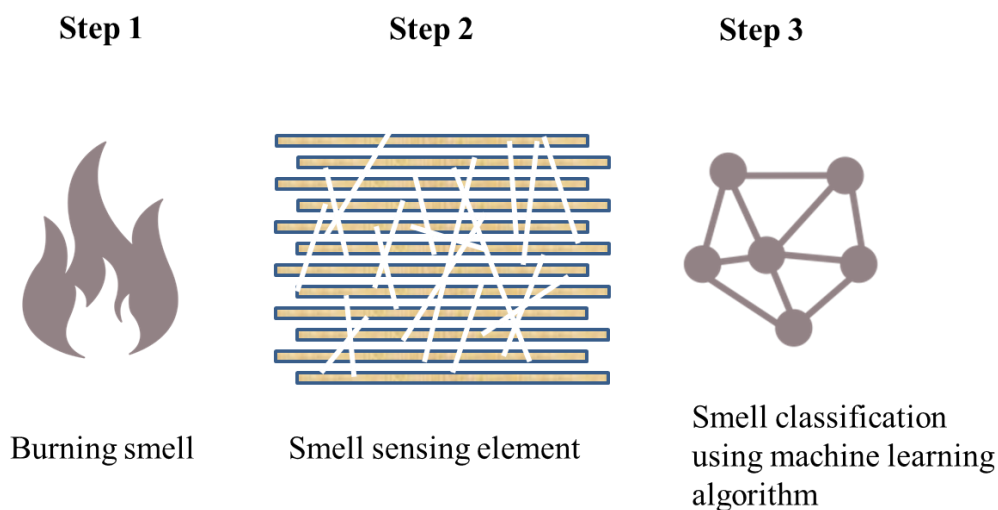
Figure 5: Resemblance of eNose with a biological nose. Step1: The burning smell is generated and traveled to the sensing element. Step2: The sensing element of the sensor reacts with the molecules responsible for the burning smell and sends an already taught fingerprint signal to the application layer. Step3: At the application level, the burning smell fingerprint signal is classified using a machine learning algorithm

For this study, SnO_2 nanowire material has been used as the detector and Linear Discriminant Analysis (LDA) as the classification algorithm. LDA is a commonly used technique for data dimensionality reduction and classification.

2.2 Classification algorithm: Linear Discriminant Analysis (LDA)

Linear Discriminant Analysis is a dimensionality reduction method. It discriminates the groups based on several features. It tries to reduce the number of dimensions in a dataset while retaining as much information as possible. The original technique was developed as Fisher's Discriminant Analysis[24], which was a two-class technique. LDA is one of the widely used classification techniques at the moment[25–30]. LDA is a purely statistical method (multivariate data analysis method) without any averaging, fitting, or other processes which cut or estimate data. All input data is kept alive and LDA gives just the best view on the data concerning the separation of groups.

The following steps need to be followed to use the LDA technique for classification.

    I.   LDA can only be used as supervised classification techniques. Therefore, the data must be labeled by a subject matter expert.

II. Separability, S_b between different classes needs to be calculated using the following equation:

$$S_b = \sum_{i=1}^{g} N_i (\overline{X_\iota} - \overline{X})(\overline{X_\iota} - \overline{X})^T$$

Where,

S_b = Separability
g = Number of classes
$\overline{X}$ = Mean of the class means
T = Transpose

III. Within the class, variance needs to be calculated by calculating the distance between the mean and data point from each class. Within-Class Variance, S_W can be calculated using the following equation:

$$S_W = \sum_{i=1}^{g} \sum_{j=1}^{N_i} (X_{i,j} - \overline{X_i})(X_{i,j} - \overline{X_i})^T$$

IV. Find a lower-dimensional space that maximizes between-class variance (Step II) and minimizes within-class variance (Step III) using the following equation:

$$P_{LDA} = arg\ max \frac{|P^T S_b P|}{|P^T S_w P|}$$

Where,

P = lower-dimensional space projection. Also known as Fisher's criterion.

The principle is presented in figure 5. The LDA algorithm looks for a projection that minimizes the distance S_w and at the same time maximizes the distance S_b between each class.
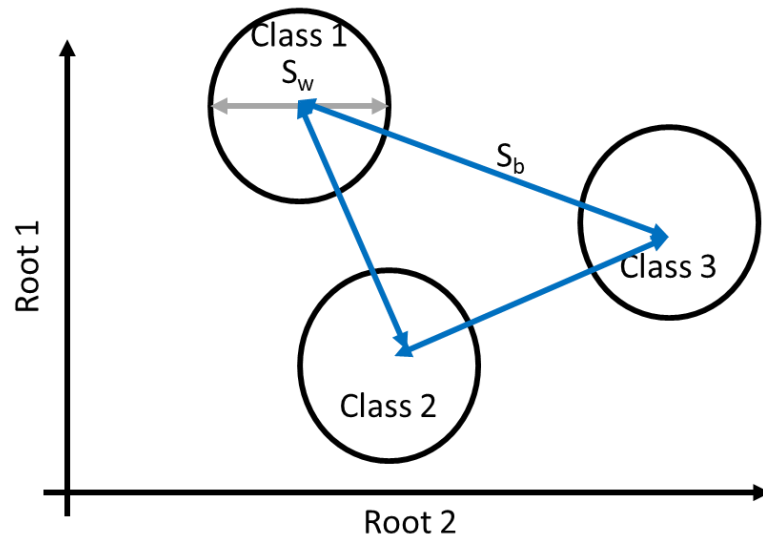
Figure 6: The working principle of the LDA algorithm looks for a projection that minimizes the distance S_b and at the same time maximizes the distance S_w between each class.

2.3 SnO$_2$ nanowire

SnO$_2$ is an n-type semiconductor with a wide bandgap (E.g. = 3.6 eV at 300 K). It has been widely used for gas sensing, optoelectronic devices, transparent conductor, and many other applications. Only because of its vast practical importance, an increasing amount of work has been done on crystalized SnO$_2$ to understand the semiconducting nature of this material. In this section, the geometry, band structure, optical properties, and gas sensing properties of SnO$_2$ nanowire (section 2.3.5) will be discussed.

2.3.1 The geometry of SnO$_2$ nanowire

SnO$_2$ nanowire has a tetragonal rutile structure with a space group of **P4$_2$/mnm** (136), where, **P** indicates a primitive Bravais lattice, **4$_2$** a screw axis, **m** indicates mirror planes and **n** indicates a glide plane. The unit cell contains two Tin and four Oxygen atoms as shown in figure 7.
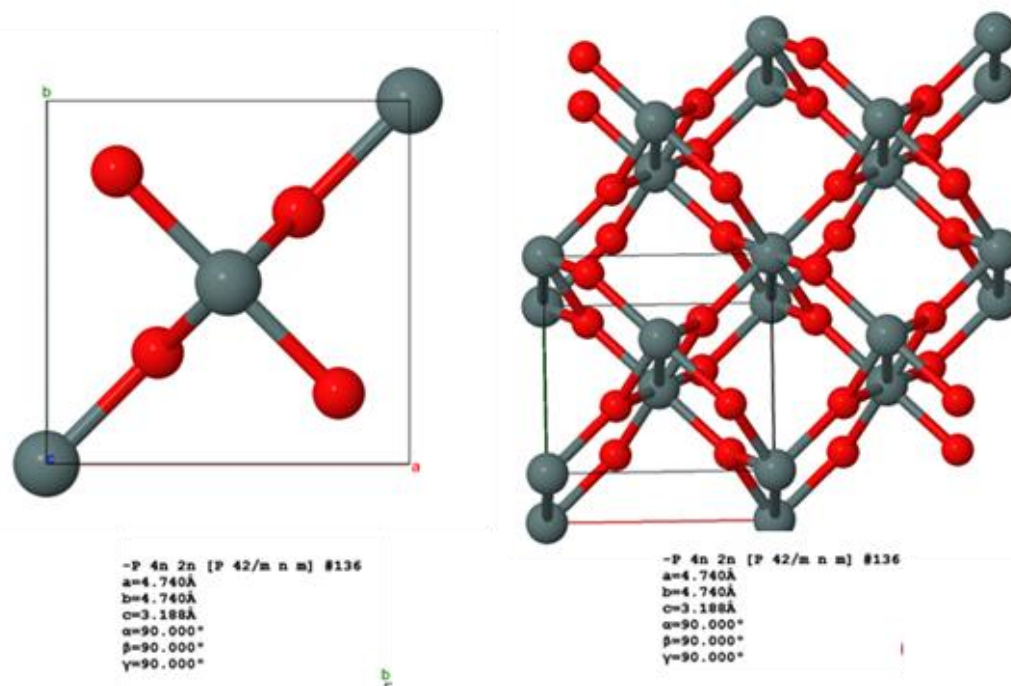
Figure 7: Typical SnO₂ nanowire unit cell and crystal structure. The figure has been produced using VESTA software under a common license agreement[31].

Six oxygen atoms are placed approximately at the corners of an octahedron and each oxygen atom is surrounded by three tin atoms approximately at the equilateral triangle corners, which gives the structure 6:3 co-ordinations. The typical lattice parameters measured using XRD, are a=b= 4.7 Å; c= 3.18 Å with the c∕a ratio of 0.676. Ionic radii for O2- is 1.4 and for Sn4+ 0.7 Å.

2.3.2 Band structure of SnO₂

The band structure of SnO₂ is nicely captured in different publications [32–34]. As shown in figure 8, the conduction band minimum is at the zone center Γ. This state from 3.6 eV upwards is a single minimum having no subsidiary minima leading to an indirect gap. The main minimum is formed due to the $5s^2$ state. Sn has an electronic configuration as follows $[Kr]4d^{10}5s^25p^2$. It is a direct bandgap with an effective mass of 0.23-0.3. In a tight binding portrayal, it contains 96% of Sn S states.

The upper valence band from 0 eV to -8.1 eV consists of mainly 2p states of Oxygen along with some Sn s and p states. The Ionicity of SnO₂ is approximately 60%. Additionally, at -16 eV, there are O 2s states which are not contributing to the bonding.

The upper valance band is fairly flat contributed by oxides having a large effective mass, which does not favor conduction by holes. The valance band maximum has Γ_2^- symmetry

providing indirect bandgap[35], which is also consistent with the UV spectra, which has been presented experimentally[36].
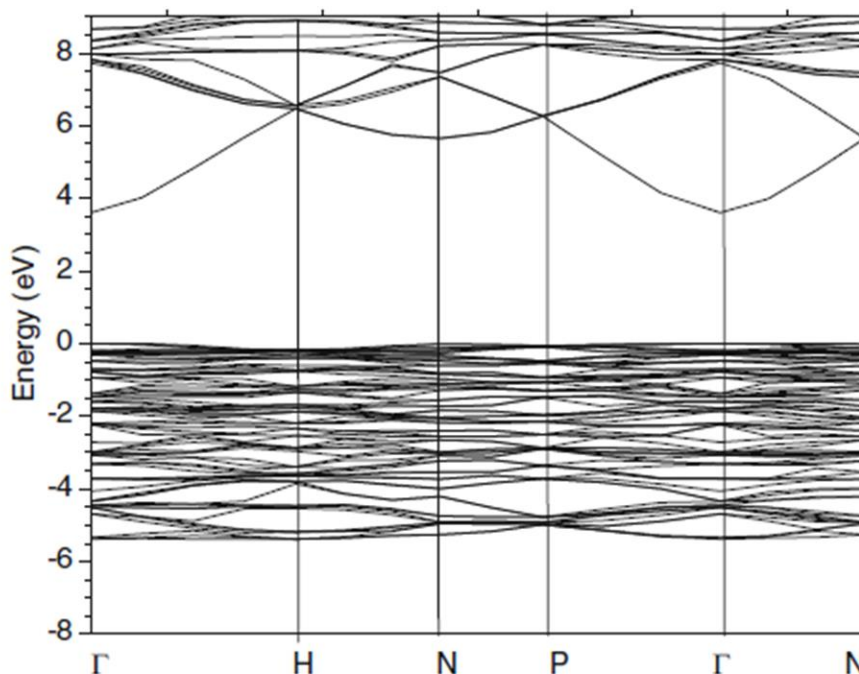
Figure 8: SnO₂ band structure. Bandgap fitted[33]. Reused with permission from Springer Nature'

2.3.3 Optical properties of SnO₂ nanowire

The optical properties of SnO₂ nanoparticles and thin film have been investigated extensively by several groups[37–40]. However, comparatively, there is less reporting on the optical property of SnO₂ nanowires, which has been nicely covered by I. Manna et al. [41] and later confirmed by M. Augustin and M. Sommer et al[42]. In the group of I. Manna, the SnO₂ nanowires were synthesized based on thermal evaporation of Sn powders in the presence of a gold catalyst. UV-VIS absorption spectra of the samples were studied for the wavelength range 200–800 nm to determine the bandgap using a PEL 45 spectrophotometer. The optical bandgap is reported to be 3.6 eV which is similar to the reported bulk SnO₂ bandgap[39]. The typical absorption spectrum is presented in figure 9. Within SnO₂ nanowires, there is oxygen deficiency in the surface which is situated at ~2.7 eV below the conduction band minima and 0.9 eV above the valance band maxima. The oxygen vacancies also possess a high electron affinity to trap electrons locally forming intermediate states near conduction band minima[43].
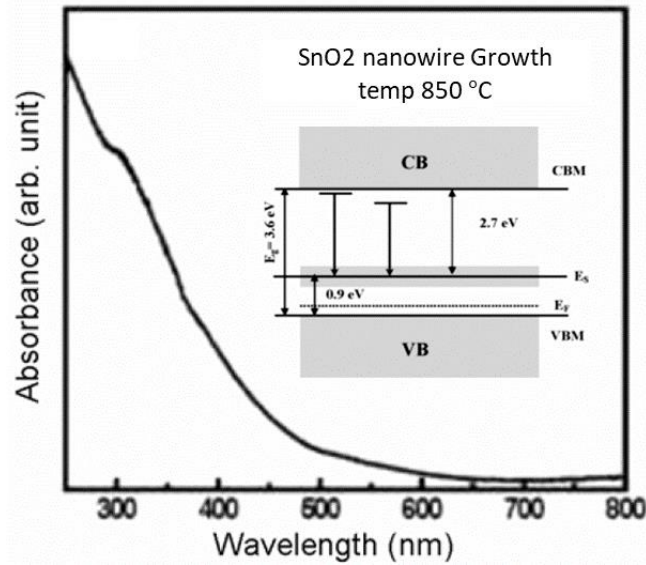
Figure 9: Typical optical absorption spectrum of SnO₂ nanowires grown at 850°C temperature. <u>Inset</u>: Schematic energy band diagram of SnO₂ nanowires and nanobelts, where the optical bandgap is reported to be 3.6 eV. Recreated from[41] with permission.

2.3.4 Electrical properties of SnO₂ nanowire with UV illumination

The electrical properties of SnO₂ material are initially published by Jarzebski and Marton et al[44]. In pure form, SnO₂ is an n-type wide-bandgap semiconductor, and therefore its electrical conduction results from the existence of point defects (native and foreign atoms) which act as donors or acceptors. Later on, electrical characteristics of SnO₂ nanowire under UV illumination have been reported by Wei Lu et al[45]. In essence, when a pristine SnO₂ nanowire makes a connection between two electrodes, a rectifying behavior is expected at room temperature without any excitation, as shown in figure 10(a) (curve a). This is the signature behavior of Schottky barriers at the metal/ semiconductor contact. In a vacuum (10^{-5} Torr), a smaller increase in current can be observed (curve b). Upon illumination by UV light, Ohmic behavior can be expected (curve C) by enhanced electron tunneling at the Schottky junction due to an increment of carrier density attributed to oxygen desorption and reduction of the depletion zone with the above bandgap photons.
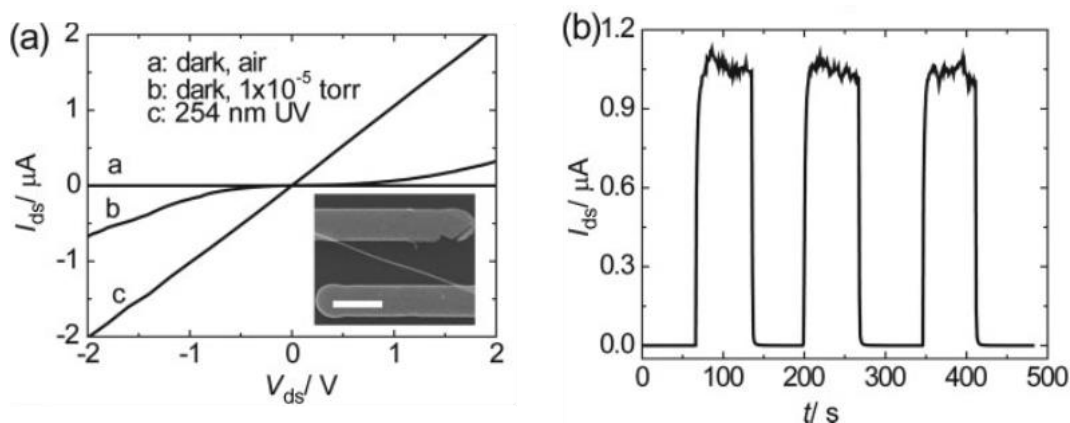
Figure 10: Electrical properties of a SnO₂ nanowire. (a) I_{ds}-V_{ds} curves of a nanowire device measured in the dark at atmospheric pressure (curve a) and in a vacuum (curve b) and exposed to 254-nm UV at atmospheric pressure (curve c). <u>Inset:</u> scanning electron microscopy (SEM) image of the SnO₂ nanowire device. (b) Reversible switching of the nanowire device between low and high-resistivity states as the UV light was turned on and off frequently. Reused with permission from[45].

As shown in figure 10(b), for a device having a single nanowire conduction path, when the UV source switched on and off and rapidly, the resulting current increased from 0 to 1μA. For a short period, the recovery time can be very fast (~ 1 s). The photocurrent sensitivity was estimated to be ~5×10^5. The photoconductive gain can be defined as the ratio of the number of electrons collected per unit time and the number of photons absorbed per unit time. The gain reported was 3000, which is comparable to earlier studies on similar material[46–50]. This effect is due to the long photocarrier lifetime along with short carrier transient time in nanowire devices. Such property ensures a fast response time and high photocurrent sensitivity. Consequently, SnO₂ nanowire Schottky diodes are suitable candidates as UV photodetectors or photo-switches.

2.3.5 Gas sensing properties of SnO₂ material

The gas sensing property of a metal oxide material is well-known since the last century[51–53]. However, the fundamentals of gas sensing property have been nicely explained for the first time with a theoretical model by Barsan and Weimar et al[54,55].

In simple terms, an n-type metal oxide-based gas sensor like SnO₂, in normal air at excited condition (heat or UV excitation) accumulates oxygen at the surface by trapping electrons from the bulk, and consequently the resistance of the sensor increases. A target gas in the atmosphere may interact with the pre-adsorbed Oxygen or directly with the Oxide and trigger a change of the sensor resistance, which can be monitored as the sensor signal. Within the detection range, the sensor signal can be correlated to the concentration of the

target gas. Therefore, two aspects need to be considered, i.e. 1) The surface reaction between the material and the gases and 2) the transduction into the resistance changes of the sensor. This phenomenon has been nicely captured in figure 11.
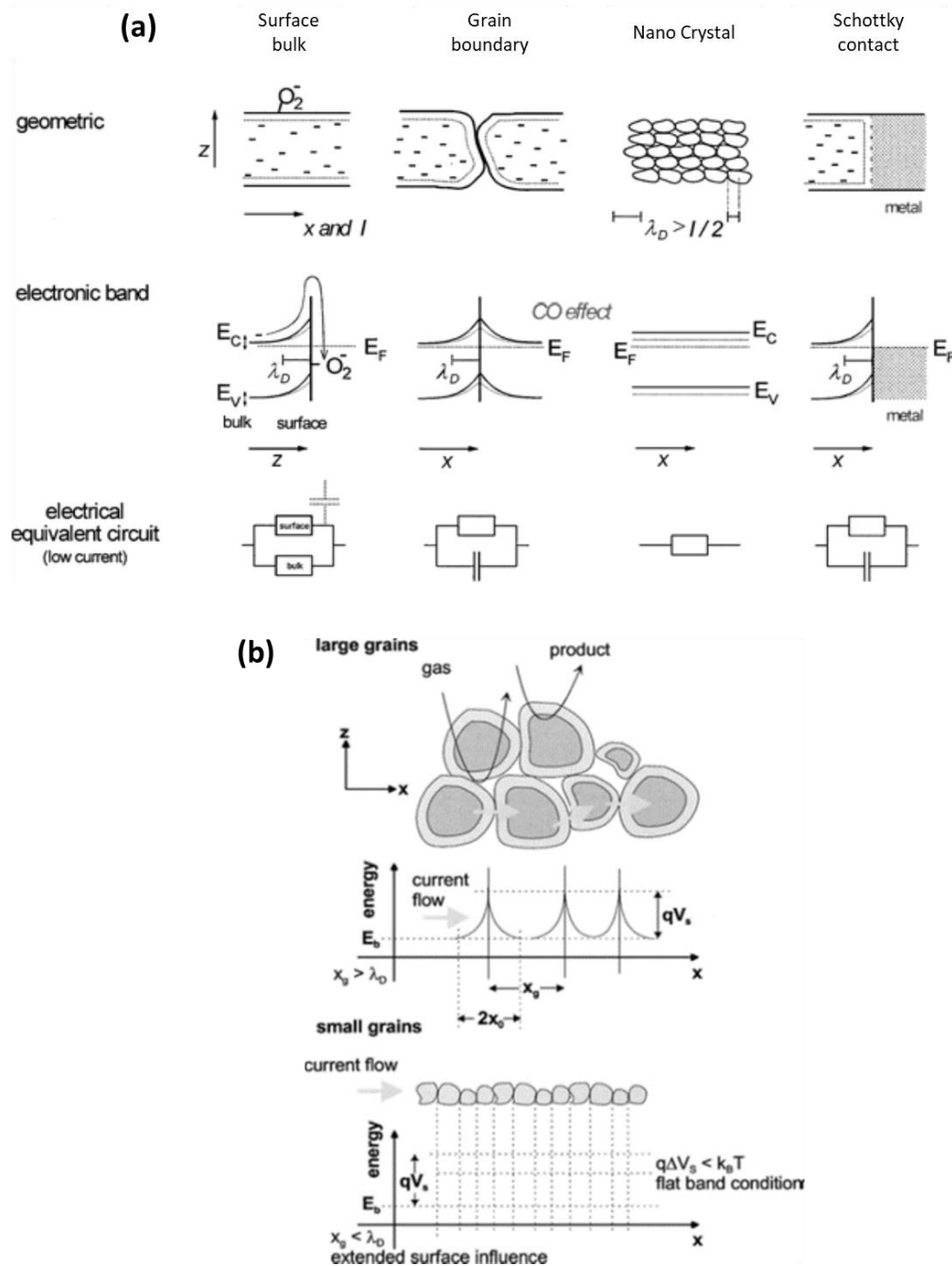
Figure 11: (a) Schematic representation of a porous sensing layer with geometry and energy band. λ_D Debye length, x_g grain size. (b) Different conduction mechanisms and changes upon O2 and CO exposure to a sensing layer in overview: This survey shows geometries, electronic band pictures, and equivalent circuits. E_C minimum of the conduction band, E_V maximum of the valence band, E_F Fermi level, and λ_D Debye length. Reused with permission from[55].

The performance of the sensor depends on the measurement parameters like excitation power, the morphology of the nanowire, and Schottky potential. A nanowire is a single crystal, the surface reaction that influences the complete conduction path. For a nanowire-based gas sensor, the gas interaction can happen at the surface of a nanowire or the interface between the nanowire and electrode. Under excitation, the nanowire gas interaction is analogous to a change of initial resistance, R, however, at the metal nanowire junction, the gas response is analogous to a parallel RC circuit as shown in figure 11 (b) as nano-crystal and Schottky contact.

In the case of chemisorption, the position of the Fermi level changes relative to the positions of the conduction band and valance band. In contrast, in the case of ion-absorption, the transfer of charge takes place between adsorbate and adsorbent, hence, the Fermi level is raised resulting in a net transfer of electrons to the surface via downwards bending of the bands, while hole-electron pairs are generated within the solid by the absorption of photons. If photon flux is interrupted, the system relaxes towards the equilibrium position. A reversible change can be expected with adsorption under irradiation and desorption in the dark.

However, one of the limitations of SnO_2 material's gas sensing property is its selectivity towards a target gas, which is a major limiting factor for some of the applications. For example, SnO_2 material is widely used as an indoor air quality sensor, where it monitors the Volatile Organic Compound concentration. Common examples of VOCs that are present in the indoor environment are Benzene, Formaldehyde, Xylene, Toluene, etc. Common sources of VOCs are paints, wood preservatives, aerosol sprays, cleansers, disinfectants, dry cleaned clothing, building materials, furnishing, office equipment such as copiers, printers, etc[56]. Regrettably, different types of VOC react very similarly with SnO_2. Not all VOCs are proven to be harmful to health[57–59]. Formaldehyde and Benzene have a more adverse effect on our health than other VOCs[60,61]. Therefore, actual indoor air quality should have been monitored based on Formaldehyde and Benzene concentration, but as most of the VOCs are having a similar surface reaction with SnO_2, such device can't be selective towards a specific type of VOC. For this work, the selectivity is achieved by using an additional classification algorithm, which minimizes such material limitation for a targeted application.

2.4 SnO_2 nanowire synthesis methodology

Due to high application potential, the controlled growth of nanowires is decisive to build devices having specific physical properties. Being an eminent METAL OXIDE gas sensor with a wide bandgap, the SnO_2 nanowire/ nanobelts synthesis process has been reported on multiple occasions. For the preparation of metal oxide nanowires, a template-

based approach has been reported on multiple occasions[62,63]. The template-based approach gives better control over the size and morphology; however, there are several shortcomings with this approach. Metal nanowires synthesized often possess poly-crystallinity and removal of the template is troublesome as it prevents straight and smooth channels. Therefore, Vapor-Liquid-Solid (VLS) and Vapor-Solid (VS) mechanisms are popular for such metal-oxide nanowire synthesis due to favorable fast growth. Freestanding Si whiskers with sub-micro radii on a Si substrate having Au island at 1000 °C was first reported by Wagner et al in 1964[64] and later on by Givargizov et al in 1987 [65]. The mechanism is presented in figure 12. However, the physical properties of nanowires are mainly determined by their synthesis process. Recent reviews have captured the fundamental and technological achievements in the synthesis process of 1D nanostructures[66–71].
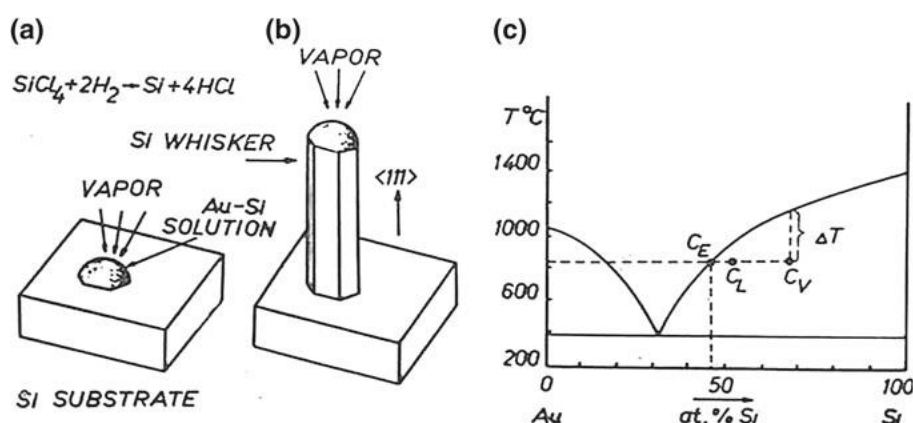
Figure 12: The Wagner-Ellis sketch schematizing the VLS growth of Si "whiskers" by the Au-assisted CVD. (a) Au-Si droplet on the substrate surface; (b) Whisker growth under the droplet; (c) Au-Si phase diagram showing the melting point at 363°C and the equilibrium silicon concentration C_E at the liquidus (solid line) at a given surface temperature T (dashed line). Vapor flux renders the Si concentration in the alloy into a supersaturated value C_L; Temperature T + ΔT corresponds to the point at which the entire VLS system is in equilibrium. Reused with permission[64].

A similar method has been used for this work to develop the SnO_2 nanowires. In other words, the used method is called the 'High-Temperature Compensation' (HTC) method. However, as a nanowire growing substrate, black Si has been used, which offers a great deal of high aspect ratio reaction favoring sites for the nanowire growth. Further details are covered in section 3.1.

2.4.1 Nanowire nucleation method: Controlling parameters

The controlling parameters of VLS have been nicely summarized by G. Dubrovskii et al. in his book '*Nucleation Theory and Growth of Nanostructures*'[72]. In short, the classical approach to explaining the nanowire nucleation phenomena has been developed on two core assumptions namely, low critical temperature, T_c and supersaturation of a metastable phase. Therefore, the entire phenomena can be subdivided into a communal of dense nuclei and a diluted perfect vapor. Unfortunately, classical nucleation theory does not always support the experimental result, hence non-classical scenarios are often observed. However, to get a feeling of how dynamic these scenarios might be, in this section, the phenomena are explained in the frame of the lattice gas model.

The nucleation theory of nanowire can be explained as a first-order phase transition with a grand canonical ensemble in thermodynamic equilibrium within a fixed volume. The process starts with the discontinuous change of density due to the condensation of supersaturated vapor into liquid droplets accumulated on the substrate in a colder region. The thermodynamic properties of the system depend upon the equilibrium relation of state among pressure (P), volume (V), temperature (T), atomic density (n), interatomic potential (U), and chemical potential (μ). The configuration part of the statistical sum of a grand canonical ensemble for all non-identical atoms (*i, j*) can be written as:

$$\Xi(\mu, N_T, T) = \frac{1}{k_B T} \sum_{\alpha_i} \exp\left(\sum_{i=1}^{N_T} \mu\alpha_i - \sum_{(i,j)} U\alpha_i\alpha_j \right) \quad (1)$$

Where,

- k_B = Boltzmann constant
- N_T = Total number of sites

In the simplest case, the local potential field acting upon the atom in a given site '*i*' can be approximated by mean-field approximation with average occupation 'θ'.

$$\sum_{(i,j)} U\alpha_i\alpha_j \cong -U_0\theta_{\alpha_i} \quad (2)$$

Where, U_0 is the effective energy of attractive interactions for reaction site '*i*' and θ can be defined as:

$$\theta = \frac{N}{N_T} = \frac{k_B T}{N_T} \left(\frac{\delta \ln \Xi}{\delta \mu} \right)_T \quad (3)$$

Here, N is the total number of molecules in the system which is always smaller than the number of the reaction sited.

Plugging equation (2) into (1) leads to diagonalization of the statistical sum:

$$\Xi = \left[1 + \exp\left(\frac{\mu}{k_B T} + \varphi\theta\right) \right]^{N_T} \qquad (4)$$

Here, φ is the dimensionless interaction constant.

The method utilizes the metal droplet which is liquid during growth. Nanowire growth and radius are determined by those droplets while the nanowire length is related to time. SnO_2 nanowire growth mechanism based on VLS was explained by Sberveglieri and Comini et al.[73]. A similar approach has been followed to produce SnO_2 nanowires for this work.

3 Experimental Setup and Methodology

In this chapter, an overview of all the experimental setup used for different measurements has been presented. It has been started with a SnO_2 nanowire fabrication setup. Then the gas mixing system used extensively for characterization is discussed. The chapter also covers the special application evaluation set up built for fire alarm and explosive detection applications. Lastly, the fire alarm verification set up which has been built at DBI as a partial requirement to fulfill the European Union Horizon 2020 SMOKESENSE project has been addressed.

Acknowledgments and contributions

The experiments carried out for the thesis is conducted by Mr. Adib. However, Mr. Adib also acknowledges the contribution of all the forerunners of the group, who already developed the Nanowire fabrication setup and gas mixing setup up to a fine state. The sensor housing used for UV KAMINA was produced by Mr. Augustin, which has been used extensively during this study. The test at DBI has been conducted by Mr. Jörg Volk from JVI GmbH as part of his responsibilities as a participant in the SMOKESENSE project symposium.

3.1 SnO$_2$ nanowire fabrication set up based on VLS method

A quartz tube within an oven is needed to produce the nanowire. An arrangement is necessary to have a fixed pressure and carrier gas flow to maintain the desired environment for the process. As shown in Figure 13(a) piezoelectric vacuum gauge controller from the MKS company has been used to control the pressure. A Jumo LR 316 has been used as a temperature controller for the oven. To control the gas flow two Mass Flow Controllers (MFC) are necessary. One of them has been used to maintain constant carrier gas Ar and the other one to provide O$_2$ during the oxidation phase.
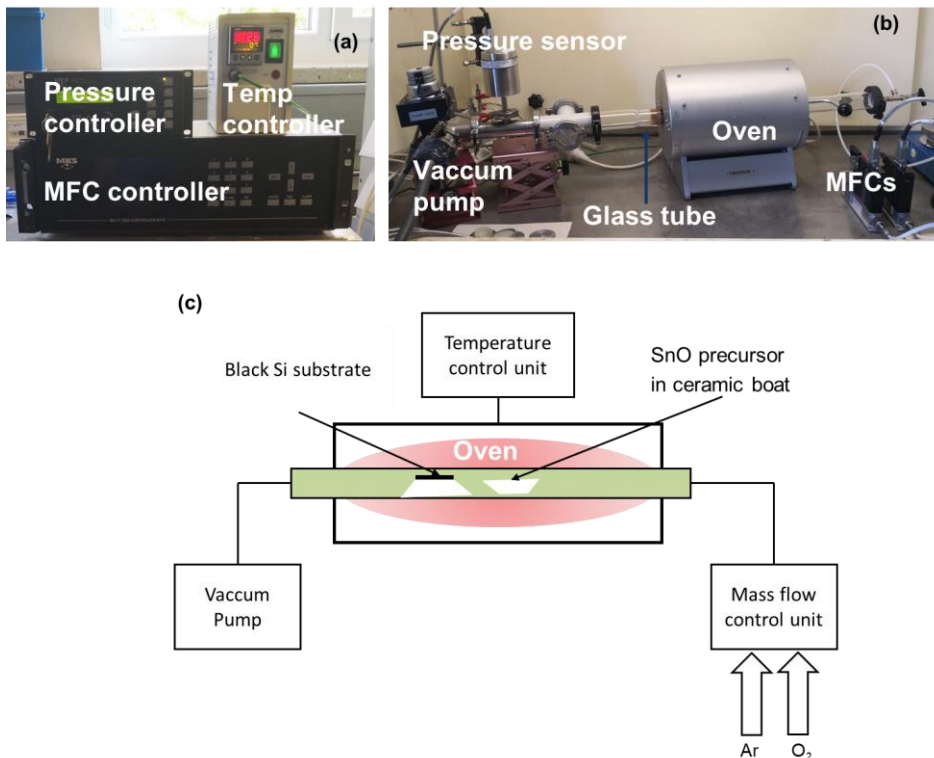
Figure 13: SnO$_2$ nanowire production set up. (a) For the SnO$_2$ nanowire growth pressure, temperature, and gas flow need to be controlled precisely. The pressure has been controlled using an MKS pressure controller. The temperature has been controlled by the Jumo temperature controller and the gas flow has been controlled by MFC (Mass Flow Controller). (b) The oven heated up to 950°C, wraps the glass tube where the nanowires are produced. For the feedback control of the pressure, the vacuum pump is placed at the outlet and the two MFCs controlling the O$_2$ and Ar flow are placed at the inlet of the gas tube. (c) The schematic of the setup. The Black Si has been used as the growing substrate placed in a colder region where the vapor may condense.

SnO precursor and substrates need to be located within an alumina boat placed at the central part of the oven as shown in figure 13 (c). Dissociation reaction happens within a temperature range of 900 °C to 1040 °C according to the following equation:

$$2SnO\ (s) \xrightarrow{\Delta H} Sn\ (l,\ g) + SnO_2\ (s) \qquad (i)$$
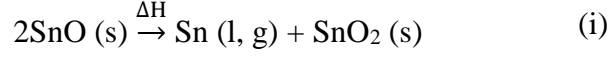
The process happens in a constant flow of inert gas (Ar) which flows in the reactor since the beginning of the heating cycle. Then the Sn vapor is carried to the substrate at a colder region where it condenses. The consequent introduction of an oxygen flow promotes the crystallization of the SnO_2 nanowires. Grown nanowires have been characterized using Scanning Electron Microscopy (SEM) and X-Ray Diffraction (XRD). A typical process flow looks as shown in table 1.

Table 1: Process flow of a typical SnO₂ nanowire production cycle

Experiment steps	Temperature °C	Pressure mbar	Ar Flow SCCM	O₂ Flow SCCM	**Time** minutes
Step 1	300	0	100	0	15
Step 2	300	0	100	0	15
Step 3	1040	0	100	0	40
Step 4	1040	300	100	0.5	60
Step 5	15	300	100	0	05
Step 6	15	1000	500	0	10

As reported by Comini and Sberveglieri et al.[73], SnO precursor decomposes into SnO_2 (solid) and Sn (liquid and vapor) by following equation (i) and carried by the carrier gas, Ar to the nanowire growing substrate. Sn vapor condenses on the substrate and appears like droplets as shown in figure 14 (a), where normal Si substrate has been used. At dissociation temperature, a large part of the Sn transforms into SnO_2 nanocrystal as shown in figure 14 (b). Very few amounts of SnO_2 wool-like whiskers or SnO_2 nanowires are seen at different places on a Si substrate as shown in figure 14 (c) and 14 (d) respectively. Si substrate lacks sufficient reaction sites and free surface energy according to the Gibbs-Thomson relationship.
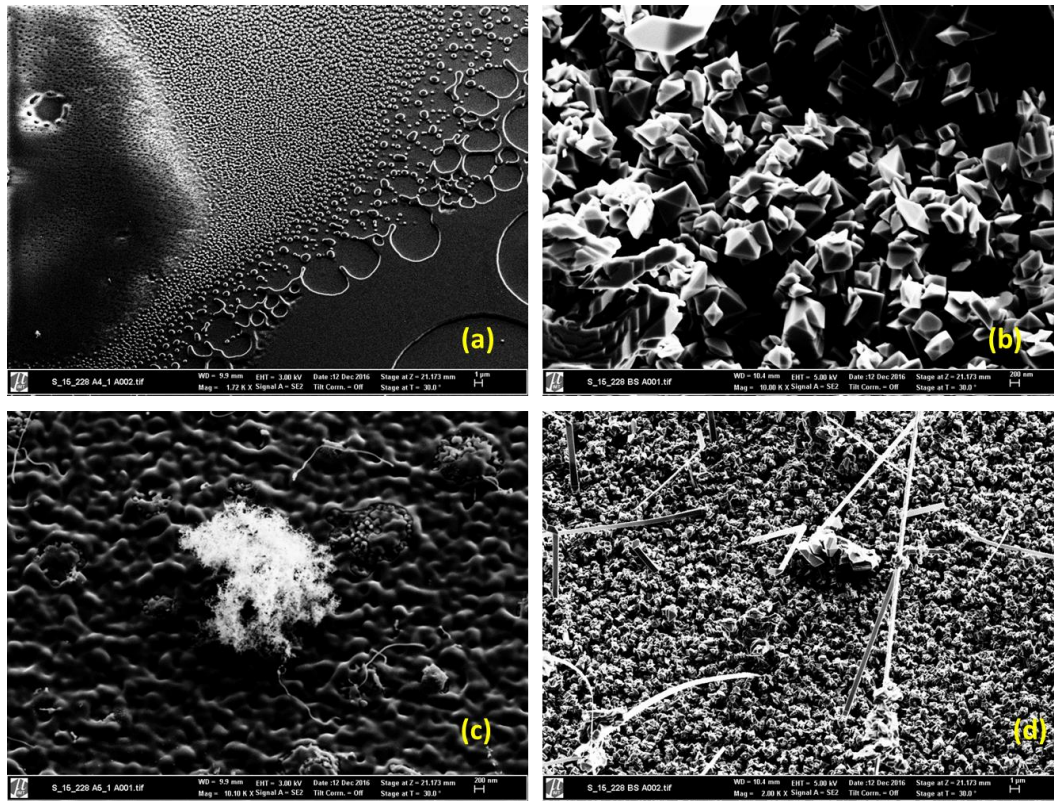
Figure 14: (a) Sn droplet on Si substrate. (b) Sn droplets transform into SnO$_2$ crystals. (c) SnO$_2$ wool-like whiskers grown on the substrate. (d) Very few nanowires grown on the Si substrate

To improve the nanowire quantity and achieve better control over nanowire size, gold-sputtered Si substrate was investigated as well. In this case, the Sn droplet wets the growth front initially and Au island acts as a growth nucleus. The introduction of O$_2$ favors the SnO$_2$ nanowire growth as well. The average nanowire diameter and length achieved using the method was 62 nm and 120 nm respectively as shown in figure 15. Even though this method offers better control over nanowire size, the quantity of nanowire is very much limited. In some areas on the substrate, the nanowire did not grow at all due to the high density of Sn droplet creating strong capillary force with the surface. Consequently, the nanowire amount was not sufficient to cover multiple KAMINA sensors. Additionally, the introduction of Au island sputtering steps can be expensive for the final product.
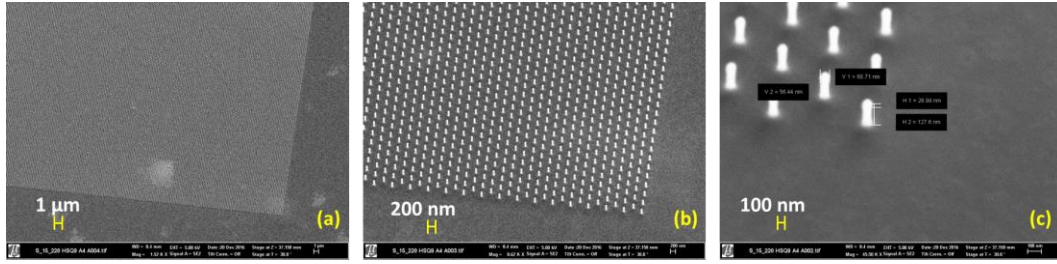
Figure 15: SnO₂ Nanowire grown with the help of the Au island. The average nanowire diameter achieved was 62 nm and length 120 nm.

As an alternative to Au island, high aspect ratio black silicon substrate was investigated later on. Black silicon is an etched Si substrate having sharp tips, which favor the formation of initial nuclei. The Black-Si (figure 16 (a)) has been produced by the cryogenic etching process of silicon using SF_6. Reactive Ion Etching (RIE) chamber needs to be cooled down to 163K and gas flows into the chamber need to be initialized with the flow of SF_6 (65 SCCM), O_2 (44 SCCM), and Ar (50 SCCM). The high Oxygen content leads to a self-passivation of Si during the process. This self-passivation layer masks the Si locally from etching and creates vertical Si-structures scattered across the etched surface. For the process, a dry etching cluster consists of Oxford RIE Plasma-lab System 100 with ICP 380 sources has been used. The device is designed to work at a high frequency of 13.56 MHz combined with a high vacuum chamber. These high aspect ratio Black-silicon structures provide optimum 'Gibbs free energy'[74].

Different stages of nanowire growth are captured in figure 16. To investigate the growth process step by step, five separate experiments were conducted providing different dissociation times. The complete process flow has been discussed in table-1. At step 3 the dissociation reaction is triggered and Ar flow carries the Sn (l) to the substrate. Figure 16 (b) has been captured at the 2nd half of step 3, showing the black silicon spikes are covered with Sn. Tips of the black silicon substrate favor accumulation of nuclei as shown in figure 16(c), which has been captured at the end of step 3 and beginning of step 4. Figure 16(d) has been captured at the beginning of step 4 and is presenting an area where a lot of SnO_2 nuclei have been accumulated on the top of the Black silicon tip. All of these sites are potential nanowire growth starting points. Figure 16(e) has been captured from the same substrate but the first half of Step 4. In that location, several early nanowires already start growing horizontally. Figure 16 (f) is the end of the process scenario after the additional Oxygen reacts with the liquid Sn and produces more SnO_2, which acts as growth nuclei.
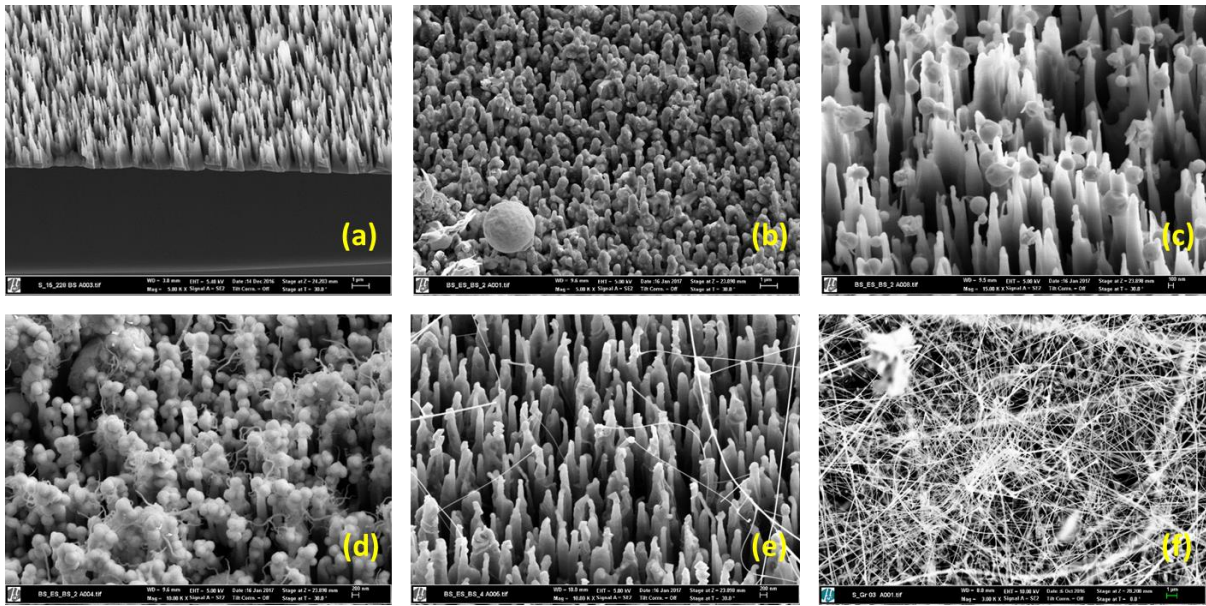
Figure 16: (a) Black-Si substrate having a high aspect ratio. (b) Sn vapor condenses on black silicon substrate. (c) A ball-like formation of SnO₂ crystal on top of the Sn-covered black silicon substrate. (d) SnO₂ nanowire growth starts from the ball-like nuclei. (e) Several nanowires start growing vertically (d) Final stage: After the complete growth process, highly dense long nanowires were produced.

The development comes out from the liquid phase and rapidly grows due to the short distance between their nascent part and nutrient droplets. Until the complete usage of the liquid Sn, the growth process continues. After that, growth degenerates and ceased to an end, leaving a characteristic shape at the wire end as shown in figure 17.
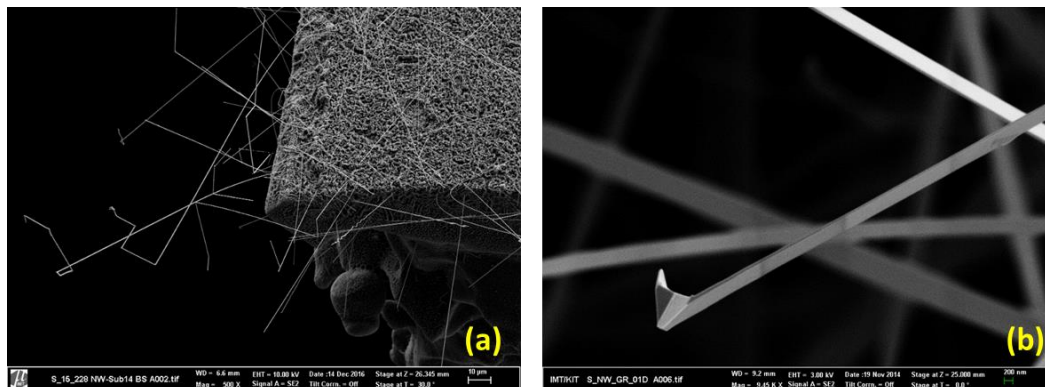
Figure 17: (a) SnO₂ nanowire growth at the edge of the substrate (b) Typical nanowire ending at the end of the degeneration process.

However, getting an ideal nanowire growth requires absolute control on the complete process. A 10% increase of SnO_2 may result in complete coverage of the black-Si substrate with the Sn layer as shown in figure 18 (a). The substrate looks like a honeycomb structure. Consequently, as the black-Si tips are covered, they no longer facilitate the growth of nanowires as shown in figure 18 (b), where very few nanowires growth is visible.
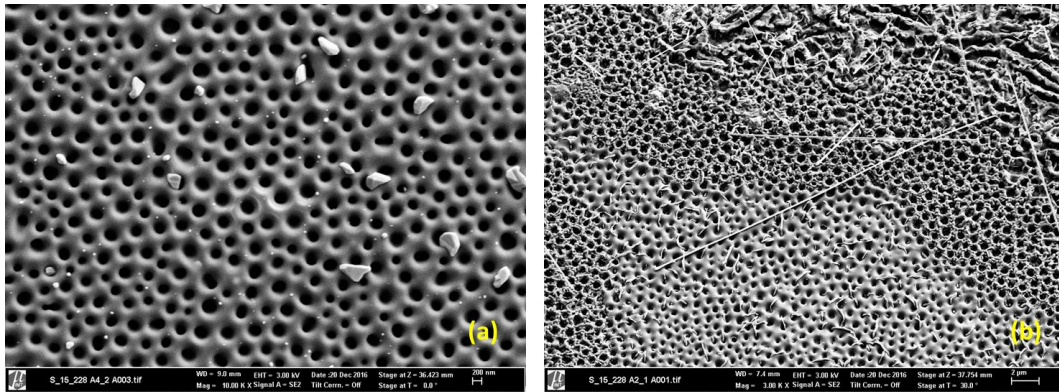
Figure 18: (a) High coverage of Sn droplet covers the complete black-Si tips and form a honeycomb-like structure. (b) As the black-Si tips may no longer facilitate growth, very few nanowires were found at the end of the process.

The primary objective of the nanowire production process development was to optimize the nanowire production volume and produce enough nanowire for at least 50 KAMINA sensors. The methodology can be considered as a proof concept for the mass production process. For the e-Nose application, nanowires need to be dispersed on the sensing electrodes. After the collection of nanowires from the substrate, they need to be submerged within an Isopropanol solution followed by an ultrasonic bath to achieve good nanowire distribution within the solution. Then the nanowires are drop-casted on the sensing electrode using a syringe. Nanowires having a smaller diameter than 100 nanometers tend to break into particles during sonication and therefore do not support a percolating connection between two electrodes. So, the preferred nanowire diameter is >100 nm. Optimization of the process to achieve a high nanowire quantity will be discussed in section 6.1. Additionally, further details on the nanowire dispersion on the KAMINA sensor will be discussed in section 4.2.

3.1.1 Overall control of the nanowire fabrication setup

To trigger the dissociation reaction of SnO precursor, 900°C temperature is needed in a low-pressure condition. Therefore, it was very important to precisely know the temperature at the exact position of the precursor within the oven. To achieve that, the oven temperature was verified using a reference sensor (Testo 901). The reference sensor was positioned in the middle of the oven while the oven was heating up to 1100°C. As the test setup was not completely thermally isolated, there is a difference between the controlled temperature by the oven and the actual temperature measured by the reference sensor. As shown in figure 19 (a), the oven heats up linearly. However, to achieve 900°C in the middle of the oven, the set temperature of the oven needs to be 950°C. As shown in figure 19 (b), the temperature at different positions of the oven was mapped precisely to ensure that the SnO precursor experience 900°C, and the nanowire growing Black-Si substrate is placed in between the temperature region of 870°C and 900°C.

(a)   (b)
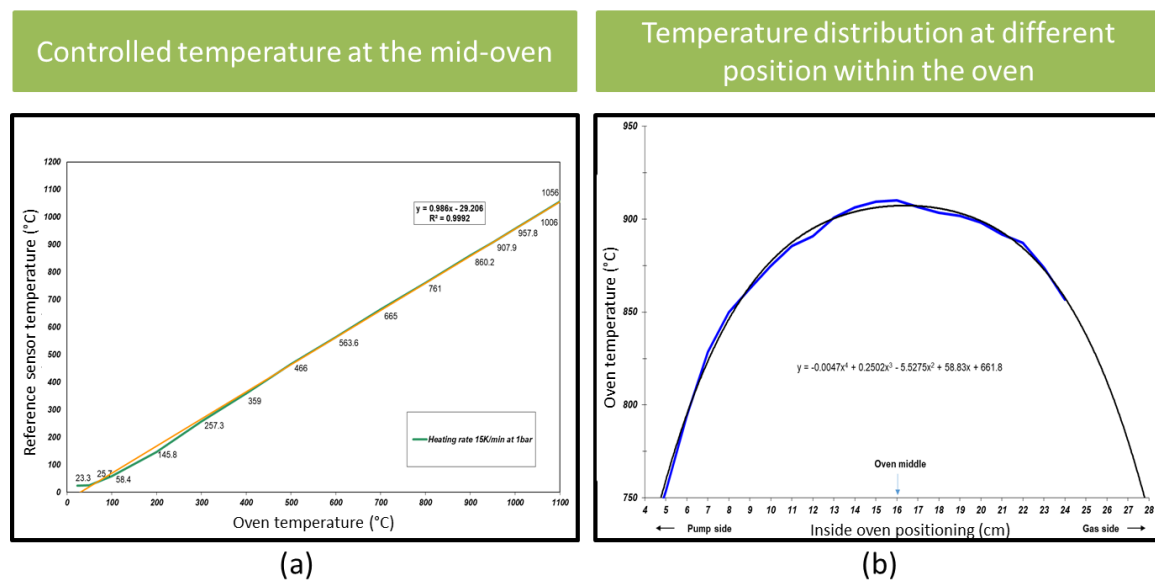
Figure 19: Precision temperature control to ensure the dissociation process of SnO particle precursor at 900 °C. (a) The set temperature and actual temperature relationship are linear. However, there is a difference of rough 100°C, which is caused by the non-optimal thermal insulation of the setup. (b) The temperature profile within the oven.

3.2 Sensor housing for the characterization

As shown in figure 20, a steel housing has been used for the gas measurement. The housing has been designed in such a way, that there is no leakage and it can maintain laminar

flow while exposing the sensor to the target gas concentration. For UV illumination there is a Sapphire-glass window to maintain UV irradiation from an outside UV-LED from a 5 mm distance.
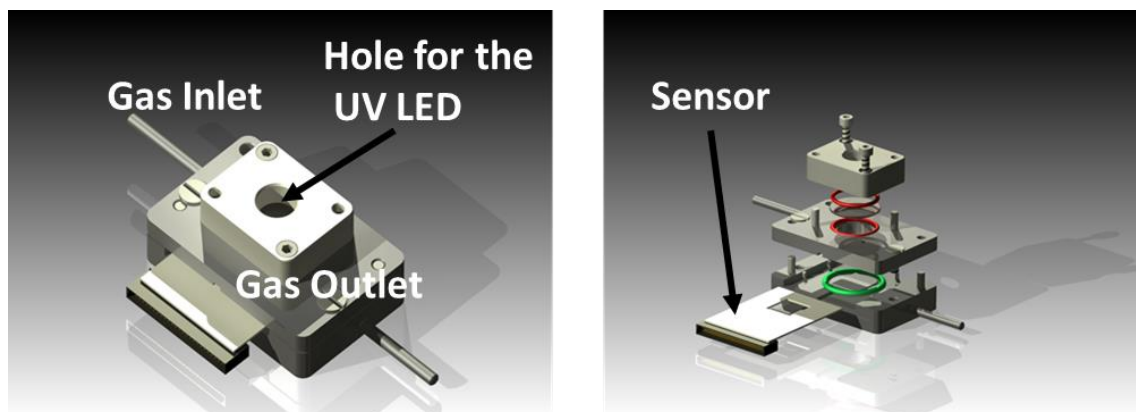
Figure 20: CAD drawing of the housing optimally designed for the gas measurement. On top of the housing, there is a hole to accommodate the UV LED.

3.3   Gas mixing system used for characterization

To deliver the target gas to the gas chamber a gas mixing system has been used, where relative humidity could have been varied from 0% to 100%. For control purposes, a calibrated temperature sensor and a relative humidity sensor were connected before the gas box. The sensor's performance parameters like dynamic detection range, sensitivity, response time, etc. have been investigated using this setup. The schematic of the setup is presented in figure 21.

The Gas Mixing System (GSM) has two parts, one has been used to maintain a reference air condition and the other part is used to supply a specific gas concentration. Both parts were having a separate air humidifier to maintain the target humidity. In total there are eight Mass Flow Controllers (MFCs) having a maximum range from 10 SCCM to 1000 SCCM. Dynamic MFC range is helpful to achieve a wide variety of gas concentrations from ppt level to ppm level. Synthetic air created by a 'Zero air generator' has been used as the carrier gas for both sides of the system. At a time, 6 gas bottles can be connected with the system which is marked as G1 to G6. An example measurement sequence is presented in table 2.
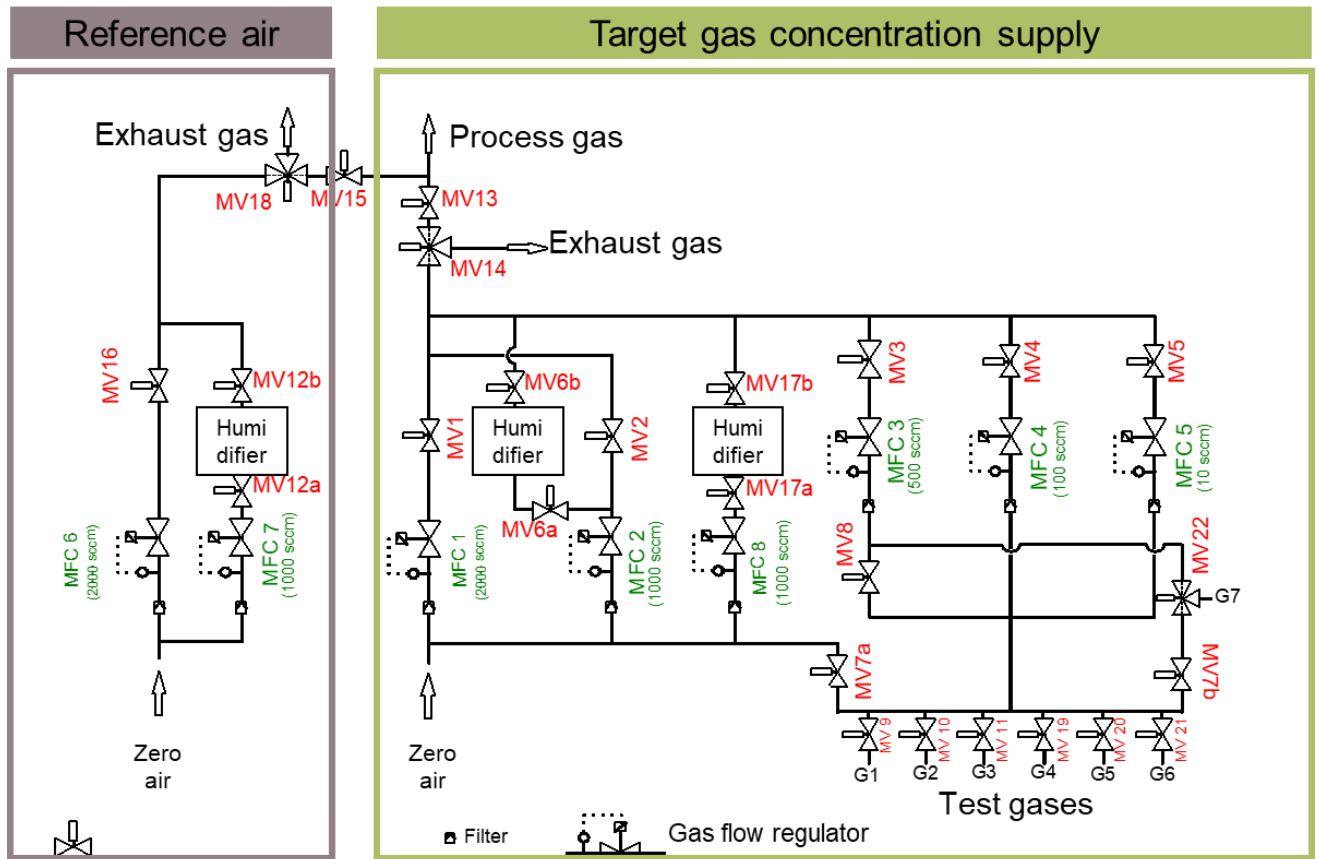
Figure 21: Gas Mixing System (GMS). The left portion marked as 'Reference Air' of the system was used to maintain the reference airflow with fixed relative humidity. The right portion marked as 'Target gas concentration supply' was used to prepare a certain gas concentration.

To achieve a target gas concentration at specific relative humidity, the following equation has been used:

$$T_c = \frac{B_c \times G_f}{D_f + W_f} \qquad (i)$$

Where,

$T_c = Target\ gas\ concentration\ (ppm)$
$B_c = Bottle\ concentration\ (ppm)$
$D_f = Dry\ air\ flow\ (sccm)$
$W_f = Wet\ air\ flow\ (sccm)$

Target relative humidity can be achieved by varying the ratio between D_f and W_f.

For example, if a sensor needs to be characterized at a room temperature and atmospheric pressure with a 500-ppm gas bottle concentration at 1000 SCCM flow, then a typical gas measurement protocol is presented in the following table:

Table 2 Typical gas measurement protocol

Target condition at 25°C and atm. pressure	Time (min)	MFC1 (sccm)	MFC2 (sccm)	MFC3 (sccm)	MFC4 (sccm)	MFC5 (sccm)	MFC6 (sccm)	MFC7 (sccm)
Air 50% RELA-TIVE HUMIDITY	30	0	0	0	0	0	500	500
Air 50% RELA-TIVE HUMIDITY + 1 ppm gas	15	498	500	0	0	2	0	0
Air 50% RELA-TIVE HUMIDITY	30	0	0	0	0	0	500	500
Air 50% RELA-TIVE HUMIDITY + 10 ppm gas	15	480	500	20	0	0	0	0
Air 50% RELA-TIVE HUMIDITY	30	0	0	0	0	0	500	500
Air 50% RELA-TIVE HUMIDITY + 100 ppm gas	15	300	500	300	0	0	0	0
Air 50% RELA-TIVE HUMIDITY	30	0	0	0	0	0	500	500
Total time (min)	165							

3.4   Application investigation set up: Fire alarm

As this work also covers the work package of the SMOKESENSE project, the first target application was the fire safety module. Therefore, the sensors had to be trained, tested and verified as a better alternative than a typical fire alarm. The setup is shown in figure 22. 'Reference air' having a fixed relative humidity has been used as the carrier flow from the Gas Mixing System (GMS). A glass cup with very good thermal insulation was placed on a hotplate, which has been used to generate a heated smell from a different material at elevated temperatures.

As a SMOKESENSE project requirement, the sensors had to be calibrated and tested with the burning smell response of Poly-Ethane (PE), Poly-Propane (PP), PCB, wood, cotton, and paper. As early fire detection was the fundamental objective, determining the lower detection limit of such a sensor as a fire alarm at a relatively lower temperature was the key parameter. An optical fire alarm has been used as a reference fire alarm which was fixed at the gas outlet of the chamber. The outcome of the work has been published separately[11].
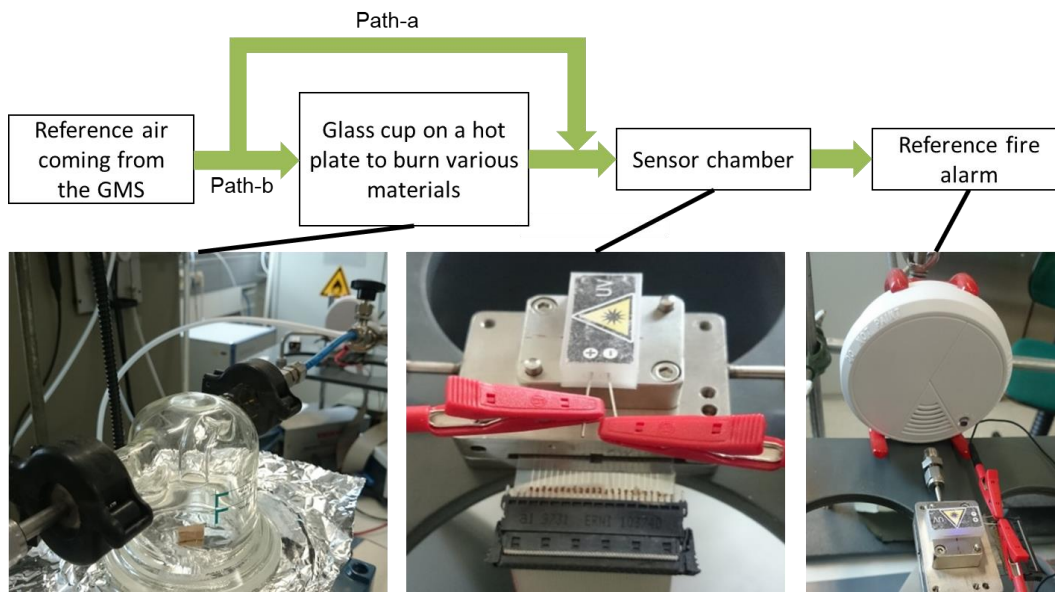
Figure 22 Measurement set up to characterize the sensor response as a fire alarm. A glass cup on a hot plate has been used as a burning smell accumulator. As a reference air, 50% relative humid air has been used as a reference air for typical experimental conditions.

For example, 0.1 g PCB starts showing smoke at 300 °C and the reference fire alarm sets off within 5 minutes of operation in this condition. However, the UV KAMINA sensor starts showing response at a much lower temperature at around 108°C as further discussed in section 6.3.

3.4.1   Fire alarm testing and verification set up at DBI

Within the framework of the SMOKESENSE project, work package 6 covered the testing of the prototype unit at DBI (Dansk Brand- og Sikringsteknisk Institut). DBI has a strong background in testing the state of the fire alarms for certifications. DBI also supports the product development activities to fulfill the project requirements. The test setup used for the UV KAMINA-based fire alarm at the DBI is presented in figure 18. The test objective was to evaluate the sensor and communication system under the field application condition.
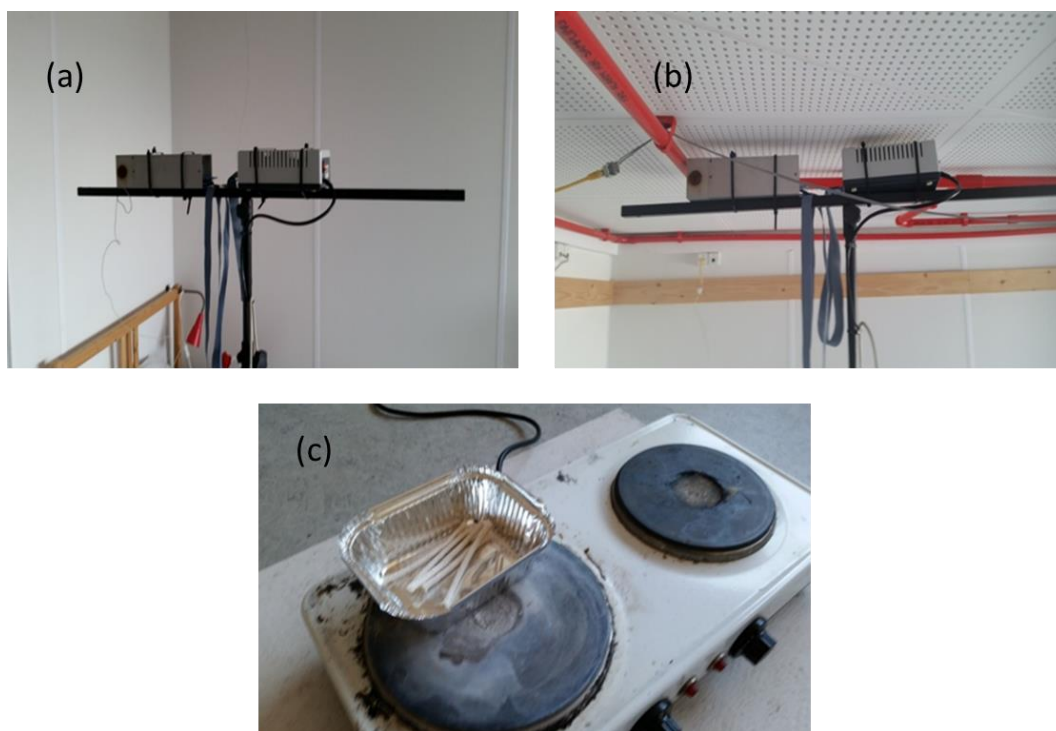
Figure 23: DBI test setup. (a, b) The sensor system was adjustable to position the sensor at different locations and different heights within a burning test reference room. (c) A typical electric stove has been used to generate a burning smell.

The setup was built to mimic an elderly person's typical room environment within a container. To simulate a fire hazard condition an electric stove was used to burn different materials. As shown in figure 19 (a, b), the sensor and measurement electronics were placed on a height-adjustable rolling stand to evaluate the sensor performance at the ceiling in different corners from the stove. The actual experimental protocol and outcome of the experiment are discussed in section 6.3.1.

3.5 Application investigation set up: Explosive gas detector

The second application investigated within the scope of the work is an explosive gas detector. The sensor was placed inside a sealed test chamber having one inlet and outlet. The gas mixing system maintained constant relative humidity and carrier air flow rate at 500 SCCM. The experiment was done at three relative humidity levels, i.e. 30%, 50%, and 70% to show the functionality of the sensor under a wide range of humidity. The target substances were placed within the vicinity of the carrier flow, at the favorable vapor pressure the substance molecule can be carried to the sensor chip operating at room temperature. As shown in figure 20(b), within a glass enclosure the target substances were

placed. The experiment was conducted in a controlled condition with necessary safety measures.
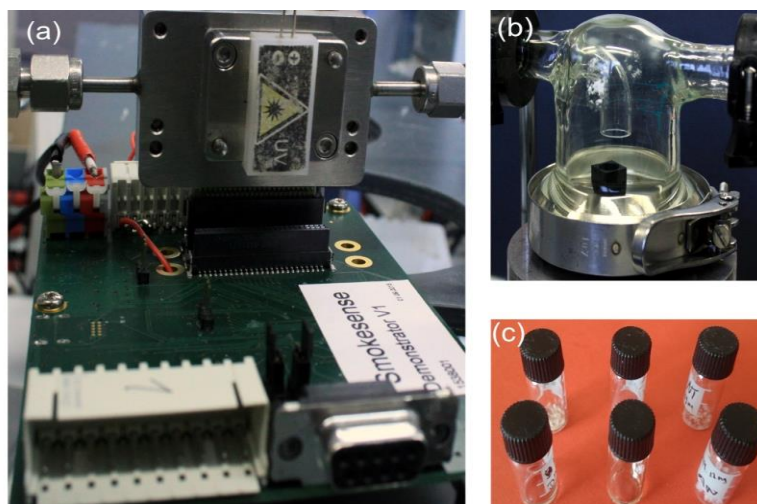
Figure 24: The experimental setup. (a) The measurement electronic and test chamber. UV is illuminated on top of the sensor. There are one inlet and one outlet. An exhaust pump sucks the fluid. (b) The sealed target reservoir chamber. Carrier airflow having specific humidity passes through the chamber. (c) The targets, which were placed within the chamber for the experiment.

3.5.1   Investigated explosive materials

Following materials have been tested with UV KAMINA.

I.   Dimethyl-methylphosphonate (DMMP):
     DMMP is an organic compound containing phosphorus. It is a colorless liquid that is widely used as a chemical warfare agent. Applications are mostly seen as a flame retardant[75] in a commercial application.

II. 2,4-Dinitrotoluene (DNT):
     DNT is an organic compound and well known as a precursor to Trinitrotoluene (TNT). Highly toxic and above the threshold limit of 1.5 mg/m^3 converts hemoglobin into methemoglobin. Widely used as a warfare compound. EPA listed DNT as hazardous waste[76–78].

III. Nitrobenzene (NB):
     Nitrobenzene is a highly toxic organic compound having a threshold limit value of 5 mg/m^3. It can also be absorbed through the skin. Additionally, prolonged

exposure may cause serious damage to the central nervous system, impair vision cause liver or kidney damage, anemia, and lung irritation. Inhalation may persuade headache, vomiting, lethargy, dizziness, and even deadly[79,80]. The US-EPA classified the compound as an extremely hazardous substance[81].

IV. 4-Nitrotoluene (4-NT):
    4-NT is a Highly toxic and carcinogenic organic compound. The material is used to produce stilbene derivatives for dyes production [82].

V. 2, 3-dimethyl-2,3 dinitro butane (DMNB):
    DMNB is a highly toxic volatile organic compound. Because of their wide use in explosive production, they are used as an explosive taggant[82].

VI. Ammonium Nitrate (AN):
    AN is mostly used as fertilizer, however, they are also used to create explosives, i.e. TNT.

Further details of the test result are covered in section 6.3.2.

4 KAMINA (KArlsruhe MIkro NAse)

This chapter starts with a brief introduction to the KAMINA system and highlights its rich historical achievements. Even though the KAMINA system managed to create a scientific breakthrough in its time, there were fundamental weaknesses in the concept, which eventually limit the sensor in the application phase. Improvement target to minimize these weaknesses has been achieved with the introduction of UV KAMINA. UV KAMINA has been developed in a way that the KAMINA system moved one step closer to a mainstream product application.

Acknowledgments and contributions

4.1 The original KAMINA: An idea

The original KArlsruhe MIkro NAse (Karlsruhe Micro Nose) was envisioned and developed by the late Dr. Goschnick and his team at modern-day IMT at KIT. The first publication related to this topic was made in 1996, where a novel multi-sensor system having 39 metal oxide sensing segments was presented[83]. Even though the publication highlights the ppb level detection of Propane and Propanol, it also provided a hint to the potential use of a pattern recognition algorithm in the future to find a fingerprint of a gas mixture. The first effective use of a pattern recognition algorithm of the microarray system has been presented in the following year[84], where the microarray sensor system was used to classify different stages of cooking a steak as shown in figure 25. Dr. Goschnick first coined the term KAMINA in 2001 at one of his publications[85], where he prophesized the potential universal use of an array-based metal oxide gas sensor system along with a machine learning algorithm. Development of the original KAMINA system was continued until 2007 and the outcome has been reported in several other publications[86–88].
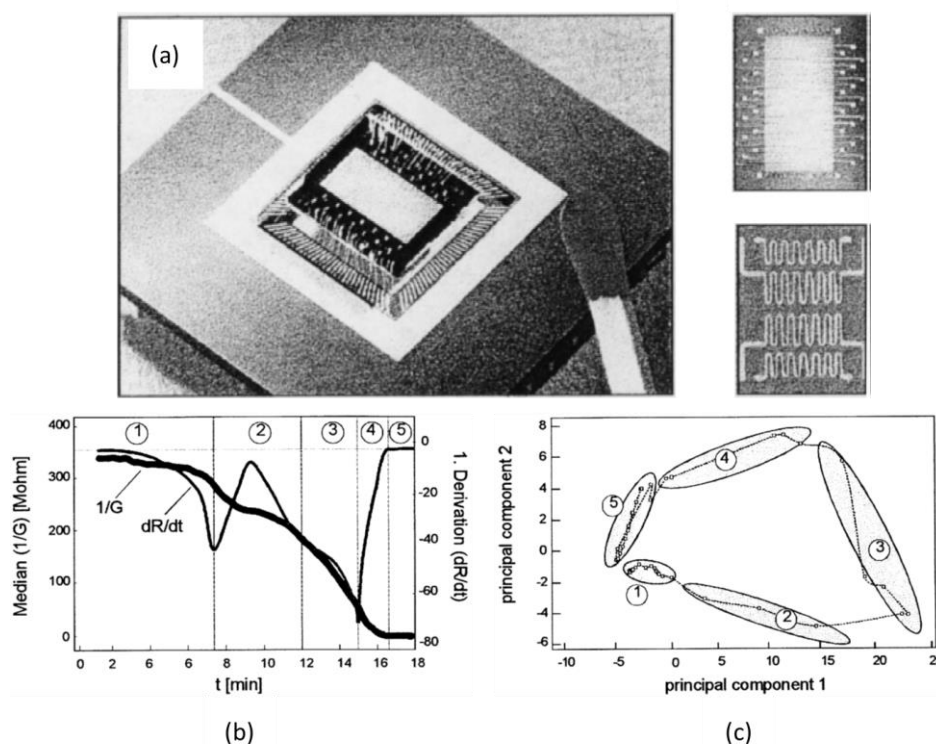
Figure 25: (a) Photograph of the microarray system, front, and backside. (b) The course of the median resistance and its first derivation during the frying of beef. The five stages correspond to meat which is 1 raw, 2 underdone, 3 well-done, 4 overdone and 5 burnt. (c) PCA score plot of the signal patterns of the frying of beef. Reproduced and used with permission[84].

Undoubtedly the idea of the KAMINA system was revolutionary. However, there were limitations.

4.1.1 System limitation of the original KAMINA

I. The complex fabrication process of shadow masking:

The sensor fabrication was done in four steps. It started with the wafer-based formation of the fundamental structure, then the separation of the sensor chips including carrier assembly, followed by the membrane deposition, and finally the annealing treatment. It required high-frequency sputtering to deposit the metal oxide film. The process has been summarized nicely in figure 26. A reactive magnetron sputtering system has been used for high-frequency sputtering. Shadow masking is used to deposit the SnO_2 nano-particle film, sensing segment electrodes, thermo-resistor structure along with four meander-shaped heating elements. Additionally, IBAD (Ion Beam Assisted Deposition) has been used to ensure thickness gradient of SiO membrane. The precursor gas is converted at room temperature to an ultrathin film of SiO and C with specific thickness defined by the bead density. Anneleaning of the microarray chip is necessary to eliminate the C from the membrane.
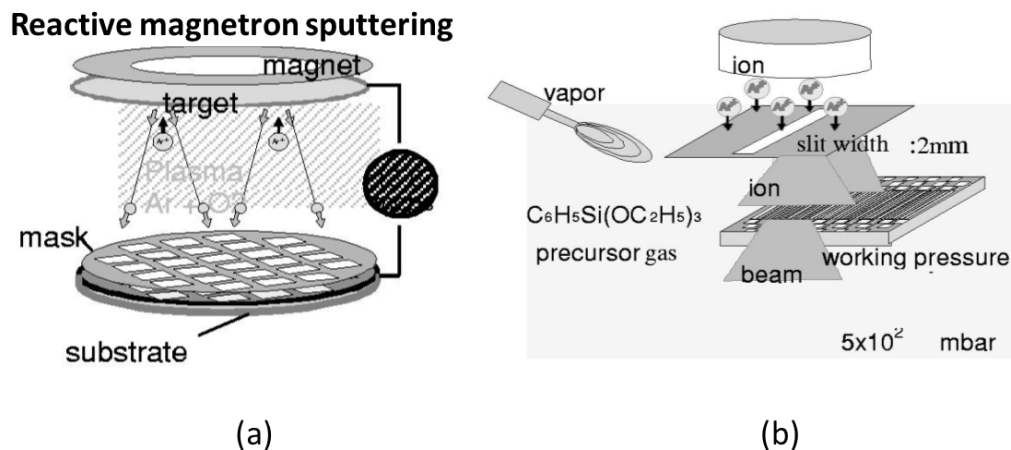
Figure 26: (a) High Frequency-sputtering: basic structure. Shadow masking is used to deposit the metal oxide film, the electrode, and thermo-resistor structure plus the four meander-shaped heating elements. (b) IBAD (Ion Beam Assisted Deposition): membrane with thickness gradient. CVD with an ion beam allows deposition of the SiO membrane. The precursor gas is converted at room temperature to an ultra-thin film of SiO and C with a thickness depending on the beam density. Annealing of the microarray chip is necessary to eliminate the carbon from the membrane and to stabilize the metal oxide crystal structure. Reproduced and used with permission[85].

The process was complex and prone to contamination during fabrication. Therefore, the process required a lot of preparation and careful handling to produce the sensor chips. To prepare the solution for the mass market, the process had to be optimized.

II. SnO₂ nanoparticle agglomeration:

Metal oxides nanoparticles including SnO_2 tend to agglomerate with the influence of environmental stimuli such as light exposure and temperature variations[89–92]. KAMINA system needed to be running at two different temperatures 250°C and 320°C to ensure a temperature gradient that favors feature extraction in the dynamic phase of the gas exposure. Due to such temperature variation, the nanoparticles change position continuously, resulting in a sensor system that needed to be calibrated very frequently. Such sensor characteristics may ruin the solution at the application level. The introduction of the SnO_2 nanowire minimized this problem at a later time.

III. Heater temperature:

The temperature gradient was an essential system requirement for the KAMINA system. The temperature gradient was maintained based on current measurement. However, the actual ambient temperature was unknown. Therefore, the same amount of voltage drop across the heater may cause different temperatures at different times. As the calibration temperature cannot be maintained across different applications, such an approach may only lead to misclassification of target gases at the application site.

IV. Complex system design:

Along with the complex heater control requirement, for a robust system, relative humidity information is also needed, as the relative humidity depends on the ambient temperature. Water molecules interact with a Metal oxide sensor as an oxidizing component. Therefore, along with a temperature sensor, a relative humidity sensor is also required to maintain target performance over the lifetime of the application.

V. High energy consumption:

The sensor needed 39 electrodes and a temperature gradient between 250 and 320°C. The temperature had to be maintained for the complete operational period. For, such a high-temperature application for a single measurement the device required more than 5 mW during the measurement sequence only to maintain the heater[87]. To maintain the heat, the device needs a 5V stable supply, which is also an issue for most modern-day IoT-type applications.

VI. Siloxane contamination:

Siloxanes are a fairly new group of PCPs, comprising of a polymeric organic silicone having a backbone of alternating silicon-oxygen units with an organic chain attached to every silicon atom, conversing them a low surface tension, physiologic inertness, high thermal stability, and a smooth texture[93,94]. Siloxane is widely present in an indoor envi-

ronment, where gas sensors are mostly used. Metal oxide sensor operating at high temperature is prone to Siloxane contamination. At high temperature, such material may create an additional layer on the metal oxide sensor, which may contaminate the sensor in a way that factory calibration may not hold after the surface characteristics of a Metal oxide surface is altered.

Apart from these issues, there were other limitations like precise gold wire bonding requirement, thermal isolation requirement during package design, etc. makes the overall system very complex and expensive for the target application.

4.2   SnO$_2$ nanowire based KAMINA

The next breakthrough of the KAMINA system was achieved after the introduction of the SnO$_2$ nanowires instead of SnO$_2$ nanoparticles as the sensing element. There has been a series of publications between 2007 and 2009, where it has been presented[95–97]. With this approach, the first two limitations (Complex fabrication process and nanoparticle agglomeration) of the KAMINA system were improved. The sensor fabrication method became easier and monocrystalline SnO$_2$ nanowires offer better material stability and sensitivity due to stable conduction path through the crystalline structures and more reaction sites respectively. However, the KAMINA system performance was still limited by the complexities causing due to heaters.

4.2.1   System introduction of the SnO$_2$ nanowire based KAMINA

As the sensing element, the random distribution of metal oxide nanostructures on 39 Pt electrodes was used. Nanowires offer a higher surface to bulk ratio enabling highly sensitive gas interaction. As the nanostructures approach the material's Debye length makes the whole nanowire a charge carrier accumulation zone. The nanowire layers render the space between the nanofibers irrespective of individual nanowire dimensions as shown in figure 27. To achieve sufficient differentiation in the response of the sensor elements two gradients were applied across the microarray, namely lateral variation of the surface temperature of the sensor and gradient distribution of nanowire density across the sensing segments.
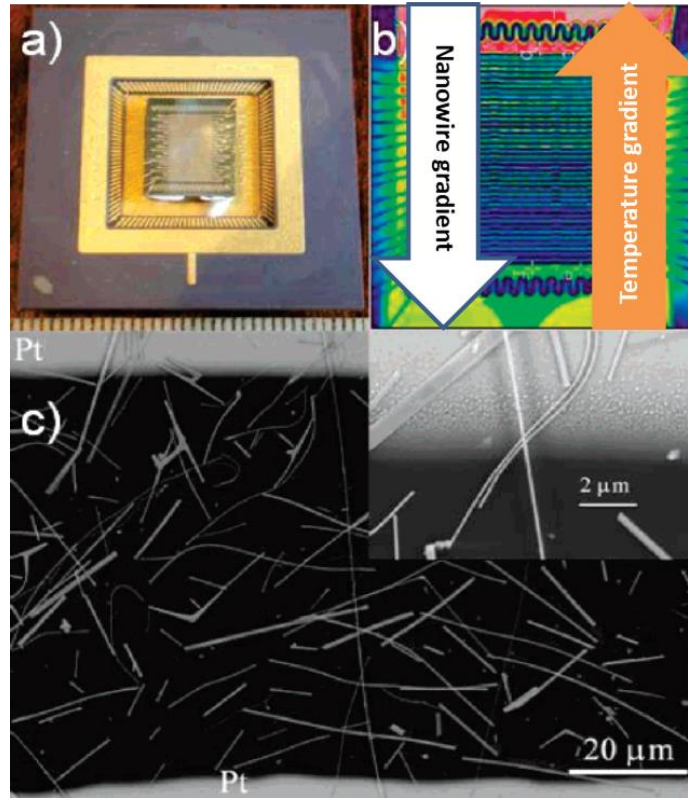
Figure 27: (a) KAMINA microarray chip having 39 Pt electrodes along with SnO₂ nan-owire as the sensing elements, (b) IR image of the chip under temperature gradient, (c) SEM image of SnO₂ nanowire between platinum electrodes. Reproduced with permission from ACS Nano letters,[98] © American Chemical Society.

The current transport via nanowire shows percolating character, meaning the conductance between two interdigitated electrodes is determined by the availability of the conduction path laid by the overlapping 1-D crystal nanostructures as shown in figure 27 (b). The electron transport through a percolating network has been qualitatively explained using a simple core-shell model as shown in figure 28(a). When exposed to reducing gases, the adsorbate induces the change of potential barrier height at the contact point between two nanowires, called a node[99], which dictates the charge transport properties through them. The electron transport in the node area follows a thermoelectric mechanism[55]. Adsorbate influences the electron transport inside an n-type SnO₂ nanowire. A nanowire having a diameter of ~100 nm and visible to ambient air can be considered as a simplistic case, where the nanowire core is surrounded by an electron depletion region, W. Additionally, the depletion width depends on the Debye length, λ_D[55], which may vary between 10-20 nm. The depletion region, W may vary due to a reduction gas interaction by $\Delta W \sim \lambda_D$ $(e\Delta V_s/kT)^{1/2}$[98]. The sensor signal for this case can be estimated as:

$$\frac{R_0}{R} = \left[\frac{D}{D - 2\Delta W}\right]^2$$

Where D is the nanowire diameter and V_s is the applied voltage.

However, for a real-world scenario, a combination of both phenomena is naturally expected. As shown in figure 28 (c), for $(e\Delta V_s/kT)^{1/2} \sim 1$ and nanowire diameter of 70-100 nm, the resistance ratio of the node is comparable to a percolating channel.
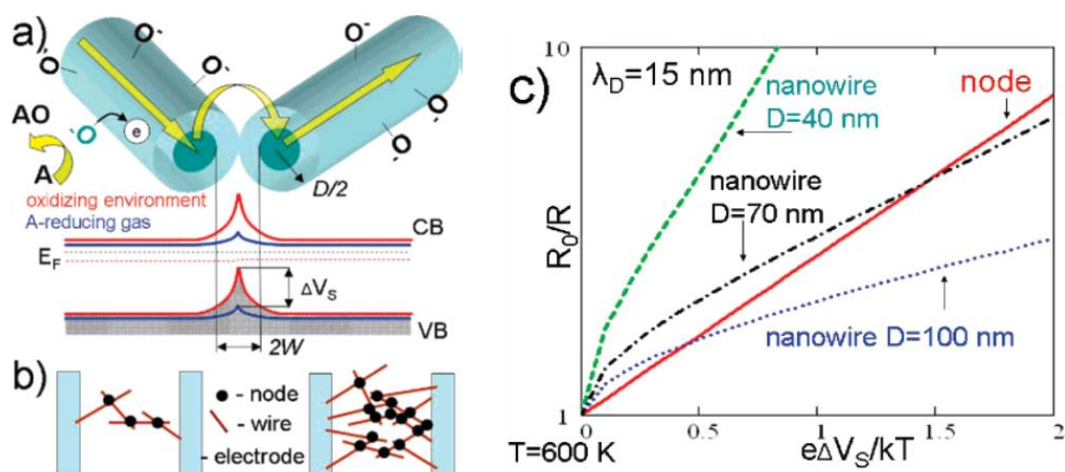
Figure 28: (a) Receptor and transduction functions of the percolating Receptor and transduction functions of the percolating nanowire net. In the oxidizing ambient, the exposure to reducing gas leads to a decrease in the contact barriers and an increase of the cross-section of the conducting channels inside the nanowires. (b) An increase in the density of the nanowires leads to an increase in the relative contribution of nodes concerning straight parts of the percolating path. (c) Comparison of the relative contribution of nodes and nanowires to the sensor signal (log scale). Reproduced with permission from ACS Nano letters[98] © American Chemical Society.

Later on, LDA[100,101] was used as a supervised multivariate pattern recognition method to translate the conductance variance of 38 sensing segments and represent them into a reduced dimension as shown in figure 29.
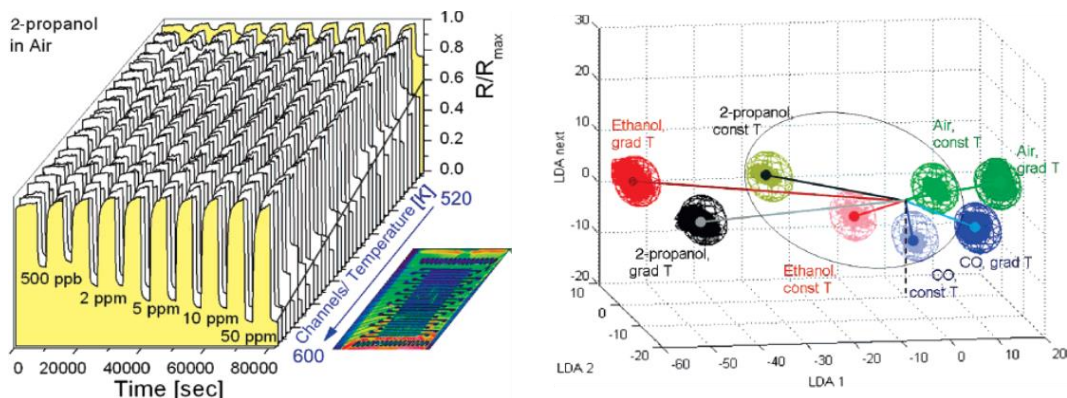
Figure 29: LDA analysis of the conductivity patterns obtained with SnO₂ nanowire-based gradient microarray at exposure to the target gases. Reproduced with permission from ACS Nano letters[98] © American Chemical Society.

Even though, the introduction of nanowires improves some of the original KAMINA system limitations, the limitations associated with the heater were still present. Therefore, the quest of UV KAMINA was started to minimize further limitations and bring the universal KAMINA eNose idea one step closer to a real product.

4.3   UV KAMINA

The UV KAMINA[11,12] has been developed with two main objectives.

I.   Minimize the limitations associated with heaters which have been an integral part of the predecessor KAMINA system. The UV KAMINA should ease the system complexity and prevent Siloxane contamination.

II.   Enable potential high-volume production of the sensor by introducing a printing technique to produce metal electrodes.

The first step to realize UV KAMINA was to characterize the UV-VIS response of SnO_2 nanowire. At room temperature, under UV illumination an abundance of electrons accumulates to the bulk surface of the SnO_2, nanowire-mat, resulting in the resistance drop. A UV KAMINA sensor array has 16 sub-sensors having 16 segment resistances as shown as a 'Bar-plot' in figure 30 (a). The 17th bar of figure 30(a) is denoting the median resistance at a certain time. Under UV illumination the median resistance of 16 sub sensor drops by 50% (figure 30 (b)). SnO_2 Nanowires accumulate oxygen at the surface by trapping electrons from the bulk[54]. A reducing gas molecule (i.e. Iso-propanol) interacts with the pre-adsorbed Oxygen or directly with the Oxide sites and free up the electron, resulting in a resistance drop. For this particular example, exposure of 100 ppm Iso-propanol reduced the median resistance from 30 MΩ   to 13 MΩ. Without excitation, the SnO_2

nanowire does not accumulate enough reaction sites on the surface, therefore without the UV Illumination, the sensor did not react to Iso-propanol at all.
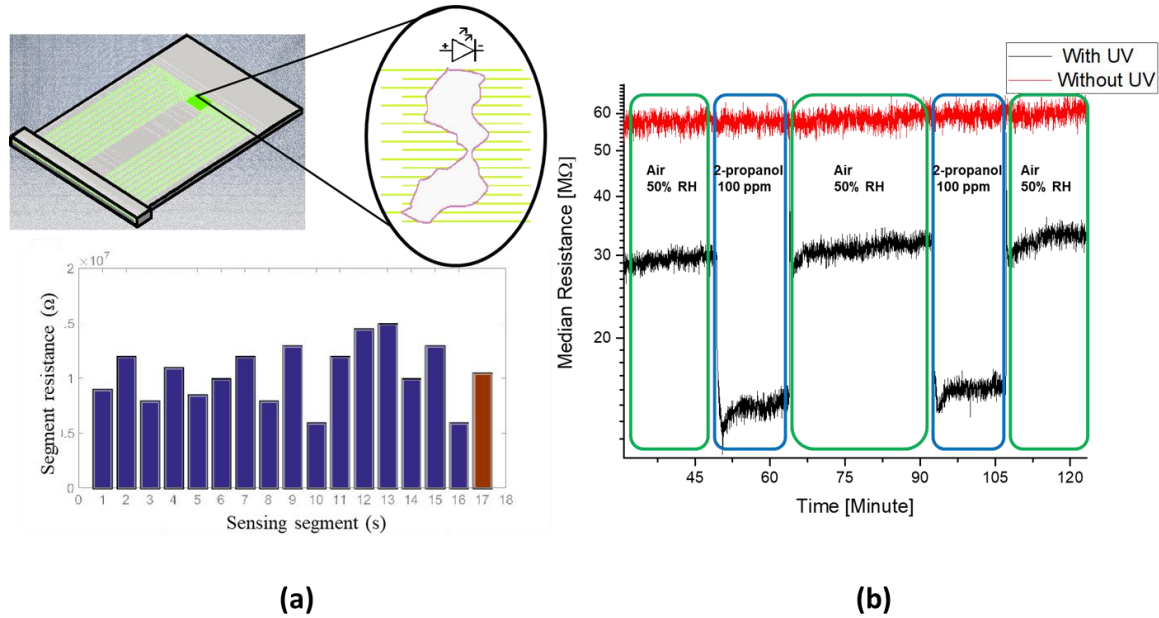
Figure 30: (a) Typical nanowire distribution in the UV KAMINA sensor is shown at the top half. At the bottom half, the resistance of 16 segments under UV illumination. The 17th bar is denoting the median resistance of 16 segments. (b) Reducing Gas response with and without UV illumination.

The influence of nanowire density variant under UV illumination has been reported by M. Augustin and M. Sommer et al.[42] separately. For that study as the sensing platform, heater based KAMINA system has been used. Nanowires were distributed from high density to low density across 38 sensing arrays. The nanowires were excited by illuminating with a separate tunable light source. The KAMINA sensor's heater was used to investigate the influence of light illumination at different temperatures up to only 100°C, which was far below the traditional heater-based KAMINA system (260°C). Sensor segments 1 to 18 had a higher density than sensor segments 21 to 38. As shown in figure 31 (a), at 20°C both high-density and low-density area shows the lowest median resistance at 365 nm. At higher temperatures, more thermal energy increases the energy density within the SnO$_2$ nanowires and contributes more free electrons within the conduction path and consequently, the resistance decreased even further. As shown in figure 31(b), at the high-density region the sensor response reaches up to 100% when illuminated with 365nm wavelength UV light. The response remained at 100% level from 20°C-100°C, indicates

that UV illumination at 365 nm minimizes temperature dependency. Under UV illumination (365 nm) the response spreads from 80% to 100% from 20°C-100°C. Therefore, for the UV KAMINA system, a high-density nanowire along with a UV LED having a 365nm wavelength has been used later on.
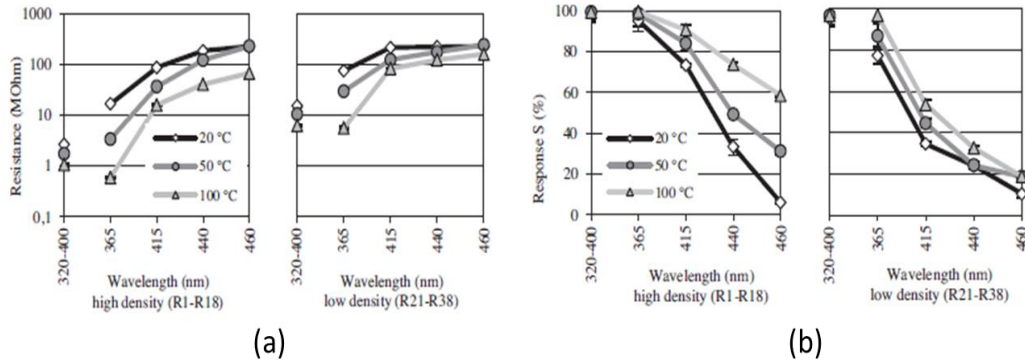
Figure 31: (a) Minimum median resistance values under the illumination of sensor segments1–18 (high-density nanowires, left) and 21-38 (low-density nanowires, right). (b) Response depending on wavelength, temperature, and electrode numbers1–18 (high-density nanowires, left) and 21–38 (low-density nanowires, right). Reused with permission[42].

The gas sensing property of the SnO_2 nanowire was covered in section 2.3.5. In short, different segment resistance responds differently due to non-uniformed nanowire distribution across segments. The irregularity is a result of the different time constant at a different segment.

4.3.1   Device fabrication method

The sensor was prepared in two simple steps. At first, the SnO_2 nanowires were produced on a black silicon substrate using the VLS method, which has been covered in sections 2.4 and 3.1 in detail. The sensor electrodes, wiring, and contact pads were printed using digital aerosol jet technology.

The interdigitated electrode structures, electrical connections, and contact pads were printed by aerosol jet (UTDoTs Auto-AJ). This digital printing technique allows for a precise and small feature size deposition of the Au nanoparticle-based ink. A detailed description of the aerosol jet technique can be found elsewhere[102]. The pattern was printed with gold ink on cleaned 0.7 mm thick glass substrates. After sintering the Au structures

at 300 °C for 5 hours in a furnace, the chip was then Ar-plasma treated to get rid of the organic residues from the printed electrodes. Feature sizes down to 10 µm can be realized, which makes it suitable for printing of interdigitated electrodes for the presented UV KAMINA sensor. Accurately defined electrodes with 120 µm width and 80 µm channel length (the difference between two adjacent electrodes) were printed with a line height of about 80-100 nm, the connection wires have been printed sub-sequentially 5 times to achieve a nominal thickness of about 450 nm. The chip has 17 interdigitated electrodes resulting in 16 electronically open segments. The sensitive region area was 16 mm^2. From the EDX shown in figure 32, the electrodes are consisting of Au. 91.55% with 4.4% possible residues. L and M series energy shell of Au shows impulse response at 0.26 keV and 2.12 keV respectively.
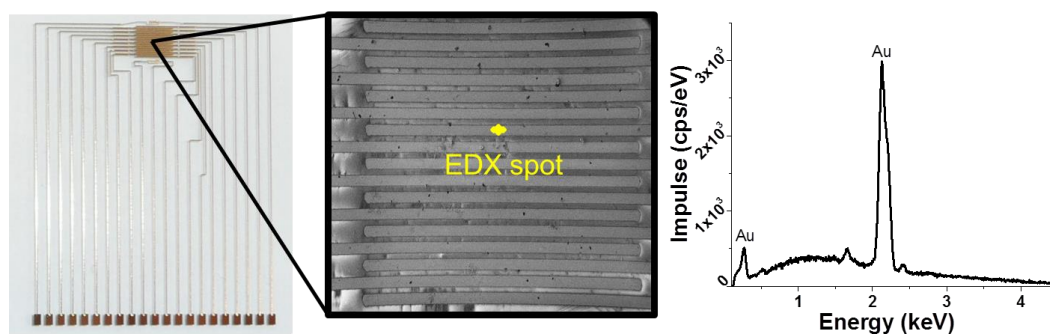
Figure 32: Aerosol jet printed UV KAMINA and EDX measurement on the gold electrodes.

As explained in Chapter 3, SnO$_2$ nanowires have been grown from SnO precursor (SnO powder) on black silicon substrates following the VLS method. The nanowires were collected from the Black-Si substrate and then a nanowire solution having approximately 1% solid in Isopropanol was prepared. After sonication for 15 minutes, the solution was deposited on top of the printed Au electrodes by solution drop-casting method using a syringe. The nanowire distribution on the electrode array was random having high density. Different initial resistance levels were shown for different segments due to the unique time constant of different percolating conduction path[103]. The prepared chip was then connected with an electronic device, which measured the change of segment resistance. The electronic device was developed by JVI GmbH as part of the designated work package of the SMOKESENSE project.

As shown in figure 33, nanowire solution deposition creates a percolating path between sensing electrodes. It creates potential barriers at the wire-to-wire junction and dictates

the gas response[104]. Consequently, the conductance of the sensor changes with the nanowire network density. The conductance path ultimately governs the response time and discrimination capabilities due to different gas response time constant. The theoretical understanding of the nanowires' percolating conduction path has been nicely summarized with a simulation model by M. A. Alam et al.[103].
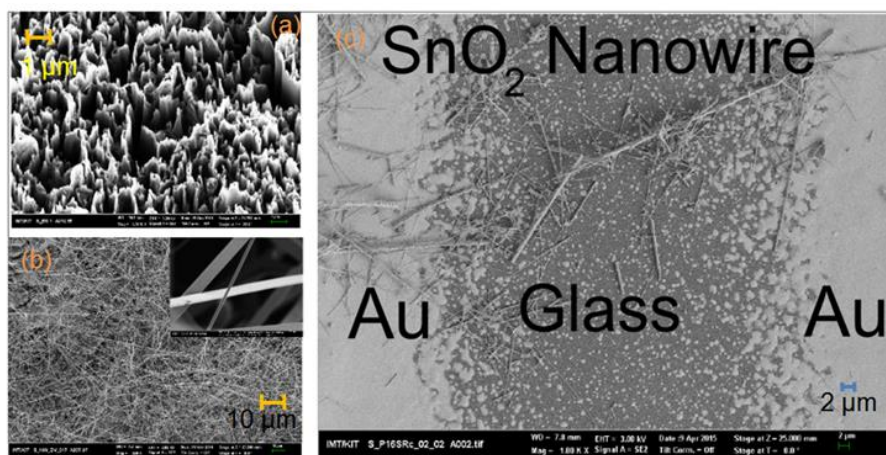
Figure 33: (a) SEM image of black silicon substrate used for nanowire growth. (b) SEM image of SnO₂ nanowires grown on the black silicon. (c) Randomly dispersed nanowire on Au electrodes. A percolating SnO₂ nanowire network is formed between two electrodes.

4.3.2   UV KAMINA as eNose

The gas response of multiple sub sensors of the UV KAMINA was then used as an eNose application. The eNose functionality of the UV KAMINA is presented in figure 34. When the sensor system is exposed to gases like Isopropanol, CO, and Benzene all sub sensors react to the gases having different time constants as shown in figure 34(a), which helps to find a unique pattern of different gas response. Different gas exposure events were classified using the LDA classification algorithm. Except for air, the last 50 data points of other target gases were used for the LDA model. For Air, 15 data points from the end of each air response curve have been considered for the LDA. The Sum of real parts of eigenvalues, found by LDA is expressed as 'Completeness of explanation' and therefore different for different LDA data sets. The 'Completeness of explanation' of this LDA model is 89%. The circles around each class center denote the 95% confidence of that class, which is a statistically calculated confidence interval based on F-test[28,30].
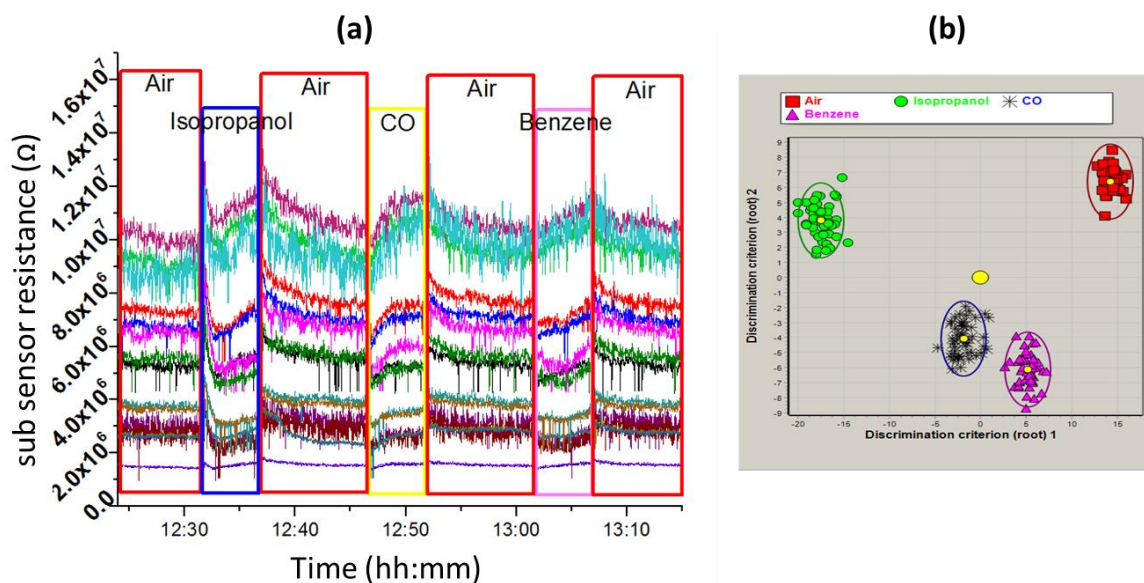
Figure 34: (a) Change of resistances of the sensor under exposure to three target gases with 100 ppm concentration diluted with 50% relatively. The response of 16 segments is shown by unique colors. (b) LDA plot: Last 50 data points are considered for LDA calculation. The statistical algorithm nicely classified all the target gases.

The development of UV KAMINA based on printing technique and UV illuminated nanowire helped to achieve the milestones for the SMOKESENSE project, which has been discussed further in section 6.3.1. The UV KAMINA has minimized several system limitations of its predecessor.

I. It has been reported before, that the heater-based KAMINA consumes between 4.5W to 9W [87] to maintain the appropriate temperature profile[25]. In contrast, for the UV KAMINA, the electronic maintained only 10 mA current to drive the LED at 5V, resulting in 50 mW of power consumption. Therefore, the introduction of UV excitation improved the power consumption by a factor of 180.

II. As there is no heater involved, the sensor is not prone to be contaminated by Siloxane, which improves the lifetime and overall stability of the sensor. It also allows the use of the sensor in an explosive environment. Such application has been presented in section 6.3.2.

III. As the device doesn't have to be thermally isolated, printing technology can be used on different substrates without strong thermal isolation requirements and may potentially improve the cost-benefit. The UV does not require any special control due to thermal management, which makes the system design very simple.

However, the UV KAMINA performance is limited by the Schottky barrier between SnO_2 nanowires and gold electrodes of different percolating conduction paths. This leads the work to UV Chem-FET, which has been covered in Chapter 5.

5 UV Chem-FET KAMINA

In this chapter another exciting KAMINA system concept has been introduced, which improves one of the shortcomings of UV KAMINA caused by the Schottky barrier between SnO_2 nanowires and metal electrodes. A simulation model has been developed additionally to facilitate the fundamental understanding of the device characteristics. Finally, the sensor has been demonstrated as eNose.

Acknowledgments and contributions

Even though UV KAMINA was already one step forward towards a real-life application, the performance of the sensor can be improved.

The target area of improvement can be expressed as follows:

> **Schottky barrier:**
> On the sensor chip of the UV KAMINA, the nanowires are lying on the metal electrodes randomly while creating a percolating connection between two electrodes. The Schottky barrier formed between semiconductor SnO_2 nanowire and metal electrodes introduces an additional barrier in the conduction path, which eventually limits to use of the full potential of the SnO_2 nanowires. Several fundamental characteristics of the sensor depend on the Schottky barrier, including response time, recovery time, and sensitivity.

To target this issue an alternate approach has been proposed having an array of FET-like structures along with a SnO_2 nanowire mat as a gate under UV illumination. The new KAMINA system has been named 'UV Chem-FET KAMINA'.

5.1   Working principle of the Chem-FET

In the presented alternative approach, a FET-like structure has been developed, where the drain and source are arranged on Si substrate as shown in figure 35(a). Within the source and drain, a SnO_2 nanowire mat needs to be placed without creating an ohmic conduction path between the source and drain. Under forward bias, the I-V curve represents the conductivity through the Si substrate conduction path. Si has a UV (365 nm) absorption coefficient of 1×10^6 (cm^{-1}) at 25°C. Therefore, as shown in figure 35(b), under UV (365 nm) illumination the conductivity increases. As explained in section 2.3, SnO_2 nanowire is predominantly an n-type semiconductor. n-SnO_2 under UV illumination accumulates Oxygen at the surface by trapping a portion of electrons from the bulk[54]. As the work function difference between Si (4.6 - 4.85 eV)[82] and SnO2 (4.8 eV)[105] is minimal and doesn't create a significant Schottky barrier, the rest of the electrons within the bulk of SnO_2 may also contribute to the direct conduction path. Therefore, when an n-SnO_2 nanowire mat is placed under UV illumination as shown in figure 35(c), it boosts the conductivity of the direct conduction path between the source and drains via Si substrate. When a reducing gas interacts with the pre-adsorbed Oxygen-ion on the bulk n-SnO_2 nanowire, an equivalent number of electrons is released from trapping and contributes to the conduction path while increasing the conductivity, which has been shown in figure 35(d). The opposite may happen for a target gas that Oxidizes. An array of such devices is used to develop the UV Chem-FET KAMINA sensor.
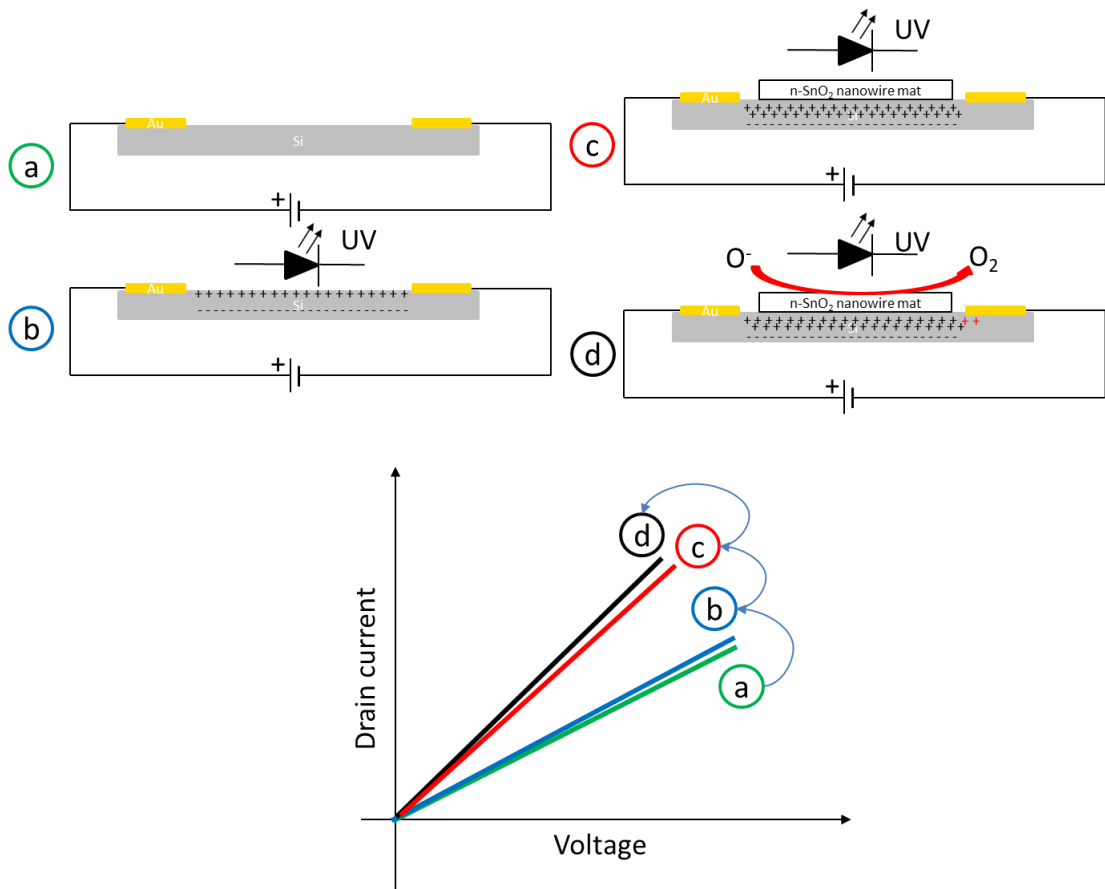
Figure 35: Working principle of a UV Chem-FET sub-sensor. (a) A biased source and drain defined the conduction path via Si substrate. (b) Under UV illumination the drain current increases due to UV (365 nm) absorption. The absorption coefficient of Si is 1×10^6 (cm^{-1}) at 25°C. (c) When n-SnO$_2$ is placed between the drain and source, the n-SnO$_2$ nanowire mat contributes more electron to the conduction path and the drain current, I_d increases. (d) When a reducing gas interacts with the n-SnO$_2$ nanowire mat, it releases more electrons, which eventually contributes to the increase of the drain current.

5.1.1 Supporting simulation results

Additionally, a simulation model has been developed to support the Chem-FET development process and gain an overall understanding of the sensor characteristics. The simulated model has defined the required Si wafer's carrier charge density and channel length. The simulation model can be divided into two parts. At first, the free charges generated within the SnO$_2$ bulk material due to UV illumination have been simulated as shown in figure 36. When the bulk nanowire mat thickness is considered to be 800 nm, under UV illumination (365 nm) electric charge density is increased within SnO$_2$ based on transfer matrix optical modeling[106]. As expected, the charge density is highest near the surface.
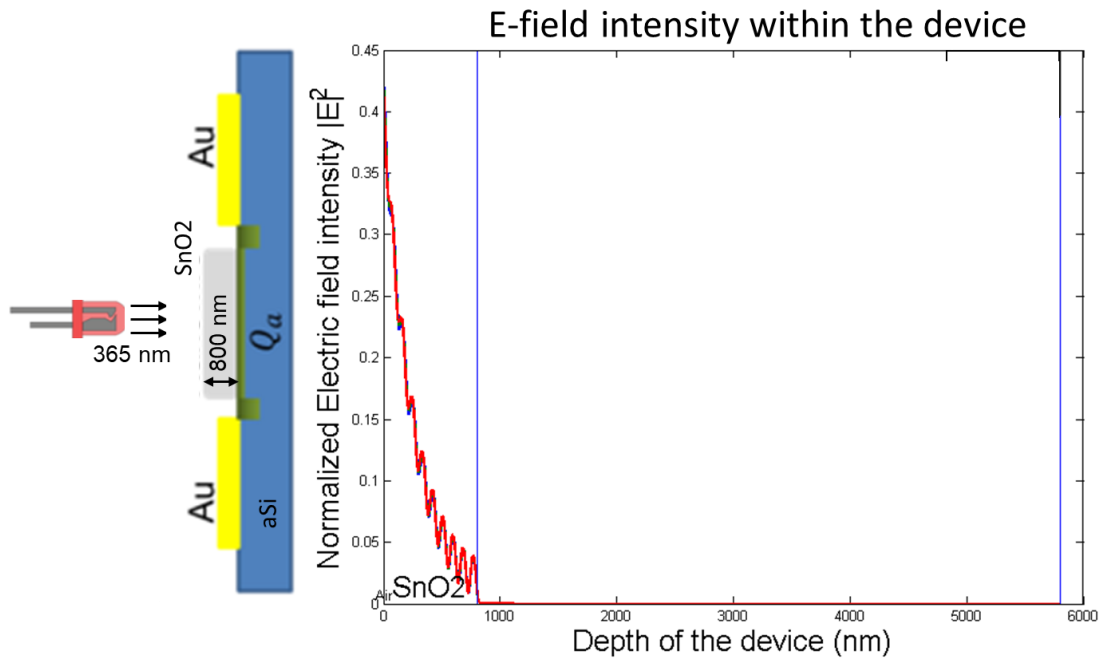
Figure 36: E-field intensity within a single UV Chem-FET under UV illumination. Charges are confined within the SnO₂ layer of 800 nm.

Furthermore, a FEM Simulation model has been developed to realize the hole concentration generation under the nanowire segment (Gate) using the electric field intensity information from the initial finding of the electric field within the SnO_2 nanowire region under UV illumination. As shown in figure 37 (a) without UV illumination, an n-type SnO_2 nanowire mat does not attract enough holes under the channel. However, under UV illumination, the SnO_2 nanowires generate free carriers on the nanowire surface, which attracts the holes from the Si substrate. The simulation model predicted the hole concentration may increase resulting in a significant conductivity increase for the device.
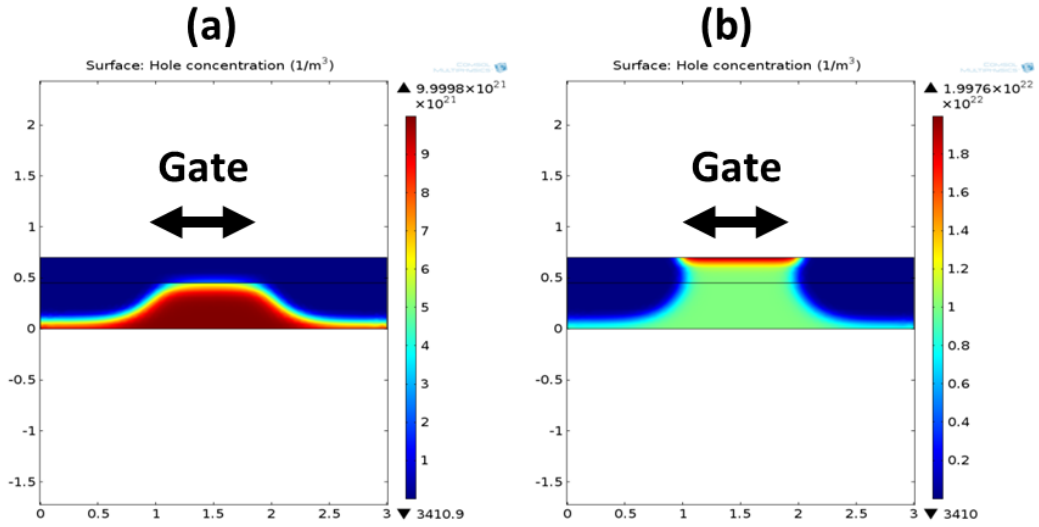
Figure 37: FEM Simulation model of a UV Chem-FET sub-sensor. (a) Without UV illumination, the gate underneath the SnO$_2$ nanowire mat shows a hole concentration of 1×10^{21}. (b) In contrast, under UV illumination, SnO$_2$ accumulates more holes under the gate, which works as a channel for the device during operation.

5.2 Device fabrication method

The electron beam lithography technique at IMT, KIT offers flexibility during the early prototype phase. Therefore, the e-beam lithography technique is used to produce the drain and source of sub-devices having 1 mm^2 area and 1 mm channel length. As the UV illuminated SnO$_2$ nanowire has been used as the gate, no separate gate contact development was necessary. As shown in figure 38(a), at first, 1 cm^2 Si substrate was spin-coated with PMMA at 5000 RPM followed by baking at 165°C for 30 minutes to dry the PMMA. Then the drain and source structure were written in array formation with e-beam writing, which was then developed. After that, Cr/Au pad was evaporated. Then the lift-off process leaves only the drains and sources on the substrate. These devices were then separated by laser cutting.

A uniformly grown SnO2 nanowire mat is necessary for the device fabrication, which needs to be placed between the drain and source. The SnO$_2$ nanowire mat was synthesized from SnO powder by following VLS (Vapor-Liquid-Solid) method as explained in section 2.4. In short, at 1050 °C, SnO decomposes into SnO$_2$ and Sn, and these species are carried to Black-Si substrate where it absorbs and the nanowire nucleation process starts from the top of the black silicon spikes as shown in figure 38(b).
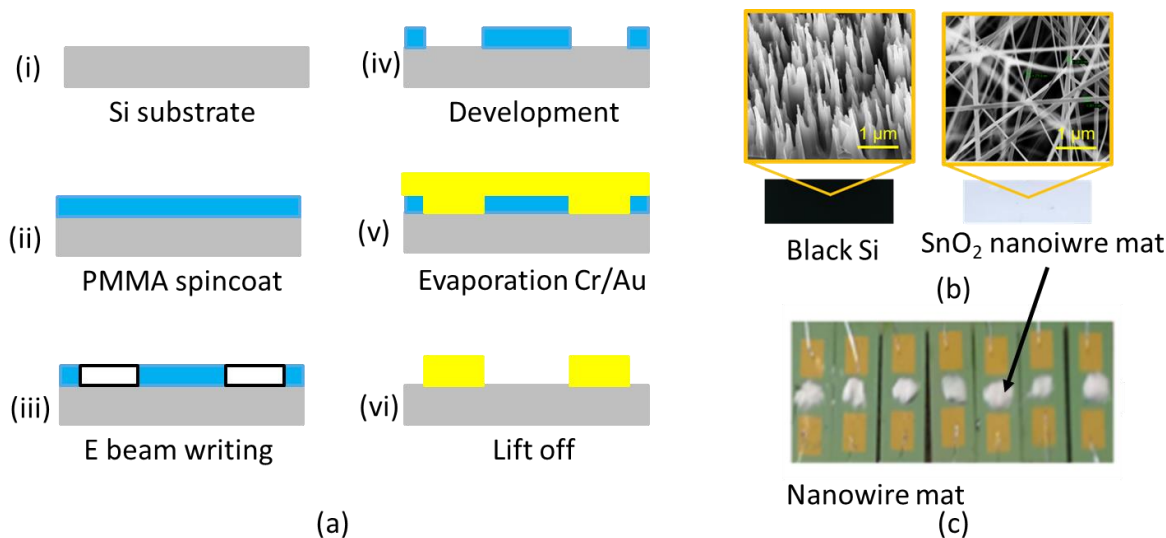
Figure 38: (a) At first, 1 cm² Si substrate was spin-coated with PMMA at 5000 RPM followed by baking at 165°C for 30 minutes to dry the PMMA. Then the drain and source structure were written in array formation with e-beam writing, which was then developed. After that, Cr/Au pad was evaporated. Then the lift-off process leaves only the drains and sources on the substrate (b) Left: Black silicon substrate produced by the Reactive Ion Etching (RIE) process. Right: Uniformly grown SnO₂ nanowire-mat on Black-Si. (c) UV Chem-FET KAMINA sensor with 7 sub sensors. A white nanowire mat was placed in between the source and drain without creating an ohmic conduction path.

The SnO$_2$ mat is then precisely harvested and placed between the drain and source as shown in figure 38(c). Then, an array consisting of seven sub-devices was connected with a docking sensor station by gold wire bonding. An external electronic was used to measure the change of sub-devices drain current, I$_d$ under gas exposure, while illuminated by UV-LED (365 nm).

5.3   Experimental methodology

At first, the working principle explained in section 5.1 had to be demonstrated. Therefore, the influence of nanowire on the drain current was investigated by measuring the drain current of a sub-device before and after nanowire integration. After it showed two different drain currents, in the next step influence of UV illumination on the drain current was explored. Then the sensor's gas responses were examined with different gases using the gas mixing system, i.e. 100 ppm CO, Iso-propanol, and Benzene each at 50% relative humidity and 25°C. To demonstrate the functionality of the UV Chem-FET sensor as an eNose, classification among these gases is needed. For classification, Linear Discriminant Analysis (LDA) algorithm has been used to attain the fingerprint response of the target gases as explained in previous sections. To showcase the application functionality as fire

alarm the device was tested with burning smells generated from beech and cotton heated up to 250°C.

The investigation can be subdivided into three major steps as follows:

5.3.1 Step 1: Conductivity variation under UV illumination

At first, the working principle of the Chem FET needed to be verified. Therefore, the following electrical tests were carried out to investigate the conductivity variation at following conditions as explained in section 5.1:

    I.   Conductivity without both UV illumination and nanowire
   II.   Conductivity with UV illumination and without nanowire
III.   Conductivity with UV illumination and with nanowire

The tests were performed in ambient conditions using an Agilent 4155C semiconductor parameter analyzer. The devices were connected via triaxle probes in a probe station (Cascade Microtech). The used measurement setup is shown in figure 39. A special arrangement was necessary where the 365 nm UV LED was placed just above the substrate while maintaining 5 mm height and it was made sure that the optical power density is identical for all the measurements.
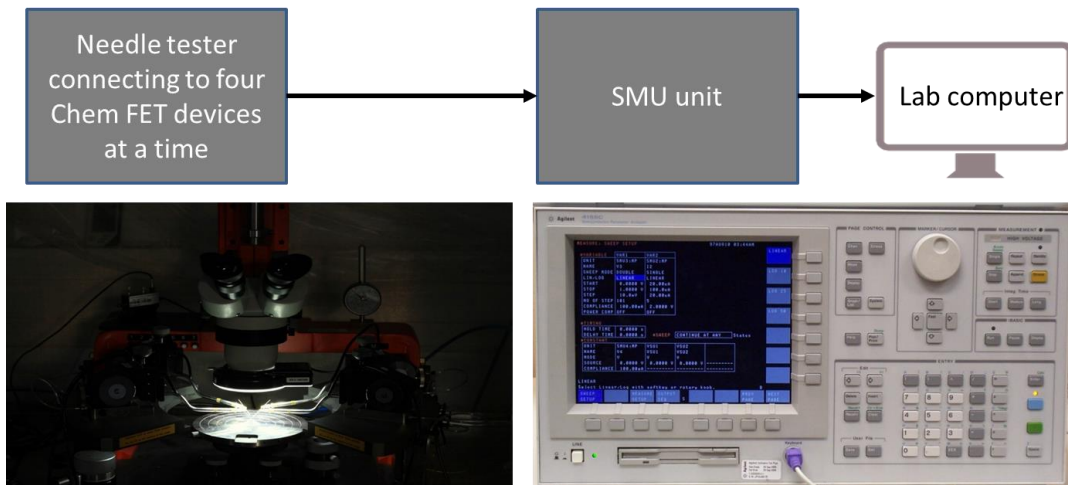
Figure 39: Needle tester set up to measure the IV characteristics of the sub-devices

As shown in figure 40, without the UV illumination and nanowire, the device current was measured from 0 to 2.25 V DC. The I-V characteristics provide the conductivity variation of the device and showcase the influence of UV excitation and nanowire. As explained in the working principle segment (section 5.1), the drain current was increased by 45 µA at 1.6V, which is the operating voltage of the used electronics. The electronic system had a

resistance resolution of 1kΩ. 45 µA current change is corresponding to a resistance change of 35 kΩ, which is well above the resolution of the electronic.
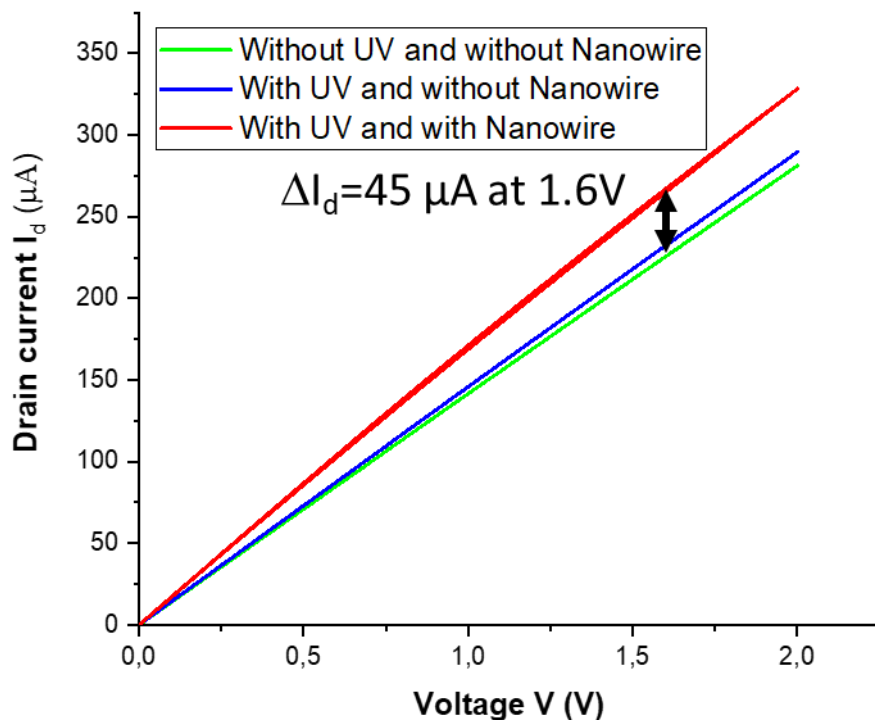
Figure 40: Drain current, I_d of a sub-device at different combinations of UV illumination and nanowire presence. Under UV illumination and in the presence of SnO_2 nanowire, the drain current increased by 45 µA

5.3.2   Step 2: Gas test in a gas mixing system

To illustrate the gas sensing ability of the new device, in a controlled environment at 50% relative humidity and 25°C temperature; 100 ppm Benzene, 100 ppm CO and 100 ppm Iso-propanol were passed through the sensing chamber. Synthetic Air with 50% relative humidity has been considered as a reference gas. The mean current of seven sub-devices is shown in the inset of figure 41(a). Signal strength for corresponding gases is calculated using the mean current shown in the inset figure. If all surface oxygen of the nanowire mat is replaced by the target gas molecules, then the gas-induced current change coincided with the change of current under UV illumination, ΔI_{UV}. Hence, the normalized gas response signal can be represented as the following equation:

$$Normalized\ Signal = \frac{I_{gas} - I_{Air}}{\Delta I_{UV}}$$

Where,

$$I_{gas} = Current\ under\ gas\ exposure$$

$$I_{Air} = Current\ under\ clean\ air\ exposure$$

As shown in figure 41, among the gases, the sensor signal was strongest for Isopropanol and weakest for CO, which is a consistent behavior of SnO_2 material's gas sensing property[107,108].
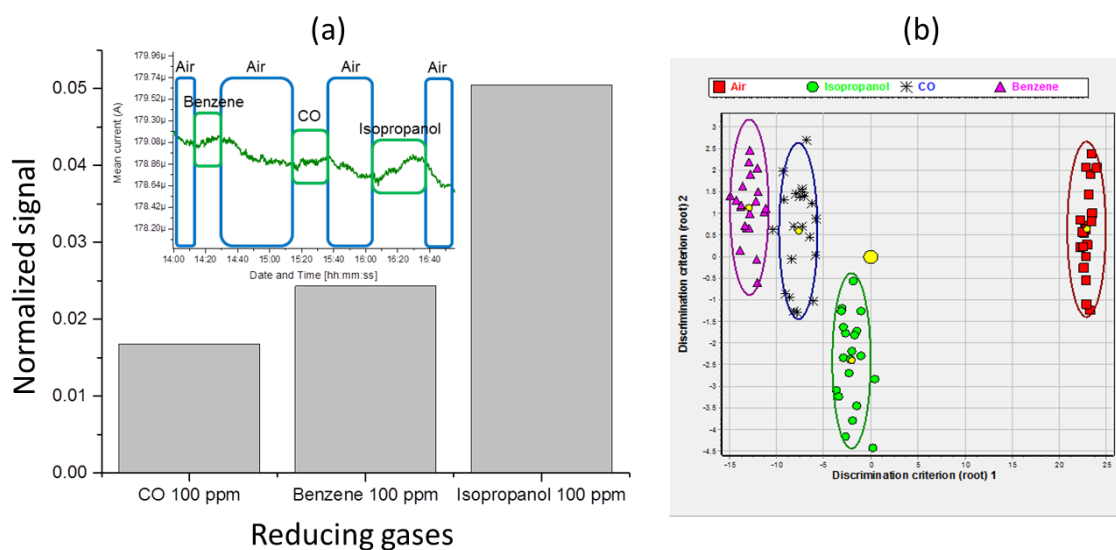
Figure 41: (a). Signal of 100 ppm CO, 100 ppm Benzene, and 100 ppm Iso-propanol at 50% RELATIVE HUMIDITY. **_Inset:_** *Change of mean current of seven sub-devices while exposed to CO, Benzene, and Iso-propanol. (b) LDA plot: Last 20 data points are considered for LDA calculation except for air. For air, 5 data points from the end part of each air section shown in the inset plot. Every dot in the LDA plot corresponds to a set of 7 current values.*

The selectivity has been characterized in terms of the 'Completeness of explanation' of the LDA model. The actual event interval is marked and the last 20 data points of a gas event of the target concentrations were used for the LDA model shown in figure 40 (b). For air, 5 data points from the end of each air response curve have been considered for the model. The circles around each class center denote the 95% confidence interval of that class. The stability of the model is calculated to be 92.6% using the 'leaving one out method'. The 'Completeness of explanation' of the model is 60%, which also indicates that the sensor is already saturated at a high ppm level concentration and cannot separate as well as UV KAMINA at such high concentration. Due to laboratory logistics limitations, ppb level measurement was out of the scope of the investigation, where the sensitivity of the UV Chem-FET is indicated to be prominent.

5.3.3 Step 3: UV Chem-FET KAMINA as eNose

To investigate the potential of being used for fire alarm applications, the device was tested with the burning smell of beech and cotton. The experiment was done at fixed 50% relative humidity. The setup schematic is presented in figure 42, which is very similar to the test setup explained in section 3.4. At first, reference air was passed to the sensor. Then in a parallel gas path, Beech (0.44 g) and Cotton (0.10 g) was heated to up to 250 °C for 5 minutes within a closed chamber. Then the smell was carried to the sensor with the help of a carrier airflow at 500 SCCM as 2 minutes pulse. As shown in figure 41, the responses of all the sub-sensors were very fast and acted immediately. For both Beech and Cotton, the initial strong response gradually weakened as the gas concentration reduced.
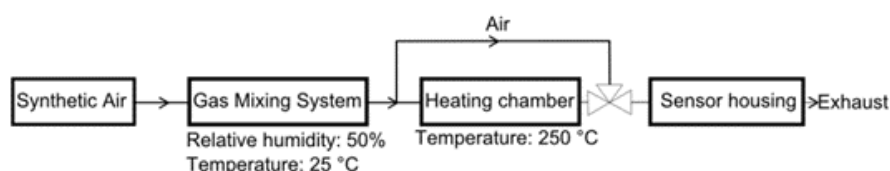
Figure 42: Experimental setup for the heated smell test of Beech and Cotton. Initially, the heater was heated to 250 °C. Then Beech and Cotton were placed on the hot plate, which then carried to the sensor as 2 minutes pulse between two purging air periods

The sensor responded to the gas produced from the materials at the elevated temperature of the substance's as shown in figure 43. The Chem FET response is truly a gas response and not a hot air response, which can be argued based on the following observations:

1. If the response was due to the hot gas flow, then the conductivity of the devices should have been increased, as additional temperature increases the absorb energy density within the device.
2. As shown in figure 43(b), the Beech and Cotton burning smells were classified successfully by the LDA, which indicates that the sensor response to the overall smell change.

For the LDA, 20 data points from the middle of the burning phase region have been considered for Beech and Cotton. For class 'Air', 10 data points from the last part of every air event were considered for the LDA. As shown in figure 42 (a), all the sub-sensors showed a fast response and fast recovery to the target smells. The system successfully classified all the target smells as shown in figure 42 (b). The 'Completeness of explanation' of the model is 94.6%. Using the 'Leave one out method'[109], the model stability is calculated to be 90.5%.
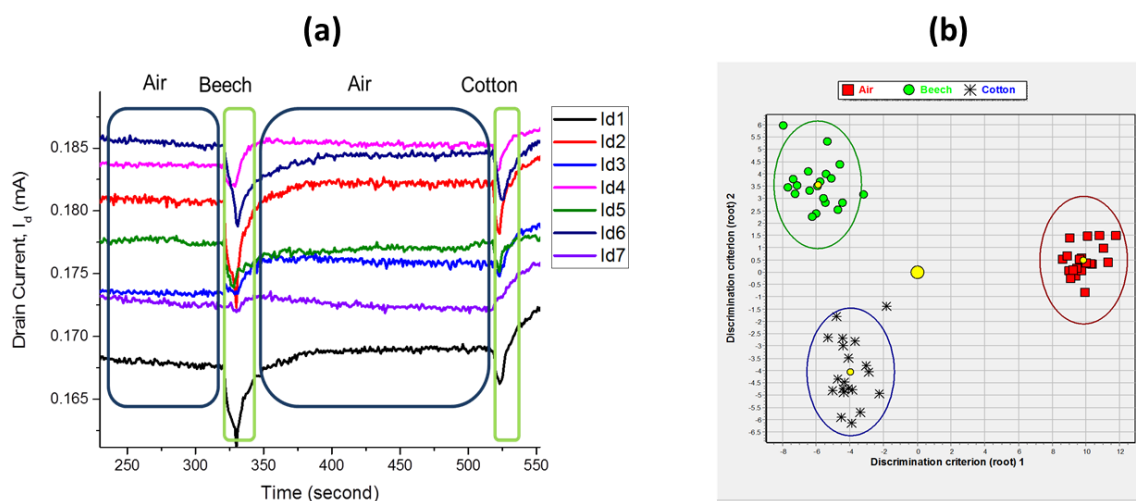
Figure 43: (a) Change of drain current as a response to target smells change of heated Beech and Cotton at 250 °C. Air with 50% relative humidity has been used reference gas in between two scorched smells as a reference gas (b) LDA plot: Smell classification using 20 data points from the highest response area has been considered. It has successfully classified three different kinds of sensor response, i.e. Air, Beech smell, and Cotton smell at 250 °C. Every dot in the LDA plot corresponds to a set of 7 current values from 7 devices.

With the presented results, it can be justified that the UV Chem-FET KAMINA may also be useful as a burning smell detector. As the SnO_2 nanowire is only in contact with the Si substrate, there is no significant work function difference. SnO_2 is acting as a gate to facilitate the channel underneath only. Therefore, the sensor reaches a stable condition much quicker and reacts faster. A detailed performance comparison is presented in Chapter 6.

6 Performance of the sensor as eNose

SnO$_2$ nanowire is one of the essential building blocks of the KAMINA eNose system. Therefore, in the first section, the SnO$_2$ nanowire growth process optimization is discussed. In the next section, a performance comparison is presented between UV KAMINA and UV Chem-FET KAMINA, which indicates the different application appropriateness of these two systems. Then two applications of the eNose are discussed, i.e. early fire detector and explosive gas detector. Finally, the status of the research targets is addressed which has been defined at the beginning of this work.

6.1 SnO₂ nanowire growth process optimization

The SnO$_2$ nanowire growth mechanism has been covered in detail in section 3.1. In summary, at 900°C, SnO decomposes into SnO$_2$ and Sn (l, g) and carried to a condensing region of the substrate by the carrier gas (Ar), resulting in the precipitation of SnO$_2$ nanoparticles from Sn. Then the nanoparticles act as the nucleation sites for the growth of SnO$_2$ nanowires. Normally SnO$_2$ nanowire is tetragonally elongated along the c-axis. However, at lower temperatures on the accumulating substrate, it only grows toward the optimized direction, and hence nanowires form. A visual explanation is presented in figure 44.
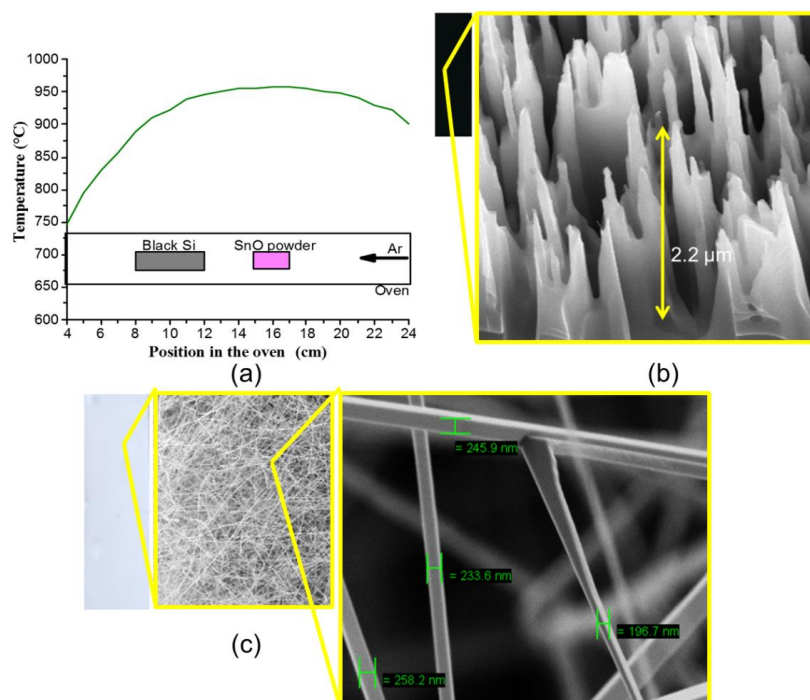
Figure 44: SnO$_2$ nanowire growth on black silicon substrate. (a) Temperature distribution within the oven. The typical position of the Black-Si substrate and SnO precursor is shown. (b) Black-Si substrate spikes, which are potential growing sites of SnO$_2$ nanowires (c) Typical density of nanowire grown on the Black-Si substrate. For this particular example, the nanowire diameter varies between 196 nm to 260 nm.

For the UV KAMINA sensor, the nanowires are dispersed on the sensor by following the Isopropanol solution drop-casting method using a syringe. As explained in section 4.3.1, the nanowires need to be placed into an ultrasound bath for 15 minutes to ensure long nanowires are broken and nicely diluted within the solution. To support this process, the nanowire diameter needs to be more than 100 nm. Below 100 nm, the nanowire crystal

structure tends to break down into fine pieces and does not contribute to the percolating connection between two electrodes which are spaced by 50µm. Additionally, the UV Chem-FET requires a high-density nanowire mat. Therefore, the growth process needs to be optimized to ensure a good portion of nanowires is having a diameter of above 100 nm, as well as the density of nanowires, which are sufficient to fulfill the need of UV Chem-FET sensor. The process optimization has been carried out experimentally and the optimization result will be discussed in the following sections.

6.1.1 Nanowire diameter variation regarding flow variation

Flow is defined as the change of volume per unit of time and as the unit, Standard Cubic Centimeter per Minute (SCCM) was used during the process. To investigate the impact of the carrier gas flow (Ar) variation, the following test protocol has been followed with 5 test repetitions at each carrier gas flow.

Table 3 Test protocol to investigate the flow variation impact on the SnO_2 nanowire

SnO Precursor Temperature	B-Si substrate temperature	Pressure	Ar Flow	O_2 Flow	O_2 hold time
°C	°C	mbar	SCCM	SCCM	min
920	890	600	30	0.5	60
920	890	600	40	0.5	60
920	890	600	50	0.5	60
920	890	600	100	0.5	60

The distribution of nanowire diameter at different carrier flow is shown in figure 45. At 30 SCCM, 50 SCCM, and 100 SCCM the diameter remains at around 150 nm. For all three occasions, nanowires diameter evenly distributed between a minimum of 100 nm and a maximum of 220 nm. However, at 40 SCCM, the median diameter remains at 100 nm, and the distribution of nanowire diameter is not symmetrical. Therefore, it can be concluded that the carrier gas flow doesn't have much impact on the nanowire diameter distribution.
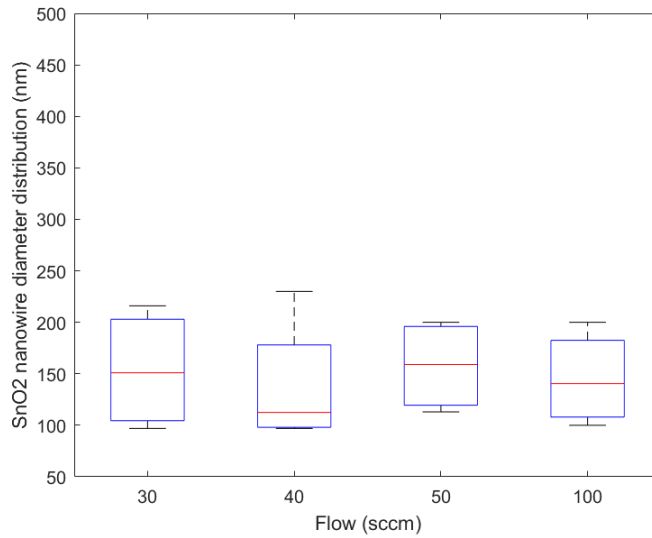
Figure 45: SnO₂ nanowire diameter distribution at different carrier flow. The carrier gas flow does not have much impact on the nanowire diameter distribution.

6.1.2   Nanowire diameter variation regarding pressure (p) variation

The test protocol presented in table 5 has been followed to investigate the pressure variation. SnO precursor temperature and B-Si substrate temperature were fixed at 920°C and 890°C respectively and additionally other relevant test parameters such as carrier gas Ar flow, O_2 flow, O_2 hold time were fixed as well.

Table 4 Test protocol to investigate the pressure variation impact on the SnO₂ nanowire

SnO Precursor Temperature	B-Si substrate temperature	Pressure	Ar Flow	O_2 Flow	O2 hold time
°C	°C	mbar	SCCM	SCCM	min
920	890	200	100	0.5	60
920	890	300	100	0.5	60
920	890	400	100	0.5	60
920	890	500	100	0.5	60
920	890	600	100	0.5	60

Nanowire diameter distributions at different pressures has been presented in figure 46.
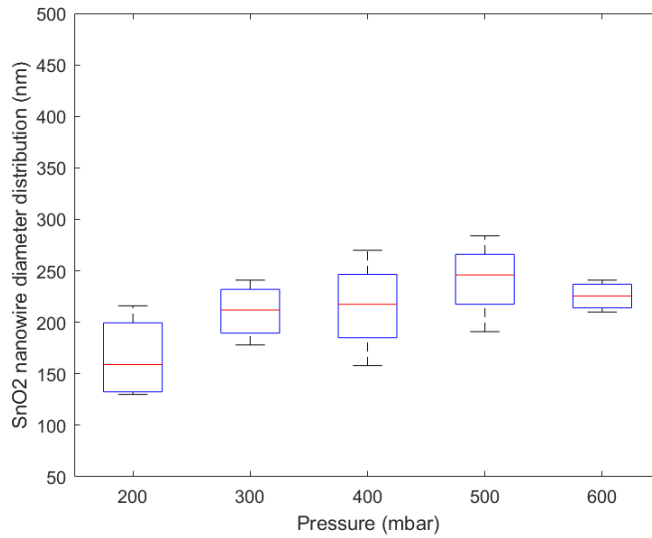
Figure 46: SnO₂ nanowire diameter distribution at different pressure. Between 200 mbar and 600 mbar pressure variation, the median of the nanowire diameter shifts from 160 nm to 225 nm.

It is evident that from 200 mbar to 600 mbar pressure variation, the median of the nanowire diameter increases from 160 nm to 225 nm respectively. However, the complete range (160nm – 225nm) of nanowire diameter is useful for the UV KAMINA.

6.1.3 Nanowire diameter variation regarding temperature (T) variation

As the chemical reaction happens within a narrow temperature range, therefore a wide range of temperature variation is not logical. The temperature has been varied between 877°C and 900°C. As shown in figure 47, the nanowire diameter varies between 100 nm and 400 nm within the specific temperature range. As the nanowires are mostly above 100nm, such temperature variation is not critical for both UV KAMINA and UV Chem-FET.
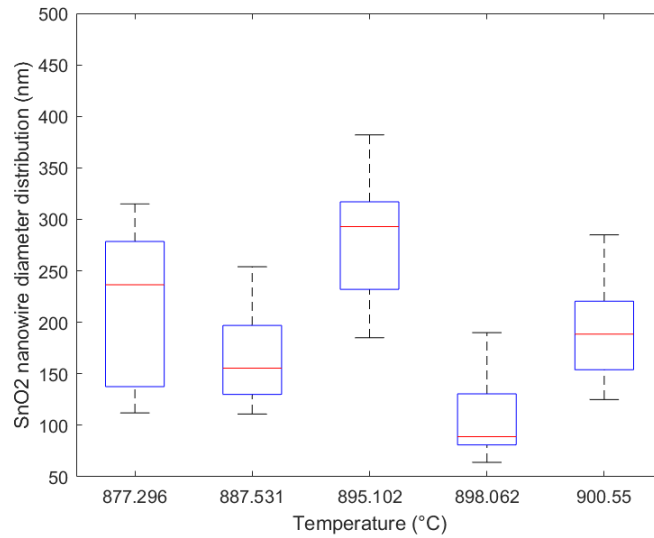
Figure 47: SnO$_2$ nanowire diameter distribution at different temperatures. Temperature variation has little to no impact on nanowire diameter distribution between 877 °C and 900 °C.

6.1.4   Nanowire density variation regarding temperature variation

The density of the nanowire growth on the black silicon surface varies widely. As shown in figure 48, the density is highest (30%) at around 895 °C regions, which is a favorable temperature for growth. At 877 °C and 904°C regions, the density drops down to 16% and 11% respectively.
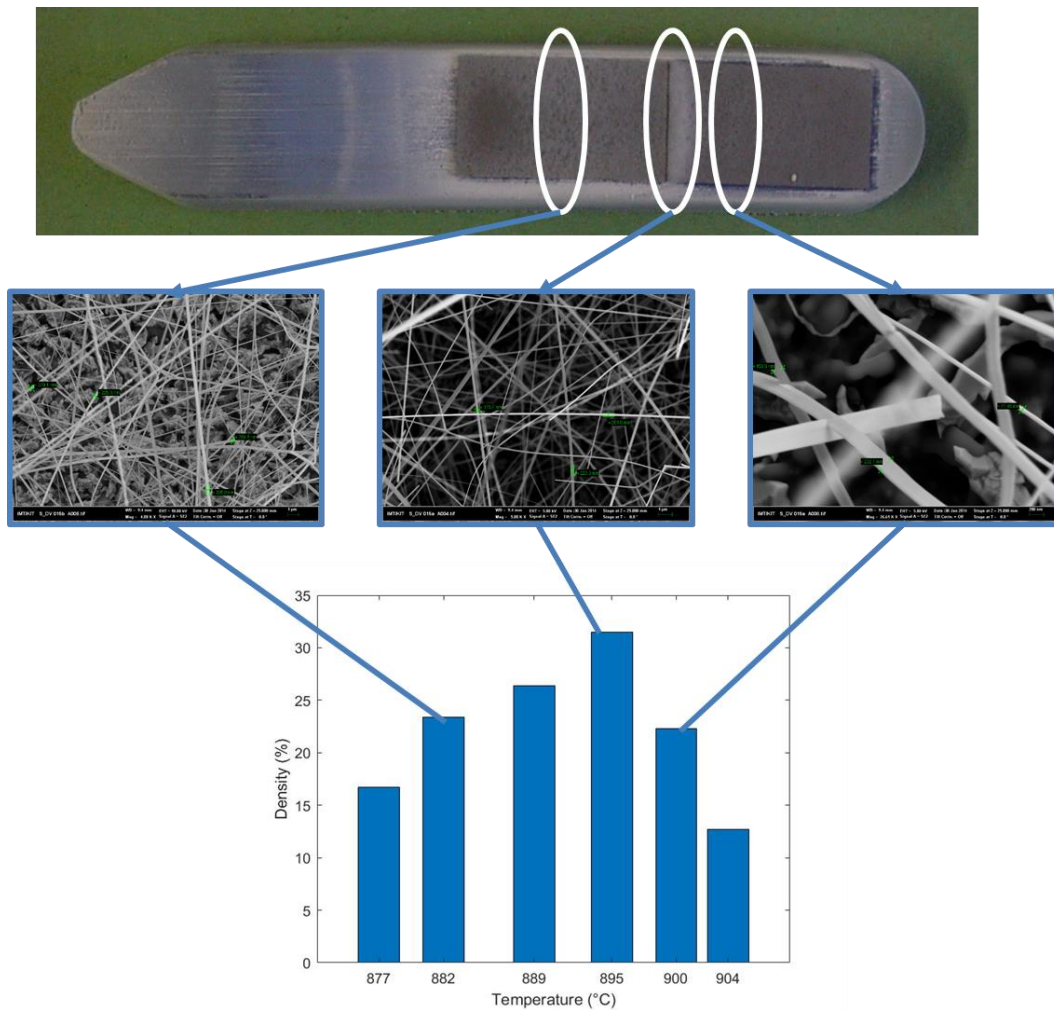
Figure 48: SnO₂ nanowire density distribution at different temperatures. Nanowire density varied between 18% and 32% for 877 °C and 895 °C respectively. At a high temperature of 904 °C, the nanowire density is relatively lesser than 15%.

As high density is one of the main objectives of the investigation, the Black silicon substrate is placed to cover 890°C to 900 °C temperature within the oven.

6.1.5 Crystal structure and material composition

After growing the nanowires, the crystal structure has been characterized by XRD. As shown in figure 48, the typical XRD pattern found after the growth process corresponds to the Tin-dioxide single crystal of the rutile category, which indicates the chemical homogeneity of the nanowires. The highest diffraction peaks have been found at (110), (101), (200), (202), and (400) crystal planes. From the XRD measurement, the crystal constants are as follows: a = 4.735 Å, c = 3.178 Å and V = 71.42 Å, which is comparable to the values found in other works of literature[110].
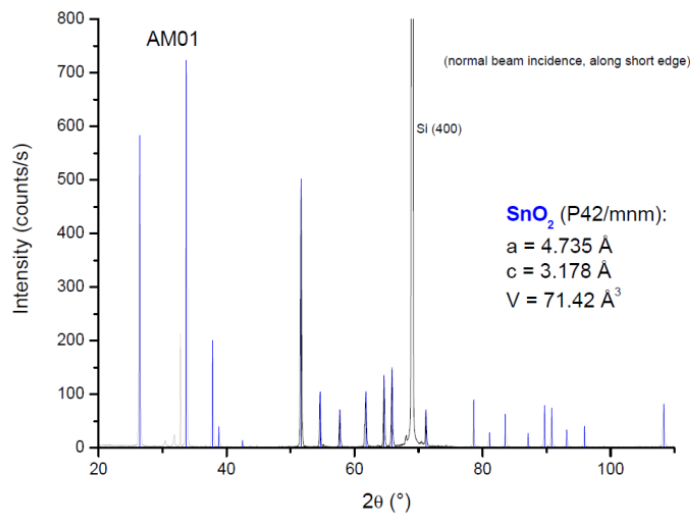
Figure 49: XRD pattern of SnO$_2$ nanowires placed over Si/SiO$_2$ substrate. The crystal constants have been found as follows: a = 4.735 Å, c = 3.178 Å, and V = 71.42 Å, which is very similar to the values found in literature[110].

6.1.6   Overall nanowire size distribution after optimization

After a typical growth process statistically, 42% of the nanowires are found to be within 201 nm – 300 nm as shown in figure 50. The remaining nanowires are distributed from 100nm – 600 nm. Among them, around 20% of the nanowires were within the 100-200 nm range. 21% of the nanowires were within the 301-400 nm range. 9% of nanowires were within the 401-500 nm range and the rest of nanowires are within the 501-600 nm range. As the nanowire size is substantially bigger, only 2% of nanowires from one batch are sufficient to prepare a single UV KAMINA sensor.
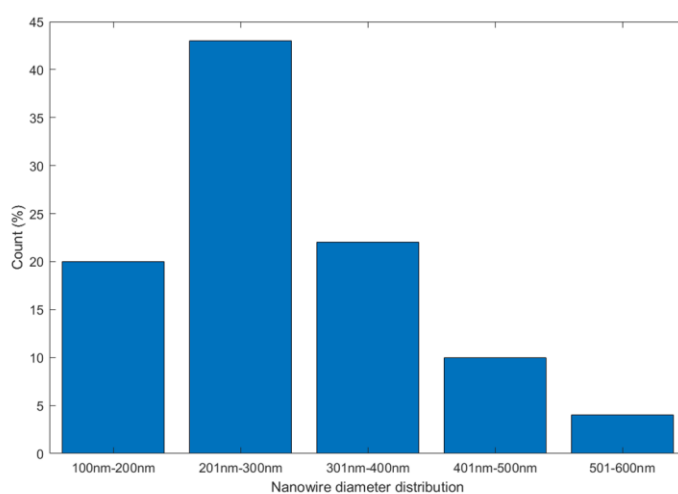
Figure 50: Nanowire size distribution after the growth process. 42% of the nanowires are within the 201 nm to 300 nm range.

6.2 Performance of UV KAMINA and UV Chem-FET

In this section sensor performance of UV KAMINA and UV Chem-FET KAMINA is discussed. Signal to noise ratio, response time, and selectivity have been considered as the top-three performance indicators. All the experiments in the section were done at ambient pressure, 50% relative humidity, and 25°C.

6.2.1 Signal to noise ratio

To quantify the signal-to-noise ratio both UV KAMINA and UV Chem-FET KAMINA sensors were exposed to 100 ppm Iso-propanol. Both sensor systems comprise an array of sub-sensors. Among all the sub-sensors, the most sensitive one has been chosen to quantify the Signal-to-noise ratio. The signal has been calculated using the following equation:

$$Signal\ (\%) = \frac{R_{air} - R_{gas}}{R_{air}}\ \%$$

As shown in figure 51(a), the UV Chem-FET sensor signal is 6.86% and in contrast, the UV KAMINA sensor signal is 16.67%. However, UV Chem-FET sensor signal has less noise ($\sigma=5.85\Omega$) compared to UV KAMINA sensor ($\sigma= 1.69 \times 10^4\ \Omega$). Therefore, the signal-to-noise ratio for UV Chem-FET and UV KAMINA is 1.17 and 9.87×10^{-4} respectively. The UV Chem-FET KAMINA sensor has a continuous conduction path via the substrate. On the other hand, the UV KAMINA sensor has a percolating conduction path via random positioning of nanowires, which may induce additional noise due to a different gas reaction on different paths after overcoming the Schottky barrier between the nanowires and the metal electrodes. Therefore, UV Chem-FET KAMINA has a higher signal-to-noise ratio for 100 ppm Iso-propanol.
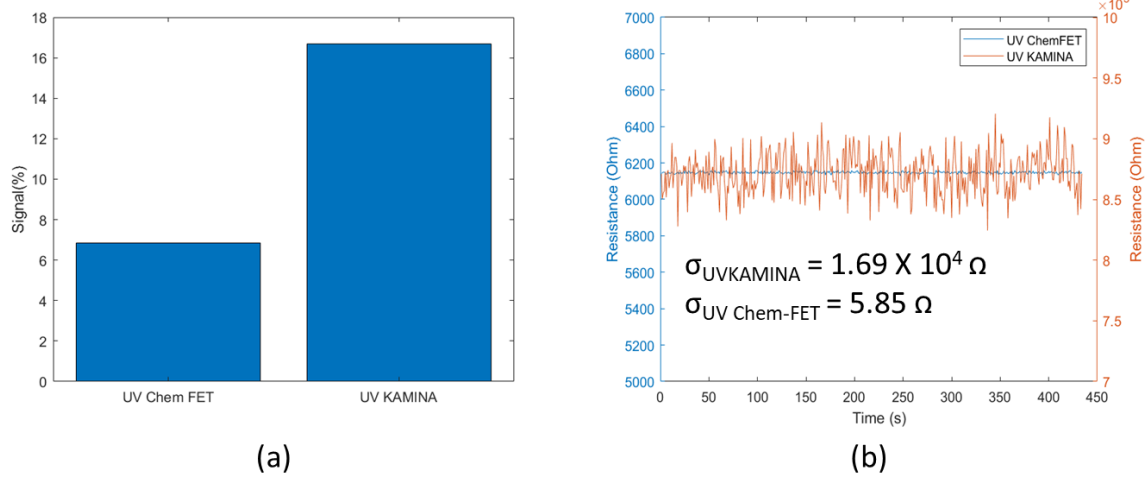
Figure 51: (a) The UV Chem-FET sensor signal is 6.86% and in contrast, the UV KA-MINA sensor signal is 16.67%. (a) UV Chem-FET sensor signal has less noise (σ=5.85Ω) compared to UV KAMINA sensor (σ= 1.69 × 10⁴ Ω).

6.2.2 Response time of UV KAMINA and UV Chem-FET

Response time is the amount of time required for a gas sensor to respond due to sudden gas exposure. As shown in figure 52, when both UV KAMINA and UV Chem-FET are exposed to 100 ppm Iso-propanol at the same time, UV Chem-FET reaches 90% of the saturation level much faster than UV KAMINA. A sub-sensor of a UV KAMINA might have multiple percolating conduction paths. Each conduction path possesses a different time constant resulting longer time to reach saturation. In contrast, the UV Chem-FET conduction path is via the Si substrate and offers a single time constant. Therefore, UV Chem-FET is faster than UV KAMINA. However, a shorter response time is not a problem for UV KAMINA. The UV KAMINA can be trained with a 'smell exposure' in the transition phase. Therefore, for a fire alarm type application, UV KAMINA is perfectly suitable when trained with the burning smell in the transition phase. Further details of the fire alarm application are discussed in section 6.3.
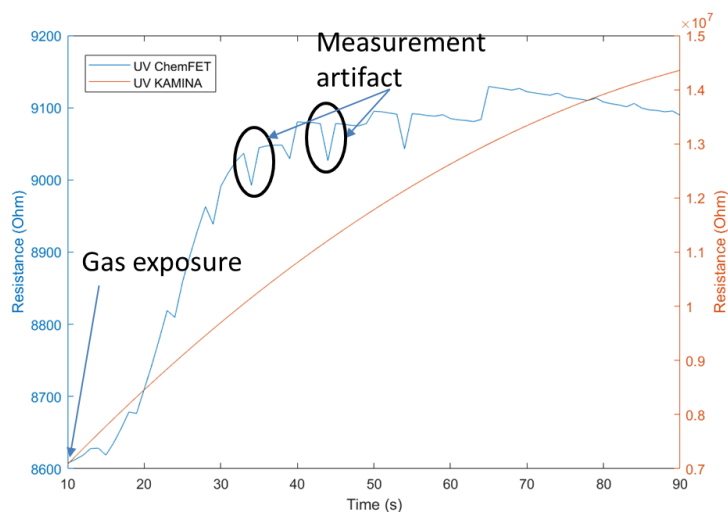
Figure 52: UV Chem-FET has a faster response time than UV KAMINA when exposed to 100 ppm Iso-propanol. During this experiment, The UV Chem-FET showed some measurement artifacts due to readout electronics' limitations.

6.2.3   eNose Selectivity based on the classification algorithm

The ability of a sensor to respond uniquely under exposure to different smells and classify them is addressed with the term selectivity. As the sensing material, the pristine SnO_2 nanowires are not very selective for different gases. However, in combination with a classification algorithm like LDA, a good selectivity can be achieved. Following the LDA classification methodology, selectivity can be quantified in terms of the 'Completeness of explanation' of the LDA model. To quantify the selectivity of UV KAMINA and UV Chem-FET KAMINA, both of them were exposed to 100 ppm Iso-propanol, 100 CO, and 100 ppm Benzene. The sum of the real parts of eigenvalues, found by LDA is expressed as 'Completeness of explanation'. As shown in figure 53, for the UV KAMINA the 'Completeness of explanation' of the LDA is 89%. In contrast, the UV Chem-FET offers a 'Completeness of explanation' of 60%. This indicates that UV KAMINA finds a better smell fingerprint compared to UV Chem-FET. There can be two reasons behind the better selectivity of UV KAMINA.

I.   UV KAMINA's random percolating conduction path reacts differently with a unique time constant for different gas exposure. This might help the system to extract better gas dynamic information.

II. UV KAMINA consists of 16 sub-sensors. In contrast, UV Chem-FET has only 7 sub-sensors. More sub-sensors of the UV KAMINA might facilitate during the smell fingerprint classification.

Therefore, further investigation is necessary on this topic to conclude.
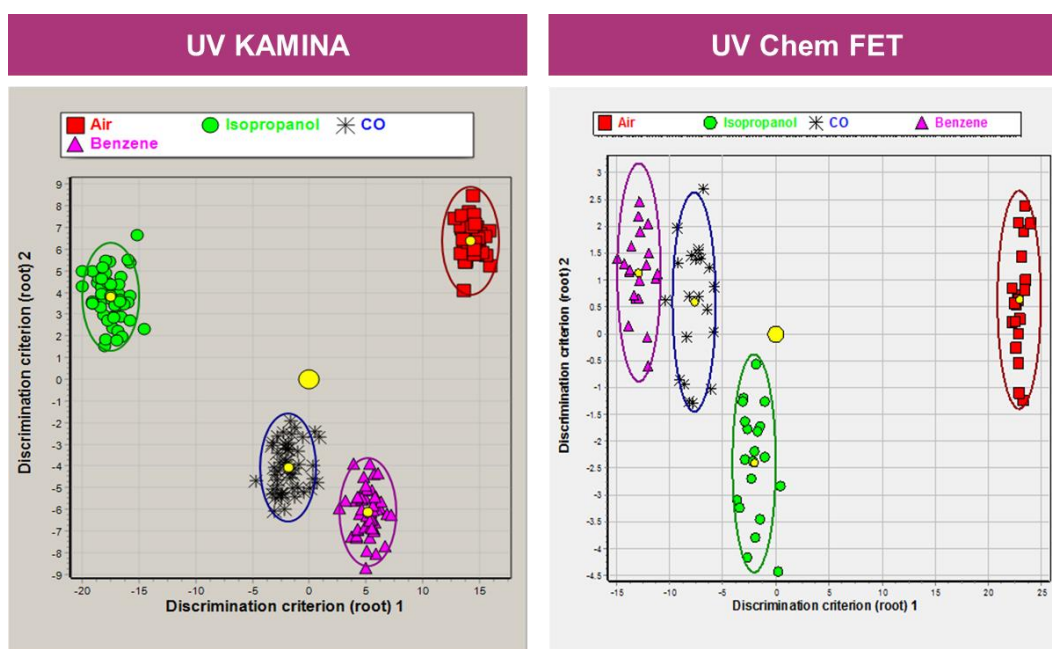
Figure 53: Selectivity based on LDA classification algorithm for UV KAMINA and UV Chem-FET. UV KAMINA offers better selectivity than UV Chem-FET. The sensors were exposed to 100 ppm CO, 100 ppm Iso-propanol and, 100 ppm Benzene.

6.2.4 Cross sensitivity to relative humidity

Both UV KAMINA and UV Chem-FET KAMINA share the same sensing material as SnO_2 nanowire. SnO_2 is responsive to humidity. The humidity-induced signal variation may lead to misclassification for the KAMINA system, which has been investigated and the result is presented in figure 54. The experiment has been conducted on a UV KA-MINA at nine steps during three separate experiments according to the test protocol listed in table 5. In figure 54, the 3 data files are stitched during data processing, hence shows the sudden jump.

Table 5 Test protocol to investigate relative humidity dependency for a KAMINA system

Target gas	Concentration (ppm)	Relative humidity (%)	Time (s)
Synthetic air	N/A	0	280
Synthetic air	N/A	50	250
Synthetic air	N/A	70	250
CO	150	0	280
CO	150	50	250
CO	150	70	250
Iso-propanol	150	0	280
Iso-propanol	150	50	250
Iso-propanol	150	70	250
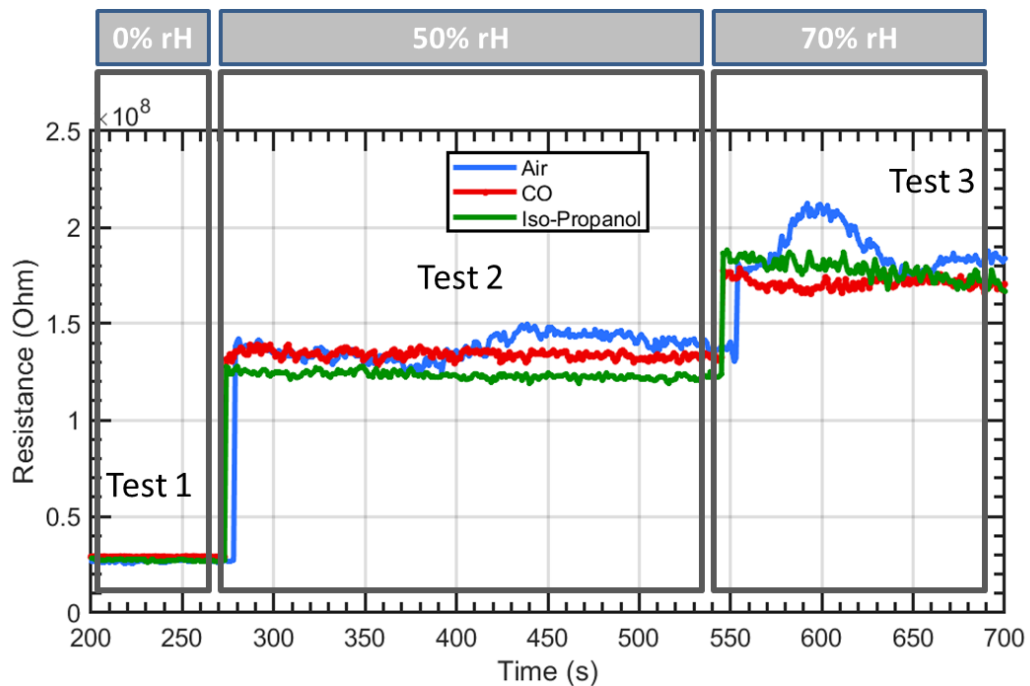
Figure 54: Variation of median resistance of UV KAMINA at different relative humidity levels at fixed gas concentration. The sudden jumps in the lines are artifacts coming from data handling while stitching multiple data files and therefore are not representing the response time of the sensor.

Three types of LDA model has been made to understand the impact of relative humidity change on the KAMINA system's LDA model.

LDA model-1:

   I. Class Air = Air at 0% relative humidity + Air at 50% relative humidity + Air at 70% relative humidity
  II. Class Iso-propanol = Iso-propanol at 0% relative humidity + Iso-propanol at 50% relative humidity + Iso-propanol at 70% relative humidity
 III. Class CO = CO at 0% relative humidity + CO at 50% relative humidity + CO at 70% relative humidity

LDA model-2:

   I. Class Air = Air at 50% relative humidity + Air at 70% relative humidity
  II. Class Iso-propanol = Iso-propanol at 50% relative humidity + Iso-propanol at 70% relative humidity
 III. Class CO = CO at 50% relative humidity + CO at 70% relative humidity

LDA model-3: Consider relative humidity as one of the LDA input parameters

I. Class Air = Air at 0% relative humidity + Air at 50% relative humidity + Air at 70% relative humidity

II. Class Iso-propanol = Iso-propanol at 0% relative humidity + Iso-propanol at 50% relative humidity + Iso-propanol at 70% relative humidity

III. Class CO = CO at 0% relative humidity + CO at 50% relative humidity + CO at 70% relative humidity

As shown in figure 55(a), the LDA model-1 poorly classifies all three classes, when three relative humidity data are used as the model input. This indicates that in-field applications, such LDA model might misclassify if relative humidity varies widely. However, as shown in figure 55(b), the LDA model-2 classifies all three gases in a better way. This indicates that in-field application if an LDA model is used after trained with 50% and 70% relative humidity, the system might classify the target smell considering the relative humidity varies between 50% and 70% relative humidity. However, an even better LDA model can be built (figure 55(c)) if along with the resistances of different sub-sensors, relative humidity information is also used as an LDA training input. Therefore, if the KAMINA system is intended to be used for a wide range of relative humidity variations, it is recommended to consider a relative humidity sensor in the final solution to achieve better selectivity.
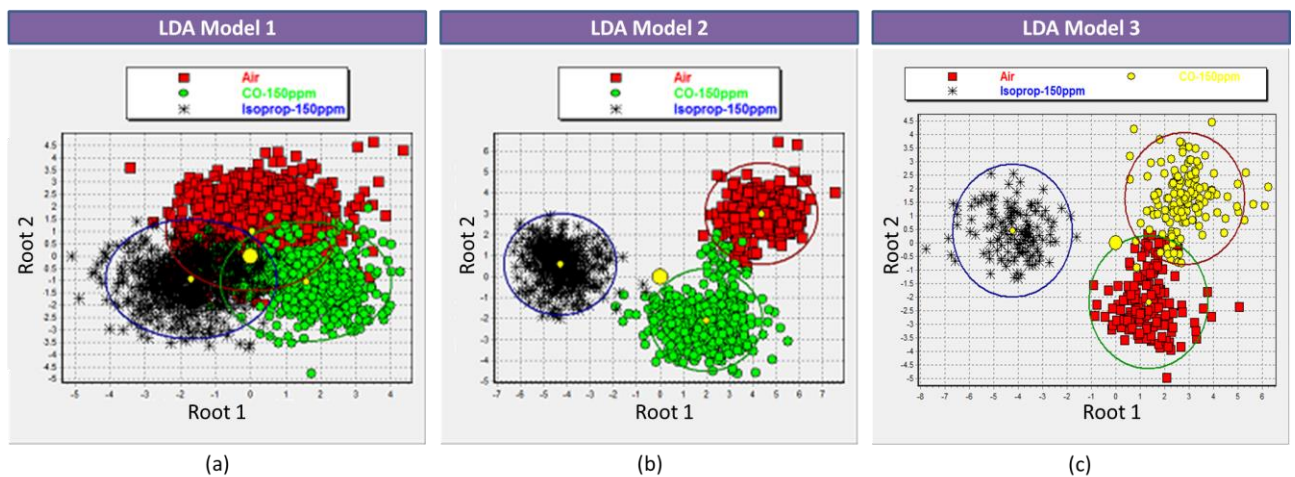
Figure 55: Three LDA models with different input parameters. By considering relative humidity as an input parameter of the LDA classification model, the sensor system can separate all three classes for three relative humidity levels.

6.2.5 Performance summary of UV KAMINA and UV Chem-FET

Both sensors are having strong and weak points, which has been summarized in table 6. UV Chem-FET offers a better signal-to-noise ratio and faster response time. However, UV KAMINA offers better classification at this stage. Therefore, for an eNose application, the UV KAMINA is better suited.

Table 6 Performance summary of UV KAMINA and UV Chem-FET

Key parameters	UV Chem-FET	UV KAMINA	Note/ Condition
Signal to noise ratio	1.17	9.87×10^{-4}	Iso-propanol 0 to 100 ppm
Response time	Faster	-	Iso-propanol 0 to 100 ppm
Selectivity	89%	60%	Completeness of explanation

6.3 Potential Applications

In terms of development, UV Chem-FET is still in a prototype phase and there are still limitations in terms of laboratory preparation to explore other applications. However, as a proof of concept, functionality as a fire alarm has already been showcased in chapter 5. Therefore, in this section, only the potential application of UV-KAMINA has been covered. The work has been published partially[11].

6.3.1 Fire alarm

A fire detector senses the early signs of a fire hazard. Normally, the detection is done in a form of heat, flame, smoke, or CO detection[111]. Several technologies are seen in the market covering consumer and industrial applications. Optical type fire alarm works based on the principle of triggering a photodiode when smoke goes inside the housing of the alarm. An ionization-based detector requires a radioactive component to ionize the air. When smoke breaks into the ionization potential, the disturbance is picked by the detector circuitry. Heat-based detectors trigger the alarm based on heat sensing. Very often, such a sensor needs multiple sensing components. For a large open area, normally video and the image-processing are used[112].

In the product landscape, eNose based fire alarm is not present at the moment. All the mentioned fire alarm techniques only work when there are smokes at an advanced level of fire. The main pain points of existing solutions for industrial and safety applications can be shortlisted as follows:

I. Extensive maintenance requirements. Bi-yearly for the majority of the products.
II. The limited scope of measurements and amount of gasses. Most of them detect only CO.

III. Complex data analysis requirements for a combination of multiple sensor solutions
IV. They are not capable to perform early detection

Exactly at this point, the value proposition of the KAMINA eNose highlights as eNose, which can offer two unique features:

I. Early detection based on smell change in the application area, even before the smoke starts to come out.
II. Gives an indication of burning material based on machine learning-based classification algorithm

6.3.1.1 System requirement of the fire alarm covered in SMOKESENSE project

Two key system requirements have been covered in two milestones:

- Milestone 1: Optimization of the KAMINA with optimized power consumption. Power consumption of the final product should be less than 5 mW
- Milestone 2: Prototype of the system for the fire risks monitoring ready

6.3.1.2 Testing in lab condition

The experimental setup used for this work has been discussed in Chapter 3, section 3.4. The flammability of a substance depends on its amount, rate of heat flow through the material, and time. Hence, it would be unrealistic to find the absolute sensitivity of a burning smell. However, to find the detection limit of the system, a heated common material's smell identification was necessary, and to determine the detection limit of the sensor as a fire alarm, experimental protocol as mentioned in table 6 has been used.

Table 7 Experimental protocol to determine the detection limit of the sensor as a fire alarm at 25°C, 50% relative humidity, and ambient atmospheric pressure

Heater temperature °C	Time (min)	MFC6 (sccm)	MFC7 (sccm)
0	30	500	500
100	30	500	500
150	30	500	500
200	30	500	500
Total time	120		

A piece of 0.15 g printed circuit board (PCB) has been heated up to 200 °C from room temperature to obtain the smell at different temperatures. In figure 58 it is shown, that the 3σ line (Signal = 0.12) meets the fit at 108 °C. So, the quantitive detection limit of the burning smell of 0.15 g PCB is 108 °C, which is far below the experimented smoke breaking temperature of around 300 °C.
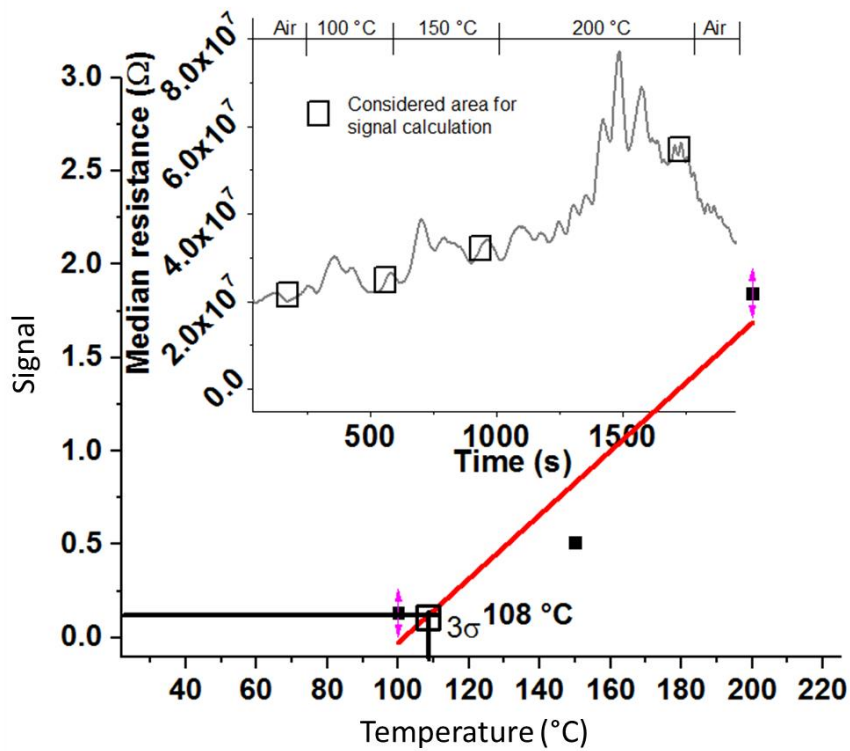
Figure 56: Signal strength characterization by heating a 0.15 g PCB at 100 °C, 150 °C, and 200 °C. The smoke breaking temperature of a similar PCB piece is around 300 °C. As the temperature increases, the signal increases exponentially.

The burning smell selectivity has also been characterized by the 'Completeness of explanation' of the LDA model consisting of three burning smells and reference air. The experimental setup is shown in section 3.4. During the test synthetic air with 50%, relative humidity carried the burning smell of the target material to the sensor vicinity. Cotton (0.12 g), beech (0.5 g), and PCB (0.15 g) were heated at 200 °C within the burning chamber. Parallel airflow has been used to clean the chamber before every burning phase. To help the reader recall the details of section 3.4 an illustration is provided in the following figure 57.
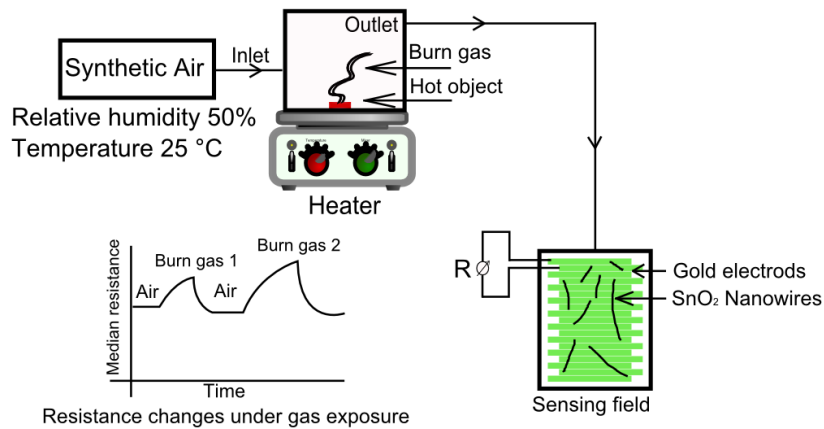
Figure 57: Experimental setup for a burn test. Initially, the heater was heated to 200 °C. Then different objects were placed on the hot plate in between two purging air periods

Cotton, beech, and PCB were on the hotplate for 4 minutes, 4 minutes, and 10 minutes respectively. For the LDA shown in figure 58, 60 data point form the middle has been considered from each event. For class 'Air', 15 data points from the last part of every air event were considered for the LDA. As shown in figure 60, the electronic nose system successfully discriminated all the substances at pre-burning temperature having a 'Completeness of explanation' of 88%.
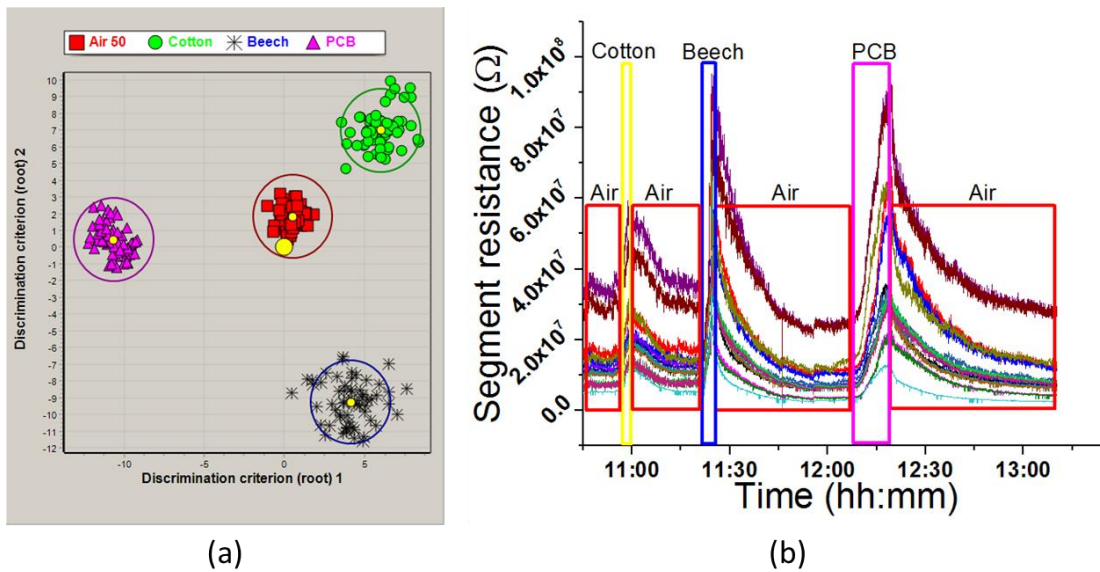
Figure 58: (a) Classification of different types of heated substances at 200 °C. The response of 16 segments is shown by unique colors. As the four classes cover both dimensions, the separation is acceptable. (b) LDA Plot: An LDA model was created with four different classes having Air, Cotton, Beech, and PCB

6.3.1.3 Field test at DBI

The goal of this experiment was to check the functionality of such a sensor in a real-life scenario. The test was performed in the test facilities at DBI, in a big container that mimics a normal room for an elderly person as covered in section 3.4.1. As a heating source, an electric stove has been used which was placed 2m above the ground. The sensor set up was attached on a stand with a possibility of adjusting the height. Being a widely used home material, beech, cotton, and PCB has been burned using the stove with maximum power at approximately 400 °C. A detailed description of this setup has been covered in Chapter 3. As shown in figure 59, the LDA model has successfully separated all the relevant smells. Apart from beech, cotton, and PCB, a fourth class is taken as the smell of the test chamber. The marked 'Transition region' indicates intermediate sensing events, when the smell is changing from one class to the next. The selectivity of the sensor is acceptable as the 'Completeness of explanation' of the model is 72%, which is worse than the 'Completeness of explanation' found in the lab (88%), which indicates that further test calibration and verification optimization are necessary before, the KAMINA system can be used in the real-world condition.
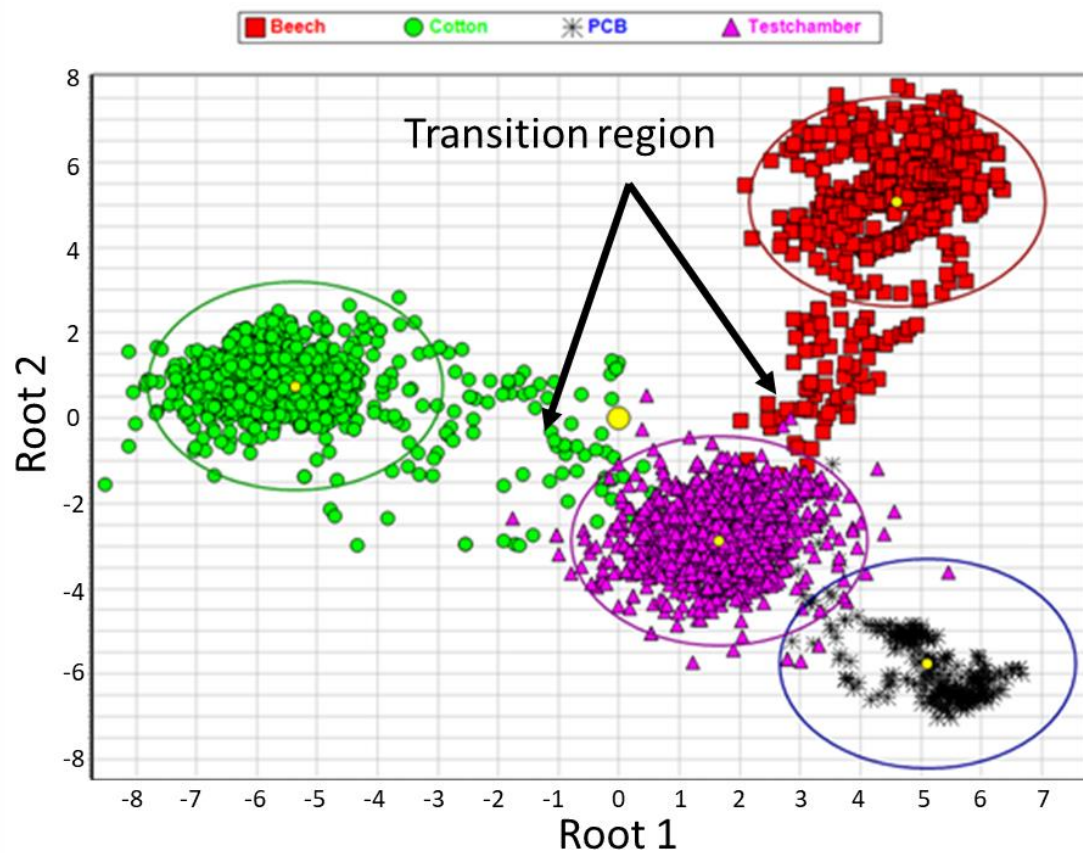
Figure 59: The laboratory-trained LDA classification model efficiently classifies the burning smell of Beech, Cotton, and PCB in a real-world condition after burning the material at 400 °C using a stove.

However, at this stage, it is not possible to conclude the alarm threshold value, as the sensor is fundamentally different from a traditional fire detector and hence requires an improved benchmarking system in contrast to the traditional one.

6.3.2 Explosive detector

Explosive detection application has been investigated in collaboration with Dr. Nico Bolse from LTI. The purpose was to explore the scalability in terms of applications using the UV KAMINA concept. The work has been presented partially at the IEEE Sensor conference 2016[12].

6.3.2.1 The goal of the study

The use of explosives in civilian attacks is a positive trend. Law enforcement agencies are facing problems with detecting hidden explosives in luggage, mail, vehicles, etc. The

current state-of-the-art detection method for explosives is sniffer dog[113–116]. But, expensive training and deteriorated life expectancy of trained canine animal leaves an area of research to develop an alternative approach. But, reliable detection of explosives is still a tireless problem due to the required high sensitivity and good selectivity to detect traces of explosives in a dynamic ambient environment[117–120]. For example, Nitrobenzene has a vapor pressure of 272 ppb at 21 °C temperature. Therefore, the detection system has to be highly sensitive at room temperature to trace explosive smell at ppb level.

6.3.2.2 Explosive detection result

UV KAMINA successfully classified the explosive materials at 30%, 50%, and 70% relative humidity as shown in figure 62. NB, AN, and DMNB are positioned closely, which indicates that the eNose will find it difficult to classify each one of them individually if present in a real-world scenario at the same time. Additionally, at different humidity LDA classified the pollutant differently, indicates that the sensor will need the relative humidity information for better classification.
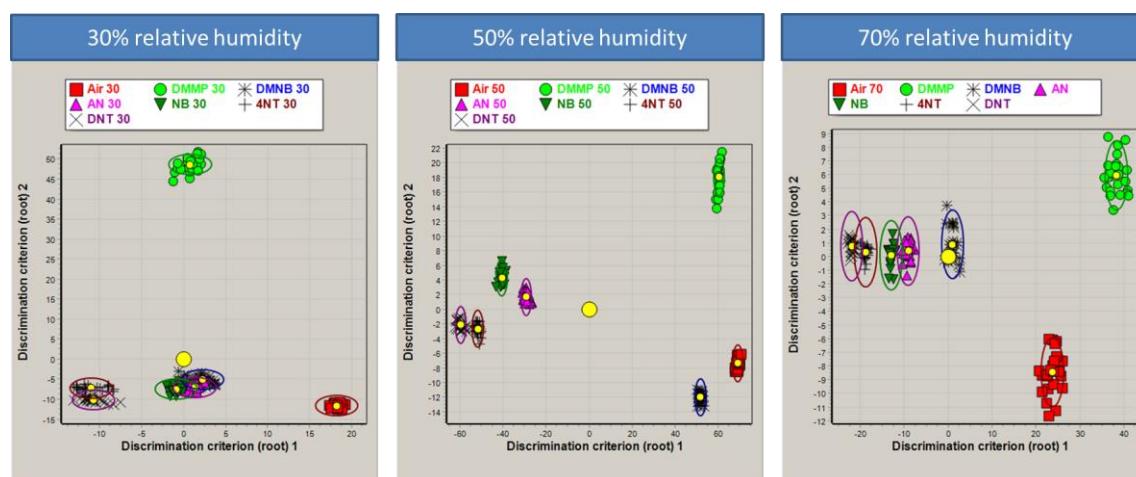
Figure 60: Classification of different types of explosive material in controlled laboratory conditions at three different relative humidity levels, i.e 30%, 50%, and 70%.

Explosives can be distinguished nicely at 50% relative humidity. However, moderately by one dimension at 30% and 70% relative humidity. Separation from the normal air is always quite good. Further investigation on the separation from disturbing materials has not been investigated. For that, an explosive reference sensor is necessary. However, organizing a reference detector for every single compound was out of the scope of the study. The goal was to investigate the potential application as an alternative cost-effective, energy-efficient mobile monitoring system. To realize the concept as a product, further investigation is necessary with a more stable calibration setup.

6.4   Discussions on the 'Research Targets'

Research Target 1: *Develop a SnO_2 nanowire-based eNose that can be used as a smart fire detector. The eNose should be able to detect potential fire hazards in the early stage and simultaneously predict the source of the potential fire.*

In section 6.3.1, it has been showcased that SnO_2 nanowire-based printed eNose can be used as an early fire detector based on smell changes in the room. Initially, it has been proven in a controlled lab environment. A close-to-real-case scenario test setup was developed at DBI, Denmark where the sensor worked reasonably.

Research Target 2: *The developed platform within the scope of the SMOKESENSE project should be able to reuse for other applications.*

In section 6.3.2, it has been showcased that the UV KAMINA sensor can be used effectively as an explosive gas vapor detector. This indicates, that the KAMINA system has a very strong potential in the eNose field to cover a wider range of applications.

Research Target 3: *Investigate the root cause of the limitations of the state-of-the-art SnO_2 material for gas sensing application and demonstrate a potential solution to minimize as many limitations as possible within the scope of the thesis work.*

In chapters 4 and 6, it has been showcased, that the UV KAMINA can offer better power consumption, better stability while minimizes system complexity. Additionally, UV Chem-FET KAMINA presented in chapters 5 and 6 may offer better performance in key areas like response time and signal-to-noise ratio.

7   Executive Summary and Outlook

Thanks to European Union Horizon 2020 SMOKESENSE project, this work had one primary goal, which is to revolutionize fire safety applications by introducing eNose, which not only facilitates early fire detection based on smell change but also, inform the user which material is going to burn in following minutes. However, there were several technical challenges for the sensor system to fulfill the key application requirements as a fire alarm, which have been targeted within the scope of the thesis work.

There were several must-have application requirements, which are:

1. Low power consumption compared to the heater based KAMINA
2. Fast response time to smell change before the fire breaks out
3. Reliable sensor stability and selectivity for the burning smell

To meet the must-have application requirements several technological limitations had to be dealt with.

Power consumption: Traditionally, the KAMINA system used to work based on a heater, which needs to operate between 300 °C and 200 °C in continuous mode. Such heaters not only consume a lot of power but also facilitates Siloxane contamination which makes the sensor less sensitive over time during operation. Instead of using a heater, UV illumination has been used effectively, which not only reduced the power consumption (UV KAMINA consumes 50 mW, UV Chem FET consumes 4.2W to 9W) but also improves the overall stability of the sensor for the complete lifetime of the final product. Furthermore, in-process sensitivity variation due to the use of a fast variation of wavelengths or illumination power can be implemented to increase LDA separation quality as the next step.

Fast response time: Compared to a traditional fire alarm system, UV KAMINA is fast, as it doesn't have to wait until a smoke breaks out. It could potentially determine as soon as the surrounding smell changes to a burning smell fingerprint signal. Furthermore, UV Chem-FET showed an even faster response time makes it an interesting candidate to explore in the future.

Apart from these points, there are some more notable highlights:

I. Successfully demonstrated printed KAMINA sensor, which opens up enormous potential, as the printing technology is becoming mature every day.
II. SnO_2 nanowire production has been optimized in a systematic way, which provides a clear direction for mass production.

III. UV KAMINA has been demonstrated as a platform, rather than a one-time solution, which also indicates potential coverage of a wider range of applications.

However, as an outlook, some critical areas also need to be addressed to ensure a successful journey of the KAMINA system from the research arena to the market.

a. Part to part variation:

Even though conceptually UV Chem-FET KAMINA is better positioned than UV KAMINA with regards to parts to parts variation, the development of UV KAMINA is more advanced. UV KAMINA has been developed based on a random distribution of SnO_2 nanowires on interdigitated electrodes, which is the fundamental reason behind the strong part to part variation. Even though the prototype has performed very well under defined circumstances, it is very difficult to deal with for a real product. Methodologies like, electrophoresis and printing technique need to be evaluated for a potential solution to this problem.

b. eNose calibration, characterization, testing, and validation methodology:

For a gas sensor, ideally, the sensor response is characterized based on gas concentration delivered in a secured gas bottle by companies like Linde or BASI. However, a gas bottle with a specific smell concentration is not offered at the moment due to technical limitations. Sometimes, it is possible to prepare a combination of gases such as BTEX or VOC, however, it is very much limited to certain applications. To get a reliable and reproducible characteristic of an eNose, it is very important to minimize this gap. Alternatively, at least a correlated gas response to an eNose application needs to be found, which eventually may help to minimize the gap using an advanced algorithm. For a reliable calibration, characterization, testing, and validation methodology minimizing such gap are essential.

c. Further minimization of the influence of ambient condition:

A SnO_2 sensor is fundamentally influenced by humidity and ambient temperature variation. UV KAMINA can effectively classify within 30% relative humidity and 70% relative humidity conditions at 25 °C, which only covers a small window of a typical operating condition of a wide range of applications. One way to solve this issue can be choosing a hydrophobic material like Graphene as a sensing element. Another way can be using an additional relative humidity and temperature sensor as a feature parameter for a compensation algorithm.

d. Influence of a package:

For the final product, the sensor needs to be delivered within a package. The influence of a package on the sensor response is not trivial. From glue to necessary opening of the diffusion hole for the package need to be evaluated. Additionally, a secured way needs to

find out so that the sensor characteristics remain intact after different stress tests like vibration test, drop test, etc.

e. eNose standardization:

Finally, it is time to push for an eNose standardization activity with participants from different eNose developers and end-users. At this point, there is no agreement between different stakeholders in the eNose market, which may easily lead to misinterpretation of an eNose behavior and potentially hinder the growth of this unique solution.

In the end, there are several notable achievements in this work, however further work is necessary to bring the KAMINA technology to the market.

Bibliography

1. Geddes, L. A. Respiration. in *Medical Devices and Systems* (2006). doi:10.5749/j.ctv9b2tqv.33.

2. Air Quality - National Summary | National Air Quality: Status and Trends of Key Air Pollutants | US EPA. https://www.epa.gov/air-trends/air-quality-national-summary.

3. WHO | Ambient and household air pollution and health. *WHO* (2019).

4. Air Pollution Deaths Cost Global Economy US$225 Billion. https://www.worldbank.org/en/news/press-release/2016/09/08/air-pollution-deaths-cost-global-economy-225-billion.

5. Allen, J. G. *et al.* Associations of cognitive function scores with carbon dioxide, ventilation, and volatile organic compound exposures in office workers: A controlled exposure study of green and conventional office environments. *Environ. Health Perspect.* **124**, 805–812 (2016).

6. The connection between air quality and the UN Sustainable Development Goals - Breeze Technologies. https://www.breeze-technologies.de/blog/connection-between-air-quality-and-un-sustainable-development-goals/.

7. Développement, Y. Gas & Particle Sensors Report 2018. (2018).

8. Ehrmann, S., Jüngst, J., Goschnick, J. & Everhard, D. Application of a gas sensor microarray to human breath analysis. *Sensors Actuators, B Chem.* **65**, 247–249 (2000).

9. Chuang, M. Y. *et al.* Room-temperature-operated organic-based acetone gas sensor for breath analysis. *Sensors Actuators, B Chem.* **260**, 593–600 (2018).

10. Schweizer-Berberich, P. M., Vaihinger, S. & Göpel, W. Characterisation of food freshness with sensor arrays. *Sensors Actuators B. Chem.* **18**, 282–290 (1994).

11. Adib, M., Eckstein, R., Hernandez-Sosa, G., Sommer, M. & Lemmer, U. SnO2 nanowire-based aerosol jet printed electronic nose as a fire detector. *IEEE Sens. J.* **18**, 494–500 (2018).

12. Adib, M. & Sommer, M. UV excited SnO2 nanowire based printed e-Nose: Potential application as burning smell detector and explosive detector. in *Proceedings of IEEE Sensors* (Institute of Electrical and Electronics Engineers Inc., 2017). doi:10.1109/ICSENS.2016.7808805.

13. Wang, C., Yin, L., Zhang, L., Xiang, D. & Gao, R. Metal oxide gas sensors: Sensitivity and influencing factors. *Sensors* vol. 10 2088–2106 (2010).

14. Bushdid, C., Magnasco, M. O., Vosshall, L. B. & Keller, A. Humans can discriminate more than 1 trillion olfactory stimuli. *Science.* **343**, 1370–1372 (2014).

15. Gardner, J. W. & Vincent, T. A. Electronic noses for well-being: Breath analysis and energy expenditure. *Sensors (Switzerland)* Vol. 16 (7) 947-972, (2016)

16. Albert, K. J. *et al.* Cross-reactive chemical sensor arrays. *Chem. Rev.* **100**, 2595–2626 (2000).

17. Röck, F., Barsan, N. & Weimar, U. Electronic nose: Current status and future trends. Chemical Reviews vol. 108 705–725 (2008).

18. Hierlemann, A. & Gutierrez-Osuna, R. Higher-order chemical sensing. *Chemical Reviews* vol. 108 563–613 (2008).

19. Persaud, K. & Dodd, G. Analysis of discrimination mechanisms in the mammalian olfactory system using a model nose. *Nature* **299**, 352–355 (1982).

20. Lundström, I. *et al.* Artificial 'olfactory' images from a chemical sensor using a light-pulse technique. *Nature* **352**, 47–50 (1991).

21. Haddad, R. *et al.* A metric for odorant comparison. *Nat. Methods* **5**, 425–429 (2008).

22. Hagleitner, C. *et al.* Smart single-chip gas sensor microsystem. *Nature* **414**, 293–296 (2001).

23. Rakow, N. A. & Suslick, K. S. A colorimetric sensor array for odour visualization. *Nature* **406**, 710–713 (2000).

24. FISHER, R. A. THE USE OF MULTIPLE MEASUREMENTS IN TAXONOMIC PROBLEMS. *Ann. Eugen.* **7**, 179–188 (1936).

25. Sysoev, V., Kiselev, I., Frietsch, M. & Goschnick, J. Temperature Gradient Effect on Gas Discrimination Power of a Metal-Oxide Thin-Film Sensor Microarray. *Sensors* **4**, 37–46 (2004).

26. Chatterjee, C. & Roychowdhury, V. P. On self-organizing algorithms and networks for class-separability features. *IEEE Transactions on Neural Networks* vol. 8 663–678 (1997).

27. Ahdesmäki, M. & Strimmer, K. Feature selection in omics prediction problems using cat scores and false nondiscovery rate control. *Ann. Appl. Stat.* **6**, 503–519 (2012).

28. Yu, H. & Yang, J. A direct LDA algorithm for high-dimensional data — with application to face recognition. *Pattern Recognit.* **34**, 2067–2070 (2001).

29. Aliyari Ghassabeh, Y., Rudzicz, F. & Moghaddam, H. A. Fast incremental LDA feature extraction. *Pattern Recognit.* **48**, 1999–2012 (2015).

30. Martinez, A. M. & Kak, A. C. PCA versus LDA. *IEEE Trans. Pattern Anal. Mach. Intell.* **23**, 228–233 (2001).

31. Momma, K. & Izumi, F. VESTA 3 for three-dimensional visualization of crystal, volumetric and morphology data. *J. Appl. Crystallogr.* **44**, 1272–1276 (2011).

32. Arlinghaus, F. J. Energy bands in stannic oxide (SnO2). *J. Phys. Chem. Solids* **35**, 931–935 (1974).

33. Robertson, J. & Falabretti, B. Electronic Structure of Transparent Conducting Oxides. in *Handbook of Transparent Conductors* 27–50 (Springer US, 2011). doi:10.1007/978-1-4419-1638-9_2.

34. Jarzebski, Z. M. & Marton, J. P. Physical Properties of SnO2 Materials: I . Preparation and Defect Structure. *J. Electrochem. Soc.* **123**, 199C-205C (1976).

35. Agekyan, V. T. Spectroscopic properties of semiconductor crystals with direct forbidden energy gap. *Phys. Status Solidi* **43**, 11–42 (1977).

36. Egdell, R. G., Flavell, W. R. & Tavener, P. Antimony-doped tin(IV) oxide: Surface composition and electronic structure. *J. Solid State Chem.* **51**, 345–354 (1984).

37. Serin, T. *et al.* Electrical, structural and optical properties of SnO2 thin films prepared by spray pyrolysis. *J. Non. Cryst. Solids* **352**, 209–215 (2006).

38. Manifacier, J. C., De Murcia, M., Fillard, J. P. & Vicario, E. Optical and electrical properties of SnO2 thin films in relation to their stoichiometric deviation and their crystalline structure. *Thin Solid Films* **41**, 127–135 (1977).

39. Chetri, P. & Choudhury, A. Investigation of optical properties of SnO2 nanoparticles. *Phys. E Low-Dimensional Syst. Nanostructures* **47**, 257–263 (2013).

40. Jarzebski, Z. M. & Morton, J. P. Physical Properties of SnO2 Materials: III . Optical Properties. *J. Electrochem. Soc.* **123**, 333C-346C (1976).

41. MANNA, I. & RAVICHANDRAN, J. Temperature dependent growth and optical properties of SnO2 nanowires and nanobelts. *Bull. Mater. Sci.* **33**, 357–364 (2010).

42. Augustin, M., Sommer, M. & Sysoev, V. V. UV-VIS sensor system based on SnO2 nanowires. *Sensors Actuators, A Phys.* **210**, 205–208 (2014).

43. Trindade, T., O'Brien, P. & Pickett, N. L. Nanocrystalline semiconductors: Synthesis, properties, and perspectives. *Chemistry of Materials* vol. 13 3843–3858 (2001).

44. Jarzebski, Z. M. & Marton, J. P. Physical Properties of SnO2 Materials: II . Electrical Properties. *J. Electrochem. Soc.* **123**, 299C-310C (1976).

45. Wan, Q., Dattoli, E. & Lu, W. Doping-Dependent Electrical Characteristics of SnO2 Nanowires. *Small* **4**, 451–454 (2008).

46. Kind, H., Yan, H., Messer, B., Law, M. & Yang, P. Nanowire Ultraviolet Photodetectors and Optical Switches. *Adv. Mater.* **14**, 158–160 (2002).

47. Keem, K. *et al.* Photocurrent in ZnO nanowires grown from Au electrodes. *Appl. Phys. Lett.* **84**, 4376–4378 (2004).

48. Chang, P. C. *et al.* High-performance ZnO nanowire field effect transistors. *Appl. Phys. Lett.* **89**, 133113 (2006).

49. Soci, C. *et al.* ZnO nanowire UV photodetectors with high internal gain. *Nano Lett.* **7**, 1003–1009 (2007).

50. Ziman, J. M. *Electrons and Phonons. Electrons and Phonons* (Oxford University Press, 2007). doi:10.1093/acprof:oso/9780198507796.001.0001.

51. Matsushima, S., Teraoka, Y., Miura, N. & Yamazoe, N. Electronic interaction between metal additives and tin dioxide in tin dioxide-based gas sensors. *Jpn. J. Appl. Phys.* **27**, 1798–1802 (1988).

52. Göpel, W. & Schierbaum, K. D. SnO2 sensors: current status and future prospects. *"Sensors Actuators, B Chem.* **26**, 1–12 (1995).

53. Kissine, V. V., Voroshilov, S. A. & Sysoev, V. V. Comparative study of SnO2 and SnO2:Cu thin films for gas sensor applications. *Thin Solid Films* **348**, 304–311 (1999).

54. Barsan, N. & Weimar, U. 7.3.3 Fundamentals of Metal Oxide Gas Sensors. in 618–621 (AMA Service GmbH, 2020). doi:10.5162/imcs2012/7.3.3.

55. Barsan, N. & Weimar, U. Conduction model of metal oxide gas sensors. *J. Electroceramics* **7**, 143–167 (2001).

56. US EPA, O. Volatile Organic Compounds' Impact on Indoor Air Quality.

57. Ahmed, W. M., Lawal, O., Nijsen, T. M., Goodacre, R. & Fowler, S. J. Exhaled Volatile Organic Compounds of Infection: A Systematic Review. *ACS Infectious Diseases* vol. 3 695–710 (2017).

58. Buszewski, B., Kesy, M., Ligor, T. & Amann, A. Human exhaled air analytics: Biomarkers of diseases. *Biomedical Chromatography* vol. 21 553–566 (2007).

59. *Volatile Organic Compounds' Impact on Indoor Air Quality*. (EPA, 2017).

60. *https://www.who.int/publications/i/item/9789241565196*.

61. https://www.epa.gov/sites/production/files/2016-09/documents/formaldehyde.pdf.

62. Xi, G. & Ye, J. Ultrathin SnO2 nanorods: Template- and surfactant-free solution phase synthesis, growth mechanism, optical, gas-Sensing, and surface adsorption properties. *Inorg. Chem.* **49**, 2302–2309 (2010).

63. Zheng, B. C. *et al.* Growth of less than 20 nm SnO nanowires using an anodic aluminum oxide template for gas sensing. *Micromachines* **11**, (2020).

64. Wagner, R. S. & Ellis, W. C. Vapor-liquid-solid mechanism of single crystal growth. *Appl. Phys. Lett.* **4**, 89–90 (1964).

65. Givargizov, E. . Highly Anisotropic Crystals | E.I. Givargizov | Springer. in (Springer, 1987).

66. Dubrovskii, V. G., Cirlin, G. E. & Ustinov, V. M. Semiconductor nanowhiskers: Synthesis, properties, and applications. *Semiconductors* vol. 43 1539–1584 (2009).

67. Zhang, X., Dubrovskii, V. G., Sibirev, N. V. & Ren, X. Analytical study of elastic relaxation and plastic deformation in nanostructures on lattice mismatched substrates. *Cryst. Growth Des.* **11**, 5441–5448 (2011).

68. Park, H. D. & Prokes, S. M. Study of Nanowire Growth Mechanisms: VLS and Si Assisted. in *One-Dimensional Nanostructures* 1–15 (Springer New York, 2008). doi:10.1007/978-0-387-74132-1_1.

69. Zhou, W., Zhang, Y., Niu, X. & Min, G. One-Dimensional SiC Nanostructures:

Synthesis and Properties. in *One-Dimensional Nanostructures* 17–59 (Springer New York, 2008). doi:10.1007/978-0-387-74132-1_2.

70. Mandl, B. *et al.* Growth mechanism of self-catalyzed group III-V nanowires. *Nano Lett.* **10**, 4443–4449 (2010).

71. Ross, F. M. Controlling nanowire structures through real time growth studies. *Reports Prog. Phys.* **73**, 114501 (2010).

72. Dubrovskii, V. G. *Nucleation Theory and Growth of Nanostructures*. (Springer Berlin Heidelberg, 2014). doi:10.1007/978-3-642-39660-1.

73. Calestani, D. *et al.* Nucleation and growth of SnO2 nanowires. in *Journal of Crystal Growth* vol. 275 e2083–e2087 (North-Holland, 2005).

74. Fan, H. J., Barnard, A. S. & Zacharias, M. ZnO nanowires and nanobelts: Shape selection and thermodynamic modeling. (2007) doi:10.1063/1.2720715.

75. Maier, L. Organic phosphorus compounds 90.1 a convenient, one-step synthesis of alkyl- and arylphosphonyl dichlorides. *Phosphorus. Sulfur. Silicon Relat. Elem.* **47**, 465–470 (1990).

76. Booth, G. Nitro Compounds, Aromatic. in *Ullmann's Encyclopedia of Industrial Chemistry* (Wiley-VCH Verlag GmbH & Co. KGaA, 2000). doi:10.1002/14356007.a17_411.

77. CDC - NIOSH Pocket Guide to Chemical Hazards - Dinitrotoluene. https://www.cdc.gov/niosh/npg/npgd0235.html.

78. Six, C. & Richter, F. Isocyanates, Organic. in *Ullmann's Encyclopedia of Industrial Chemistry* (Wiley-VCH Verlag GmbH & Co. KGaA, 2003). doi:10.1002/14356007.a14_611.

79. Gowenlock, B. G. & Richter-Addo, G. B. Preparations of C-nitroso compounds. *Chem. Rev.* **104**, 3315–3340 (2004).

80. Karwa, S. L. & Rajadhyaksha, R. A. Selective Catalytic Hydrogenation of Nitrobenzene to Hydrazobenzene. *Ind. Eng. Chem. Res.* **27**, 21–24 (1988).

81. Federal Register | govinfo. https://www.govinfo.gov/app/collection/fr.

82. CRC Handbook of Chemistry and Physics: A Ready-reference Book of Chemical ... - David R. Lide - Google Books. https://books.google.de/books/about/CRC_Handbook_of_Chemistry_and_Physics.html?id=q2qJId5TKOkC&redir_esc=y.

83. Althainz, P., Goschnick, J., Ehrmann, S. & Ache, H. J. Multisensor microsystem for contaminants in air. *Sensors Actuators, B Chem.* **33**, 72–76 (1996).

84. Ehrmann, S., Jüngst, J. & Goschnick, J. Automated cooking and frying control using a gas sensor microarray. *Sensors Actuators, B Chem.* **66**, 43–45 (2000).

85. Goschnick, J. An electronic nose for intelligent consumer products based on a gas analytical gradient microarray. in *Microelectronic Engineering* vols 57–58 693–704 (Elsevier, 2001).

86. Arnold, C., Haeringer, D., Kiselev, I. & Goschnick, J. Sub-surface probe module

equipped with the Karlsruhe Micronose KAMINA using a hierarchical LDA for the recognition of volatile soil pollutants. *Sensors Actuators, B Chem.* **116**, 90–94 (2006).

87. Gmür, R., Goschnick, J., Hocker, T., Schwarzenbach, H. & Sommer, M. Impact of sensor packaging on analytical performance and power consumption of metal oxide based gas sensor microarrays. *Sensors Actuators, B Chem.* **127**, 107–111 (2007).

88. Goschnick, J., Haeringer, D. & Kiselev, I. Multicomponent quantification with a novel method applied to gradient gas sensor microarray signal patterns. *Sensors Actuators, B Chem.* **127**, 237–241 (2007).

89. Zhou, D., Bennett, S. W. & Keller, A. A. Increased Mobility of Metal Oxide Nanoparticles Due to Photo and Thermal Induced Disagglomeration. *PLoS One* **7**, e37363 (2012).

90. Wiesner, M., Lowry, G., Alvarez, P., Dionysiou, D. & Biswas, P. Assessing the risks of manufactured nanomaterials. *Env. Sci Technol* **40**, (2006).

91. Sager, T. M. *et al.* Role of engineered metal oxide nanoparticle agglomeration in reactive oxygen species generation and cathepsin B release in NLRP3 inflammasome activation and pulmonary toxicity. *Inhal. Toxicol.* **28**, 686–697 (2016).

92. Godymchuk, A. *et al.* Agglomeration of iron oxide nanoparticles: pH effect is stronger than amino acid acidity. *J. Nanoparticle Res.* **21**, 1–12 (2019).

93. Siloxane - an overview | ScienceDirect Topics. https://www.sciencedirect.com/topics/earth-and-planetary-sciences/siloxane.

94. Palmisano, V. *et al.* Selectivity and resistance to poisons of commercial hydrogen sensors. in *International Journal of Hydrogen Energy* vol. 40 11740–11747 (Elsevier Ltd, 2015).

95. Choi, Y.-J. *et al.* Novel fabrication of an SnO(2) nanowire gas sensor with high sensitivity. *Nanotechnology* **19**, 095508 (2008).

96. Zheng Wei Pan, Zu Rong Dai & Zhong Lin Wang. Nanobelts of semiconducting oxides. *Science (80-.).* **291**, 1947–1949 (2001).

97. Huang, M. H. *et al.* Catalytic Growth of Zinc Oxide Nanowires by Vapor Transport. *Adv. Mater.* **13**, 113–116 (2001).

98. Sysoev, V. V., Goschnick, J., Schneider, T., Strelcov, E. & Kolmakov, A. A gradient microarray electronic nose based on percolating SnO 2 nanowire sensing elements. *Nano Lett.* **7**, 3182–3188 (2007).

99. Kalinin, S. V. *et al.* Electronic transport imaging in a multiwire SnO 2 chemical field-effect transistor device. *J. Appl. Phys.* **98**, 044503 (2005).

100. Henrion, R., Henrion, G., Henrion, R. & Henrion, G. Methoden der multivariaten linearen Regression. in *Multivariate Datenanalyse* 103–157 (Springer Berlin Heidelberg, 1995). doi:10.1007/978-3-642-57792-5_5.

101. Jurs, P. C., Bakken, G. A. & McClelland, H. E. Computational methods for the

analysis of chemical sensor array data from volatile analytes. *Chem. Rev.* **100**, 2649–2678 (2000).

102. Clifford, B., Beynon, D., Phillips, C. & Deganello, D. Printed-Sensor-on-Chip devices – Aerosol jet deposition of thin film relative humidity sensors onto packaged integrated circuits. *Sensors Actuators, B Chem.* **255**, 1031–1038 (2018).

103. Go, J., Sysoev, V. V., Kolmakov, A., Pimparkar, N. & Alam, M. A. A novel model for (percolating) nanonet chemical sensors for microarray-based E-nose applications. in *Technical Digest - International Electron Devices Meeting, IEDM* (2009). doi:10.1109/IEDM.2009.5424266.

104. Sysoev, V. V. *et al.* Percolating SnO2 nanowire network as a stable gas sensor: Direct comparison of long-term performance versus SnO2 nanoparticle films. *Sensors Actuators, B Chem.* **139**, 699–703 (2009).

105. Schierbaum, K. D., Weimar, U., Göpel, W. & Kowalkowski, R. Conductance, work function and catalytic activity of SnO2-based gas sensors. *Sensors Actuators B. Chem.* **3**, 205–214 (1991).

106. Burkhard, G. F., Hoke, E. T. & McGehee, M. D. Accounting for Interference, Scattering, and Electrode Absorption to Make Accurate Internal Quantum Efficiency Measurements in Organic and Other Thin Solar Cells. *Adv. Mater.* **22**, 3293–3297 (2010).

107. Hoefer, U., Kühner, G., Schweizer, W., Sulz, G. & Steiner, K. CO and CO2 thin-film SnO2 gas sensors on Si substrates. *Sensors Actuators B. Chem.* **22**, 115–119 (1994).

108. Trung, D. D. *et al.* Effective decoration of Pd nanoparticles on the surface of SnO2 nanowires for enhancement of CO gas-sensing performance. *J. Hazard. Mater.* **265**, 124–132 (2014).

109. Cheng, H., Garrick, D. J. & Fernando, R. L. Efficient strategies for leave-one-out cross validation for genomic best linear unbiased prediction. *J. Anim. Sci. Biotechnol.* **8**, (2017).

110. Handbook of X-ray Photoelectron Spectroscopy: A Reference Book of Standard ... - John F. Moulder - Google Books. https://books.google.de/books/about/Handbook_of_X_ray_Photoelectron_Spectros.html?id=A_XGQgAACAAJ&redir_esc=y.

111. Liu, Z. Review of Recent Developments in Fire Detection Technologies. *J. Fire Prot. Eng.* **13**, 129–151 (2003).

112. Thou-Ho Chen, Ping-Hsueh Wu & Yung-Chuen Chiou. An early fire-detection method based on image processing. *2004 Int. Conf. Image Process. 2004. ICIP '04.* **3**, 1707–1710 (2004).

113. O'Brien, C., Tharion, W. J., Karis, A. J. & Sullivan, H. M. Predicting military working dog core temperature during exertional heat strain: Validation of a Canine Thermal Model. *J. Therm. Biol.* **90**, (2020).

114. Potter, A. W., Berglund, L. G. & O'Brien, C. A canine thermal model for simulating temperature responses of military working dogs. *J. Therm. Biol.* **91**, (2020).

115. Hayes, J. E., McGreevy, P. D., Forbes, S. L., Laing, G. & Stuetz, R. M. Critical review of dog detection and the influences of physiology, training, and analytical methodologies. *Talanta* vol. 185 499–512 (2018).

116. Schoon, A., Fjellanger, R., Kjeldsen, M. & Goss, K. U. Using dogs to detect hidden corrosion. *Appl. Anim. Behav. Sci.* **153**, 43–52 (2014).

117. Räupke, A. *et al.* Highly sensitive gas-phase explosive detection by luminescent microporous polymer networks. *Sci. Rep.* **6**, 1–7 (2016).

118. Wang, C. *et al.* Trace detection of RDX, HMX and PETN explosives using a fluorescence spot sensor. *Sci. Rep.* **6**, 1–9 (2016).

119. Lichtenstein, A. *et al.* Supersensitive fingerprinting of explosives by chemically modified nanosensors arrays. *Nat. Commun.* **5**, 4195 (2014).

120. Zhou, C. *et al.* Ultrasensitive, Real-time and discriminative detection of improvised explosives by chemiresistive thin-film sensory array of Mn 2+ tailored hierarchical ZnS. *Sci. Rep.* **6**, 1–8 (2016).

Appendix I
UV LED Specification

The characteristics of the UV LED used in this work is presented in this section according to the datasheet.

■Forward voltage vs. Forward current

Ta=25℃

Forward current I_F (mA) vs. Forward voltage V_F (V)
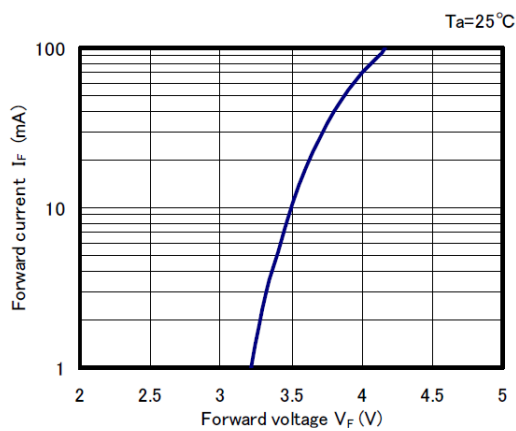
■Forward current vs. Relative output power

Ta=25℃

Relative output power (a.u.) vs. Forward current I_F (mA)
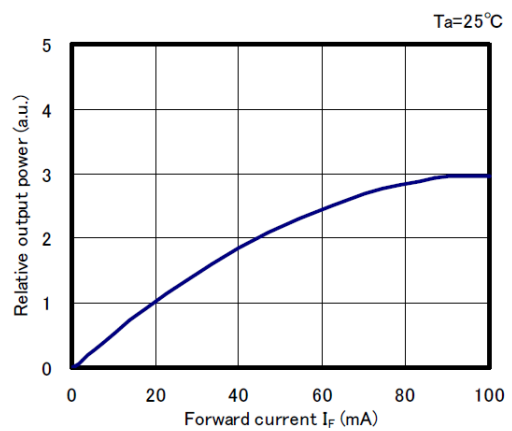
■Ambient temperature vs. Allowable forward current

Allowable forward current (mA) vs. Ambient temperature Ta (℃)

■Spectrum

Ta=25℃, I_F=20 mA

Relative output power (a.u.) vs. Wavelength λ (nm)

■Directivity

Ta=25℃

Relative output power
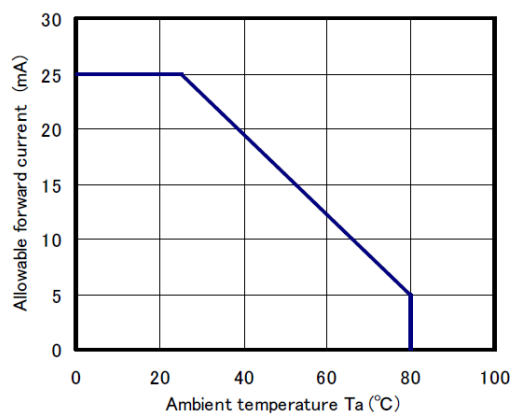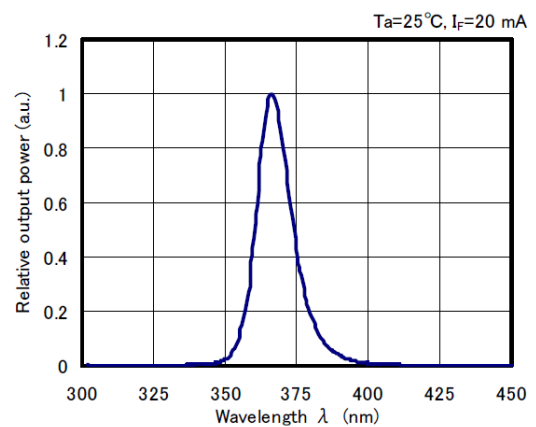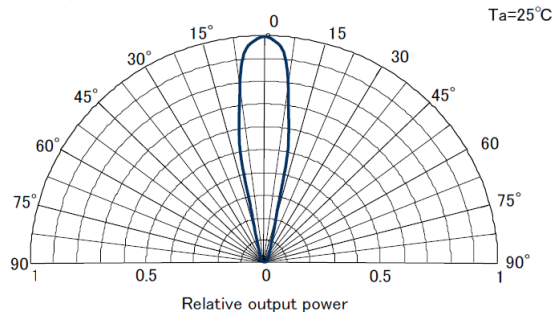
List of publications from the work

Peer review journal published:

M. Adib, R. Eckstein, G. Hernandez-Sosa, M. Sommer, and U. Lemmer, "SnO$_2$ nanowire-based aerosol jet printed electronic nose as fire detector," *IEEE Sens. J.*, vol. 18, no. 2, pp. 494–500, Jan. 2018, doi: 10.1109/JSEN.2017.2777178.

Conference proceeding:

M. Adib and M. Sommer, "UV excited SnO$_2$ nanowire based printed e-Nose: Potential application as burning smell detector and explosive detector," Jan. 2017, doi: 10.1109/ICSENS.2016.7808805.

M. Adib and M. Sommer, "Live demonstration: Printed e-Nose for universal applications," Jan. 2017, doi: 10.1109/ICSENS.2016.7808570.

Poster contribution:

M. Adib and M. Sommer, "The humidity effect on UV excited SnO$_2$ Nanowire based e-Nose," International conference on micro-and nanofabrication and manufacturing using lithography and related techniques at The Hague, Netherlands, 2015.

In preparation:

M. Adib, M. Sommer, U. Lemmer, "UV Chem FET KAMINA (KArlsruhe MIkro NAse) Novel eNose Based on Drain Current Modulation by Photo Gated SnO$_2$ Nanowire Mat".